DISEÑO ÓPTIMO DEL FACTOR DE PESO DEL CONTROLADOR PREDICTIVO DE CORRIENTE DE UNA MÁQUINA DE INDUCCIÓN DE SEIS FASES BASADO EN EL ALGORITMO DE OPTIMIZACIÓN DE ENJAMBRE DE PARTÍCULAS

TRABAJO FINAL DE MAESTRÍA

UNIVERSIDAD DEL CONO SUR DE LAS AMÉRICAS
Maestría en Ingeniería Electrónica con énfasis en Energías Renovables y Eficiencia Energética

DISEÑO ÓPTIMO DEL FACTOR DE PESO DEL CONTROLADOR PREDICTIVO DE CORRIENTE DE UNA MÁQUINA DE INDUCCIÓN DE SEIS FASES BASADO EN EL ALGORITMO DE OPTIMIZACIÓN DE ENJAMBRE DE PARTÍCULAS

Hector Fretes Acevedo
Autor

Prof. Dr. Jorge Esteban Rodas Benítez
Tutor

Prof. Dr. Jesús Doval-Gandoy
Cotutor

2020

TRIBUNAL EXAMINADOR

PROF. MSC. OSVALDO GONZÁLEZ, Universidad Nacional de Asunción, Paraguay

PROF. DR. JESÚS DOVAL-GANDOY, Universidad de Vigo, España

PROF. DR. RAÚL GREGOR, Universidad Nacional de Asunción, Paraguay

PROF. DR. JORGE RODAS, Universidad Nacional de Asunción, Paraguay

DR. IGNACIO GONZÁLEZ-PRIETO, Universidad de Málaga, España

Noviembre 2020
Asunción, Paraguay

RESUMEN

El control predictivo de estados finitos (FS-MPC) como control predictivo de corriente (PCC) es considerado una alternativa interesante para el control de las corrientes de estator de máquinas multifásicas, debido a la flexibilidad que ofrece el control, permitiendo la inclusión de restricciones con facilidad. La selección de una acción de control en el PCC involucra la minimización de una función de costo, en la cual se ven involucradas variables tales como las corrientes de estator, a través de factores de peso. Los factores de peso del PCC necesitan ser diseñados y ajustados para las variables de interés, como las corrientes de pérdida de la máquina, que se proyectan en el plano $(x - y)$. Este diseño es normalmente abordado por medio de procedimientos de prueba y error, no existiendo un enfoque sistemático para la solución de este problema. Para aplicaciones en motores de tres fases, técnicas de diseño basadas en redes neuronales o el coeficiente de variación han sido propuestas, sin embargo, la generalización de estas técnicas al caso de máquinas multifásicas no es algo trivial, y sólo procedimientos empíricos han sido reportados. En este contexto, el presente Trabajo Final de Maestría propone un método de ajuste del factor de peso del PCC basado en el algoritmo de optimización Multiobjetivo de Enjambre de Partículas (MOPSO), utilizando como objetivo la minimización de las raíces de los errores cuadráticos medios en el seguimiento de las corrientes de estator, utilizando el concepto de Óptimos de Pareto. Para ello es modelada y simulada una Máquina de Inducción Hexafásica Asimétrica, junto con el PCC, obteniendo Frentes de Pareto que proveen soluciones óptimas al problema, que luego son probados experimentales para validar la técnica propuesta.

Los resultados muestran que el error en el subespacio $(x - y)$ pueden obtenerse mejoras del orden de 500 % con un bajo efecto en el subespacio $(\alpha - \beta)$ con el método propuesto.

HECTOR FRETES ACEVEDO

Noviembre, 2020. Asunción, Paraguay.

SUMMARY

Finite State Predictive Control (FS-MPC) as Predictive Current Control (PCC) is considered an interesting alternative for stator's currents control in polyphasic machines, due to the control flexibility, allowing an easy inclusion of constraints. The selection of a control action in PCC involves the minimization of a cost function, which involves variables such as stator's currents, through the introduction of Weight Factors (WF). These WF for the PCC must be designeed and ajusted for the variables of interest, such as current losses that are projected to the $x - y$ plane. This design is usually approached by trial and error, lacking a systematic approach for this problem's solution. Tuning methods based in neural networks or the coefficient of variation were proposed for three-phase inverters and motors applications. However, the extension of this concepts to multiphase machine applications is not straigthforward. In this context, the present work proposes a WF tuning method based in the Multiobjective Particle Swarm Optimization algoritm (MOPSO), using as objective the minimization of Root-Mean-Square Error (RMSE) in stator's current tracking, using the Pareto Optimals concept. To achieve this, an Assymetric Hexafasic Induction Machine, obtaining Pareto Fronts that provide optimal solutions to the problem, this solutions are then validated through experiments in order to verify the validity of the proposed method.

Results show that RMSE for $x-y$ subspace can be improved around 500 %, with minor effect in $\alpha-\beta$ subspace, using the proposed method.

HECTOR FRETES ACEVEDO

Noviembre, 2020. Asunción, Paraguay.

AGRADECIMIENTOS

A mis tutores, Jorge Rodas y Jesús Doval-Gandoy por la dedicación y el apoyo que han brindado para la realización de este trabajo.

A los profesores nacionales e internacionales que formaron parte del plantel docente de la Maestría, por su orientación y su predisposición para atender dudas y consultas.

A mis compañeros, por su apoyo a lo largo de la Maestría.

A mis padres, sin quienes no hubiese podido alcanzar este logro.

H.F.

AGRADECIMIENTOS INSTITUCIONALES

Al Consejo Nacional de Ciencia y Tecnología (CONACYT) del Paraguay por el apoyo económico a través del programa de Maestría 17-POS-069 y el apoyo financiero en la presentación de artículos en conferencias internacionales.

A la Universidad del Cono Sur de las Américas (UCSA) por recibirnos en sus aulas para el desarrollo de esta Maestría.

Al Applied Power Electronics Technology Research Group (APET) de la Universidad de Vigo, España, por la realización de los ensayos experimentales.

H.F.

Dedicado a mis padres

ÍNDICE GENERAL

PARTE II MODELO MATEMÁTICO

PARTE III MÉTODO PROPUESTO

PARTE IV ANEXOS

ÍNDICE DE FIGURAS

ÍNDICE DE TABLAS

ACRÓNIMOS

AC	Corriente Alterna
DC	Corriente Continua
FS-MPC	Control Predictivo de Estados Finitos
IM	Máquina de inducción
MAE	Error Absoluto Medio
MOPSO	Optimización Multiobjetivo de Enjambre de Partículas
MPC	Control Predictivo Basado en Modelo
PCC	Control Predictivo de Corriente
PSO	Optimización de Enjambre de Partículas
RMSE	Raíz del Error Cuadrático Medio
VSI	Inversor con Fuente de Tensión

Parte I

GENERALIDADES

CAPÍTULO 1

JUSTIFICACIÓN Y METODOLOGÍA

1.1 Introducción

Las máquinas multifásicas pueden encontrarse hoy en día en una amplia variedad de productos comerciales, como turbinas eólicas, buses eléctricos, elevadores de alta velocidad, barcos, entre otros [1]. En comparación con las máquinas trifásicas convencionales, la principal ventaja de las topologías multifásicas radica en su mayor fiabilidad, con capacidades de tolerancia a fallas [2]. Sin embargo, una dificultad que presentan las máquinas multifásicas es la necesidad de controlar no solo las corrientes $\alpha - \beta$ del estator, sino también las corrientes del plano $x - y$, que se encuentran relacionadas a las pérdidas de la máquina [3]. Se han propuesto un sinnúmero de controladores de corriente del estator para máquinas multifásicas, tanto técnicas de control lineales, como no lineales [4]. Entre las técnicas no lineales, el control predictivo de estado finito (FS-MPC, del inglés Finite State - Model Predictive Control) como control predictivo de corriente (PCC, del inglés Predictive Current Control) ha sido una de las técnicas más estudiadas en la última década [5–7].

El PCC de máquinas multifásicas fue propuesto por primera vez en [8]. Desde entonces, se han propuesto varias mejoras para los métodos del PCC, enfocados en resolver problemas tales como la carga computacional [9], el mejoramiento del modelo del sistema [10], frecuencias de conmutación fijas [11], entre otros. Otras contribuciones más enfocadas en máquinas multifásicas fueron realizadas para la disminución de las corrientes $x - y$ [12, 13], el control predictivo de torque [14] y la operación post-falla [15]. En todos estos enfoques del FS-MPC, una función de costo es utilizada para seleccionar la acción de control a aplicar al sistema. En el FS-MPC multiobjetivo, esta función de costo incluye un factor de peso para cada una de las variables objetivo; los valores de estos factores de peso han sido usualmente determinados a través de prueba y error en el caso de sistemas de máquinas multifásicas, lo cual genera una relación de compromiso entre las variables de interés [16].

El diseño de los factores de peso tiene una influencia en el desempeño del controlador, sin embargo es aún un problema abierto y diversos enfoques han sido planteados para afrontar este problema. En [17] algunos lineamientos para funciones de costo sin factores de peso, funciones de costo con términos secundarios y funciones de costo con términos de igual importancia son mencionados. Estos lineamientos se basan en una estrategia heurística y constituyen una extensión de lo propuesto en [18]. Si bien estas indicaciones permiten reducir el número de pruebas para la selección de los factores de peso, siguen dependiendo de procedimientos empíricos. Recientemente, un enfoque basado en redes neurales fue propuesto para seleccionar los factores de peso de forma automática [19]. Aún así, un gran número de simulaciones o experimentos deben llevarse a cabo para extraer los datos necesarios. En [20] un resumen de las últimas técnicas para los convertidores electrónicos de potencia es presentado, pero no se considera el procedimiento de diseño para el caso de máquinas multifásicas. En [21] una estrategia heurística es propuesta para obtener los factores de peso para el caso de una máquina de inducción de cinco fases, aún así, estos valores no son aplicables a todas las máquinas de inducción multifásica [16].

En el presente Trabajo Final de Maestría se propone un procedimiento de diseño del factor de peso para el PCC de una máquina de inducción hexafásica asimétrica, utilizando un algoritmo de optimización de enjambre de partículas y el concepto de Óptimos de Pareto, obteniendo un conjunto de soluciones óptimas de las cuales el diseñador del controlador puede seleccionar según su necesidad, contando con la ventaja de ser fácilmente generalizable a otras topologías de máquinas multifásicas.

1.2 Motivación

El desarrollo del presente Trabajo Final de Maestría tiene como principal motivación la realización de aportes en el diseño óptimo del factor de peso del esquema de control PCC de una máquina hexafásica asimétrica.

1.3 Objetivos

Implementar un algoritmo de optimización multiobjetivo de enjambre de partículas para el diseño óptimo del factor de peso del controlador predictivo de corriente de una máquina de inducción hexafásica asimétrica. Concretamente, pueden enumarse los siguientes objetivos específicos:

- Modelar y simular la máquina de inducción hexafásica asimétrica.
- Implementar en simulación el control predictivo de corriente de la máquina de inducción hexafásica asimétrica.
- Obtener valores óptimos del factor de peso con la técnica propuesta.
- Validar experimentalmente el algoritmo, a través de valoraciones experimentales de los factores de peso obtenidos a través de él.

1.4 Organización del documento

El presente documento se encuentra organizado en cinco capítulos. Primeramente, en el **Capítulo 1** se presentan la justificación, la motivación y los objetivos del Trabajo Final de Maestría. En el **Capítulo 2** se desarrolla el modelo matemático de la máquina de inducción hexafásica asimétrica y se plantea el esquema de control. Luego, en el **Capítulo 3** se presenta el concepto de Óptimos de Pareto, junto con el algoritmo propuesto. En el **Capítulo 4** se exponen los factores de peso obtenidos por la técnica propuesta, además del desempeño del controlador en el seguimiento de corriente utilizando estos factores de peso. Y finalmente en el **Capítulo 5** se presentan las principales conclusiones y se proponen futuros trabajos siguiendo la línea de investigación de este Trabajo Final de Maestría.

Parte II

MODELO MATEMÁTICO

CAPÍTULO 2

MÁQUINAS DE INDUCCIÓN HEXAFÁSICAS ASIMÉTRICAS

Las IM hexafásicas asimétricas constan de dos devanados trifásicos independientes, conectados en estrella en el estator, desfasados 30° eléctricos entre sí, con los neutros aislados, como se muestra en la Figura 2.1. La ventaja principal de esta configuración radica en la posibilidad de utilizar convertidores trifásicos disponibles comercialmente para su accionamiento.

2.1 Modelo Matemático de la IM hexafásica asimétrica

Para el modelado matemático de máquinas polifásicas en general se hacen las siguientes consideraciones [22]:

- La topología del rotor es del tipo jaula de ardilla, pudiendo modelarse como n cargas inductivas interconectadas en paralelo a través de los anillos que sostienen a las barras que lo conforman.
- El estator está conformado por bobinados exactamente iguales entre sí.

- El entrehierro de la máquina se asume uniforme y de espesor constante, despreciándose su variaciones debidas a las excentricidades del rotor o por las ranuras del estator y rotor. Por tanto, el flujo en el entrehierro puede considerarse constante.

- Se asume que la característica de magnetización del material ferromagnético es lineal, por lo que no son considerados los efectos de la saturación magnética.

- Son ignoradas las variaciones que pueden producirse en las inductancias de fuga y las resistencias de los devanados de rotor y estator debido a cambios de frecuencia o temperatura.

- Las variables del rotor se encuentran proyectadas al estator mediante la relación de transformación del acoplamiento estator-rotor.

Como los bobinados distribuidos de la IM poseen naturaleza resistiva-inductiva, el equilibrio de tensión de cada fase, tanto del estator como del rotor, se rige por la siguiente ecuación:

$$v = Ri + \frac{d}{dt}\psi \tag{2.1}$$

donde, v es el voltaje instantáneo, R es la resistencia del bobinado, i es la corriente instantánea, ψ es el flujo magnético instantáneo.

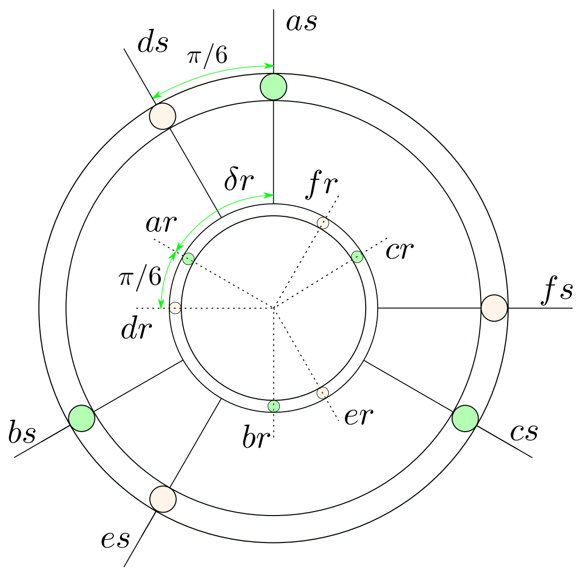

Figura 2.1: Esquema de los bobinados de la IM hexafásica asimétrica.

Como la IM analizada posee seis fases tanto en el estator como en el rotor, la ecuación del equilibrio de tensión por fase puede representarse de forma matricial como:

$$\begin{bmatrix} v_{sa} \\ v_{sd} \\ v_{sb} \\ v_{se} \\ v_{sc} \\ v_{sf} \end{bmatrix} = \begin{bmatrix} R_{sa} & 0 & 0 & 0 & 0 & 0 \\ 0 & R_{sd} & 0 & 0 & 0 & 0 \\ 0 & 0 & R_{sb} & 0 & 0 & 0 \\ 0 & 0 & 0 & R_{se} & 0 & 0 \\ 0 & 0 & 0 & 0 & R_{sc} & 0 \\ 0 & 0 & 0 & 0 & 0 & R_{sf} \end{bmatrix} \begin{bmatrix} i_{sa} \\ i_{sd} \\ i_{sb} \\ i_{se} \\ i_{sc} \\ i_{sf} \end{bmatrix} + \begin{bmatrix} \frac{d}{dt}\psi_{sa} \\ \frac{d}{dt}\psi_{sd} \\ \frac{d}{dt}\psi_{sb} \\ \frac{d}{dt}\psi_{se} \\ \frac{d}{dt}\psi_{sc} \\ \frac{d}{dt}\psi_{sf} \end{bmatrix} \tag{2.2}$$

$$\begin{bmatrix} v_{ra} \\ v_{rd} \\ v_{rb} \\ v_{re} \\ v_{rc} \\ v_{rf} \end{bmatrix} = \begin{bmatrix} R_{ra} & 0 & 0 & 0 & 0 & 0 \\ 0 & R_{rd} & 0 & 0 & 0 & 0 \\ 0 & 0 & R_{rb} & 0 & 0 & 0 \\ 0 & 0 & 0 & R_{re} & 0 & 0 \\ 0 & 0 & 0 & 0 & R_{rc} & 0 \\ 0 & 0 & 0 & 0 & 0 & R_{rf} \end{bmatrix} \begin{bmatrix} i_{ra} \\ i_{rd} \\ i_{rb} \\ i_{re} \\ i_{rc} \\ i_{rf} \end{bmatrix} + \begin{bmatrix} \frac{d}{dt}\psi_{ra} \\ \frac{d}{dt}\psi_{rd} \\ \frac{d}{dt}\psi_{rb} \\ \frac{d}{dt}\psi_{re} \\ \frac{d}{dt}\psi_{rc} \\ \frac{d}{dt}\psi_{rf} \end{bmatrix} \tag{2.3}$$

Como los bobinados del rotor de en la IM tipo jaula de ardilla se encuentran en cortocircuito, las tensiones del rotor en (2.3) son nulas.

El flujo magnético para el rotor y estator, por fase, viene dado por las siguientes ecuaciones:

$$\begin{bmatrix} \psi_{sa} \\ \psi_{sd} \\ \psi_{sb} \\ \psi_{se} \\ \psi_{sc} \\ \psi_{sf} \end{bmatrix} = L_s \begin{bmatrix} i_{sa} \\ i_{sd} \\ i_{sb} \\ i_{se} \\ i_{sc} \\ i_{sf} \end{bmatrix} + L_{sr} \begin{bmatrix} i_{ra} \\ i_{rd} \\ i_{rb} \\ i_{re} \\ i_{rc} \\ i_{rf} \end{bmatrix} \tag{2.4}$$

$$\begin{bmatrix} \psi_{ra} \\ \psi_{rd} \\ \psi_{rb} \\ \psi_{re} \\ \psi_{rc} \\ \psi_{rf} \end{bmatrix} = L_r \begin{bmatrix} i_{ra} \\ i_{rd} \\ i_{rb} \\ i_{re} \\ i_{rc} \\ i_{rf} \end{bmatrix} + L_{rs} \begin{bmatrix} i_{sa} \\ i_{sd} \\ i_{sb} \\ i_{se} \\ i_{sc} \\ i_{sf} \end{bmatrix} \tag{2.5}$$

siendo L_s y L_r matrices diagonales que representan las inductancias de estator y rotor, respectivamente. En tanto que L_{sr} y L_{rs} son las inductancias mutuas del estator a rotor y de rotor a estator, respectivamente.

Debido a las consideraciones realizadas anteriormente, las matrices de inductancia del estator y rotor son matrices diagonales con entradas constantes:

$$L_s = \begin{bmatrix} L_{ls} & 0 & 0 & 0 & 0 & 0 \\ 0 & L_{ls} & 0 & 0 & 0 & 0 \\ 0 & 0 & L_{ls} & 0 & 0 & 0 \\ 0 & 0 & 0 & L_{ls} & 0 & 0 \\ 0 & 0 & 0 & 0 & L_{ls} & 0 \\ 0 & 0 & 0 & 0 & 0 & L_{ls} \end{bmatrix} + L_{sr(\delta_r=0)} \tag{2.6}$$

$$L_s = \begin{bmatrix} L_{lr} & 0 & 0 & 0 & 0 & 0 \\ 0 & L_{lr} & 0 & 0 & 0 & 0 \\ 0 & 0 & L_{lr} & 0 & 0 & 0 \\ 0 & 0 & 0 & L_{lr} & 0 & 0 \\ 0 & 0 & 0 & 0 & L_{lr} & 0 \\ 0 & 0 & 0 & 0 & 0 & L_{lr} \end{bmatrix} + L_{rs(\delta_r=0)} \tag{2.7}$$

donde L_{ls} y L_{lr} son las inductancias de dispersión del estator y rotor respectivamente, en tanto que δ_r es el ángulo del rotor. La variación de δ_r modifica la posición relativa entre los bobinados del rotor y estator, por lo que las inductancias mutuas del estator a rotor y de rotor a estator varían en el tiempo. Estas inductancias mutuas tienen su valor pico cuando $\delta_r = 0$. La velocidad eléctrica del rotor se obtiene a partir de:

$$\delta_r(t) = \int_0^t \omega_r dt \tag{2.8}$$

Con las consideraciones tomadas al principio de esta sección, los flujos generados tanto en el estator como en el rotor son sinusoidales, por lo que la matriz de inductancia mutua del estator al rotor puede expresarse como:

$$L_{sr} = M \begin{bmatrix} cos(\delta_r) & cos(\eta_d) & cos(\eta_b) & cos(\eta_e) & cos(\eta_c) & cos(\eta f) \\ cos(\eta_f) & cos(\delta_r) & cos(\eta_d) & cos(\eta_b) & cos(\eta_e) & cos(\eta_c) \\ cos(\eta_c) & cos(\eta_f) & cos(\delta_r) & cos(\eta_d) & cos(\eta_b) & cos(\eta_e) \\ cos(\eta_e) & cos(\eta_c) & cos(\eta_f) & cos(\delta_r) & cos(\eta_d) & cos(\eta_b) \\ cos(\eta_b) & cos(\eta_e) & cos(\eta_c) & cos(\eta_f) & cos(\delta_r) & cos(\eta_d) \\ cos(\eta_d) & cos(\eta_b) & cos(\eta_e) & cos(\eta_c) & cos(\eta_f) & cos(\delta_r) \end{bmatrix} \tag{2.9}$$

donde M es la inductancia de magnetización. Los ángulos η se obtienen mediante:

$$\begin{array}{lll} \eta_d = \delta_r + \varphi & \eta_b = \delta_r + \frac{2}{3}\pi & \eta_e = \delta_r + \frac{2}{3}\pi + \varphi \\ \eta_c = \delta_r + \frac{4}{3}\pi & \eta_f = \delta_r + \frac{4}{3}\pi + \varphi & \end{array} \tag{2.10}$$

siendo $\varphi = \frac{pi}{6}$ el desfasaje angular entre dos devanados trifásicos, para el caso de la IM hexafásica asimétrica. Y, además:

$$L_{rs} = L_{sr}^T$$

De esta forma, las ecuaciones (2.2) y (2.3) pueden escribirse como:

$$v_s = R_s i_s + L_s \frac{d}{dt} i_s + L_{sr} \frac{d}{dt} i_r \tag{2.11}$$

$$v_r = R_r i_r + L_r \frac{d}{dt} i_r + L_{rs} \frac{d}{dt} i_s \tag{2.12}$$

Estas ecuaciones describen el comportamiento eléctrico de la IM, en tanto que para el comportamiento mecánico se puede relacionar el par de torsión y los parámetros de la mecánicos de la máquina según la ecuación:

$$P(T_e - T_l) = J_m \frac{d}{dt} \omega_r + B_m \omega_r \tag{2.13}$$

donde

T_e: par electromagnético

T_L: par de torsión de la carga mecánica

J_m: coeficiente de inercia

B_m: coeficiente de fricción

ω_r: velocidad eléctrica

Las ecuaciones (2.2)-(2.13) describen completamente el comportamiento del motor mediante un modelo no lineal de ecuaciones diferenciales con coeficientes variantes en el tiempo, debido a que estos coeficientes dependen de la inductancia mutua entre estator y rotor.

La resolución de estas ecuaciones en función de las variables de fase implica un gran costo computacional, por lo que frecuentemente se simplifica el modelo de la IM mediante la descomposición en vectores espaciales (VSD, del inglés *Vector Space Decomposition*), por el cual se transforma el sistema a uno de tres sub-espacios bidimensionales ortogonales entre sí [23, 24]. Estas transformaciones pueden representarse en un marco de referencia estacionario, a través de la transformada de Clarke, o bien en un marco de referencia dinámico a través de la transformada de Park. El modelo de la IM a utilizar en este trabajo está basado en la Transformada de Clarke.

2.1.1 Transformada de Clarke

La transformada de Clarke permite descomponer el espacio de seis dimensiones del modelo descrito anteriormente en tres planos bidimensionales que son ortogonales entre sí. Al ser estos planos ortogonales, se encuentran totalmente desacoplados entre sí, lo cual simplifica el modelo de la IM hexafásica asimétrica. Esta transformación se puede describir según la ecuación:

$$\begin{bmatrix} \Psi_\alpha \\ \Psi_\beta \\ \Psi_x \\ \Psi_y \\ \Psi_{z1} \\ \Psi_{z2} \end{bmatrix} = \mathbf{C_k} \begin{bmatrix} \Psi_a \\ \Psi_d \\ \Psi_b \\ \Psi_e \\ \Psi_c \\ \Psi_f \end{bmatrix} \tag{2.14}$$

donde el vector $[\Psi_\alpha, \Psi_\beta, \Psi_x, \Psi_y, \Psi_{z1}, \Psi_{z2}]^T$ representa las magnitudes eléctricas de tensión, corriente o flujo luego de la transformación, en tanto que $\mathbf{C_k}$, para el caso particular de la IM asimétrica hexafásica considerada y para una transformación de amplitud invariante [25], es la matriz:

$$\mathbf{C_k} = \frac{1}{3}\begin{bmatrix} 1 & \frac{\sqrt{3}}{2} & -\frac{1}{2} & -\frac{\sqrt{3}}{2} & -\frac{1}{2} & 0 \\ 0 & \frac{1}{2} & \frac{\sqrt{3}}{2} & \frac{1}{2} & -\frac{\sqrt{3}}{2} & -1 \\ 1 & -\frac{\sqrt{3}}{2} & -\frac{1}{2} & \frac{\sqrt{3}}{2} & -\frac{1}{2} & 0 \\ 0 & \frac{1}{2} & -\frac{\sqrt{3}}{2} & \frac{1}{2} & \frac{\sqrt{3}}{2} & -1 \\ 1 & 0 & 1 & 0 & 1 & 0 \\ 0 & 1 & 0 & 1 & 0 & 1 \end{bmatrix} \tag{2.15}$$

Tras esta transformación se obtiene un modelo desacoplado descrito según las siguientes ecuaciones:

$$v_{s\alpha} = R_s i_{s\alpha} + L_s \frac{d}{dt} i_{s\alpha} + L_m \frac{d}{dt}\left(i'_{r\alpha} cos(\delta) - i'_{r\beta} sin(\delta)\right) \tag{2.16}$$

$$v_{s\beta} = R_s i_{s\beta} + L_s \frac{d}{dt} i_{s\beta} + L_m \frac{d}{dt}\left(i'_{r\alpha} sin(\delta) + i'_{r\beta} cos(\delta)\right) \tag{2.17}$$

$$v_{r\alpha} = R_r i'_{r\alpha} + L_r \frac{d}{dt} i'_{r\alpha} + L_m \frac{d}{dt}\left(i_{s\alpha} cos(\delta) + i_{s\beta} sin(\delta)\right) = 0 \tag{2.18}$$

$$v_{r\beta} = R_r i'_{r\beta} + L_r \frac{d}{dt} i'_{r\beta} + L_m \frac{d}{dt}\left(-i_{s\alpha} sin(\delta) + i_{s\beta} cos(\delta)\right) = 0 \tag{2.19}$$

$$v_{sx} = R_s i_{sx} + L_{ls} \frac{d}{dt} i_{sx} \tag{2.20}$$

$$v_{sy} = R_s i_{sy} + L_{ls} \frac{d}{dt} i_{sy} \tag{2.21}$$

$$v_{sz1} = R_s i_{sz1} + L_{ls} \frac{d}{dt} i_{sz1} \tag{2.22}$$

$$v_{sz2} = R_s i_{sz2} + L_{ls} \frac{d}{dt} i_{sz2} \tag{2.23}$$

Y el par electromagnético viene dado por:

$$T_e = 3PL_m(i_{r\alpha} i_{s\beta} - i_{r\beta} i_{s\alpha}) \tag{2.24}$$

donde,

L_m: inductancia de magnetización

L_s: inductancia del estator, $L_s = L_m + Lls$

L_r: inductancia del rotor, $L_r = L_m + Llr$

Como la componente fundamental de flujo se encuentra mapeada al plano $\alpha - \beta$, este es el plano vinculado a la conversión de energía. En los planos $x - y$ y $z_1 - z_2$, considerando el devanado de la IM del tipo distribuido, sólo se encuentran variables del estator, en el plano $x - y$ se encuentran componentes relacionadas a las pérdidas en el estator, en tanto que en el plano $z_1 - z_2$ se representan las componentes homopolares que, al tratarse una IM con dos neutros aislados entre sí, la corriente del estator en este plano es nula.

2.1.2 Transformada de Park

Cuando se definen las variables respecto a otros marcos de referencia dinámicos, es posible obtener mayores simplificaciones, a partir de la Transformada de Clarke, aplicando transformaciones matriciales. Debido a que el estator y el rotor sólo se encuentran acoplados en el plano $\alpha - \beta$ las transformaciones a marcos de referencia dinámicos sólo afectarán a las variables eléctricas definidas en dicho plano. Para la transformada de Park, la transformación se define de tal forma que los conjuntos de bobinados del estator y el rotor giren a la misma velocidad angular, eliminando así el movimiento relativo entre los bobinados de estator y rotor, obteniendo un nuevo conjunto de ecuaciones diferenciales con coeficientes constantes.

Como en una máquina de inducción hexafásica asimétrica el entrehierro es constante, al igual que las inductancias de los bobinados, la elección de la velocidad de giro del marco de referencia es arbitrario. Si se denota la velocidad de giro del marco de referencia dinámico como ω_a, la posición instantánea respecto al marco de referencia está definida por:

$$\theta_a(t) = \int_0^t \omega_a dt \tag{2.25}$$

Del mismo modo, el rotor gira a una velocidad ω_r, definiéndose su posición respecto al marco de referencia estático por la variable θ; en tanto que respecto al marco de referencia dinámico $d - q$ está definida por ω_r, que depende de la velocidad relativa entre el marco de referencia dinámico y el rotor: ω_{sl}, denominada deslizamiento:

$$\theta = \theta_a - \theta_r = \int_0^t (\omega_a - \omega_r)dt = \int_0^t \omega_{sl} dt \tag{2.26}$$

El segundo eje, el eje q, es perpendicular al eje d, por lo que la transformación de las variables de estator y rotor viene dada por:

$$\begin{bmatrix} \Psi_d \\ \Psi_q \\ \Psi_x \\ \Psi_y \\ \Psi_{z1} \\ \Psi_{z2} \end{bmatrix} = \mathbf{D} \begin{bmatrix} \Psi_\alpha \\ \Psi_\beta \\ \Psi_x \\ \Psi_y \\ \Psi_{z1} \\ \Psi_{z2} \end{bmatrix} \tag{2.27}$$

Esta matriz $\mathbf{D}$, para las variables de estator, tiene la forma:

$$\mathbf{D}_s = \begin{bmatrix} cos(\theta_a) & -sin(\theta_a) & 0 & 0 & 0 & 0 \\ sin(\theta_a) & cos(\theta_a) & 0 & 0 & 0 & 0 \\ 0 & 0 & 1 & 0 & 0 & 0 \\ 0 & 0 & 0 & 1 & 0 & 0 \\ 0 & 0 & 0 & 0 & 1 & 0 \\ 0 & 0 & 0 & 0 & 0 & 1 \end{bmatrix} \tag{2.28}$$

En tanto que para las variables de rotor tiene la forma:

$$\mathbf{D}_s = \begin{bmatrix} cos(\theta_r) & -sin(\theta_r) & 0 & 0 & 0 & 0 \\ sin(\theta_r) & cos(\theta_r) & 0 & 0 & 0 & 0 \\ 0 & 0 & 1 & 0 & 0 & 0 \\ 0 & 0 & 0 & 1 & 0 & 0 \\ 0 & 0 & 0 & 0 & 1 & 0 \\ 0 & 0 & 0 & 0 & 0 & 1 \end{bmatrix} \tag{2.29}$$

Puede observarse que estas transformaciones sólo afectan a las ecuaciones en el plano $\alpha - \beta$, en tanto que las ecuaciones en los sub-espacios $x - y$ y $z_1 - z_2$ se mantienen invariantes. La transformación es invertible, y como $\mathbf{D}_s$ y $\mathbf{D}_r$ son ortogonales, la inversión se reduce a la transposición de la matriz, esto es, $\mathbf{D}^{-1} = \mathbf{D}^T$.

Aplicando entonces la transformación de Park, el modelo resultante queda definido por las siguientes ecuaciones de equilibrio de tensión:

$$v_{ds} = R_s i_{ds} + L_s \frac{d}{dt} i_{ds} + L_m \frac{d}{dt} i_{dr} - \omega_a \left(L_s i_{qs} + L_m i_{qr} \right) \tag{2.30}$$

$$v_{qs} = R_s i_{qs} + L_s \frac{d}{dt} i_{qs} + L_m \frac{d}{dt} i_{qr} - \omega_a \left(L_s i_{ds} + L_m i_{dr} \right) \tag{2.31}$$

$$v_{dr} = R_r i_{dr} + L_m \frac{d}{dt} i_{ds} + L_r \frac{d}{dt} i_{qr} - \omega_{sl} \left(L_m i_{qs} + L_r i_{qr} \right) = 0 \tag{2.32}$$

$$v_{qr} = R_r i_{qr} + L_m \frac{d}{dt} i_{qs} + L_r \frac{d}{dt} i_{qr} - \omega_{sl} \left(L_m i_{ds} + L_r i_{dr} \right) = 0 \tag{2.33}$$

Por lo mencionado anteriormentes, el resto de las ecuaciones es exactamente igual a las ecuaciones (2.20) a (2.23). Y finalmente, el par electromagnético generado se define por:

$$T_e = 3PL_m(i_{dr} i_{qs} - i_{qr} i_{ds}) \tag{2.34}$$

Con las transformaciones anteriormente discretas, y el modelo del inversor de voltaje (VSI, del inglés Voltage Source Inverter) es posible modelar el sistema para su control.

2.1.3 Modelo del convertidor electrónico de potencia

La máquina hexafásica es alimentada por un VSI de seis ramas y dos niveles. Se considera que el DC-Link es alimentado con una fuente de tensión V_{DC} de corriente continua. Cada rama del convertidor está compuesta por dos interruptores electrónicos de potencia, totalizando doce interruptores. El punto medio de cada rama corresponde a la salida del VSI. Como se asume que las fases del IM tienen bobinados exactamente iguales, el VSI alimenta una carga balanceada en conexión estrella, siendo la carga predominantemente inductiva. Las tensiones de fase se definen por las variables V_{sk} y $V_{sk'}$, siendo $k = [a, b, c]$ y $k' = [d, e, f]$.

A fin de evitar cortocircuitos, en cada rama sólo puede ser activado un interruptor a la vez. Además, debido a que al encontrarse apagados ambos interruptores no se ejerce ningún tipo de control sobre la carga este estado también debe ser evitado. El esquema del VSI conectado a la IM hexafásica asimétrica se observa en la Figura 2.2.

Para cumplir las condiciones anteriormente especificadas, deben utilizarse señales de disparo complementarias para cada par de interruptores de cada rama. De esta forma, el estado de cada rama, S_k y $S_{k'}$, puede definirse utilizando lógica binaria: $S_k \in [0, 1]$,

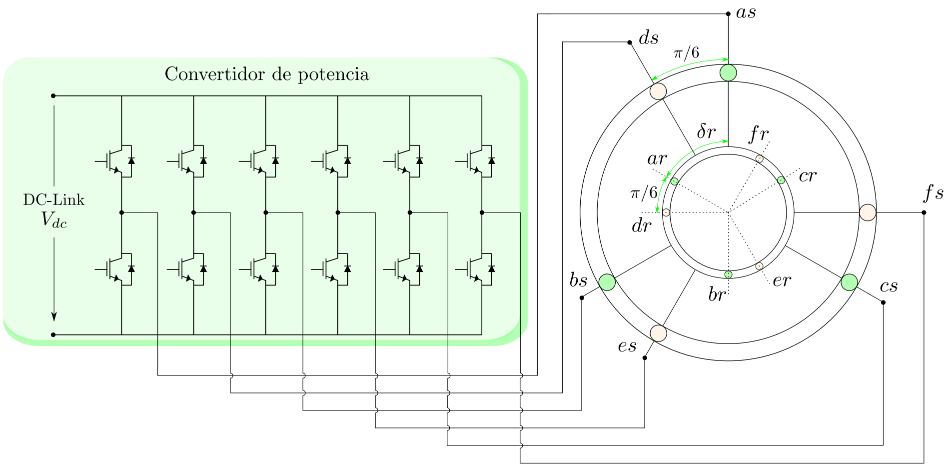

Figura 2.2: Conexión del VSI a la IM hexafásica asimétrica.

$S_{k'} \in [0, 1]$. Para el caso en el que el interruptor superior se encuentra encendido y el inferior apagado se cumple que $S_k = 1$, $S_{k'} = 0$, en tanto que para el caso opuesto se tiene que $S_k = 0$, $S_{k'} = 1$; permitiendo así que en la salida del VSI se disponga de dos niveles de tensión: $\pm\frac{V_{DC}}{2}$ respecto al punto medio del DC-Link. De esta forma, el vector de conmutación $[S_a, S_d, S_b, S_e, S_c, S_f]^T$.

Las tensiones v_{kn} y $v_{k'n}$ respecto al bus negativo del DC-Link queda definido por el estado de conmutación de cada rama:

$$v_{kn} = V_{DC} S_k \qquad v_{k'n} = V_{DC} S_{k'} \tag{2.35}$$

Estas tensiones se relacionan con las tensiones de fase de la IM, v_{kN} y $v_{kN'}$, y las tensiones entre el bus negativo del DC-Link y los puntos comunes del conexionado en estrella, v_{Nn} y $v_{N'n}$, de la siguiente manera:

$$v_{kn} = V_{kN} + V_{Nn} \qquad v_{k'n} = V_{kN'} + V_{N'n} \tag{2.36}$$

Como se considera una carga balanceada, la suma de las tensiones de fase es igual a cero, por lo que las tensiones v_{Nn} y $v_{N'n}$ quedan definidas por:

$$V_{Nn} = \frac{1}{3}(V_{an} + V_{bn} + V_{cn}) \qquad V_{N'n} = \frac{1}{3}(V_{dn} + V_{en} + V_{fn}) \tag{2.37}$$

Y, reemplazando en (2.36):

$$\begin{aligned} v_{kN} = v_{kn} - V_{Nn} = V_{DC}S_k - \tfrac{1}{3}(V_{an} + V_{bn} + V_{cn}) \\ v_{kN'} = v_{k'n} - V_{N'n} = V_{DC}S_{k'} - \tfrac{1}{3}(V_{dn} + V_{en} + V_{fn}) \end{aligned} \tag{2.38}$$

Las tensiones de fase se pueden expresar de forma matricial como:

$$\mathbf{M}_{sw} = \begin{bmatrix} v_{aN'} \\ v_{dN'} \\ v_{bN'} \\ v_{eN'} \\ v_{cN'} \\ v_{fN'} \end{bmatrix} = \frac{V_{DC}}{3} \begin{bmatrix} 2 & 0 & -1 & 0 & -1 & 0 \\ 0 & 2 & 0 & -1 & 0 & -1 \\ -1 & 0 & 2 & 0 & -1 & 0 \\ 0 & -1 & 0 & 2 & 0 & -1 \\ -1 & 0 & -1 & 0 & 2 & 0 \\ 0 & -1 & 0 & -1 & 0 & 2 \end{bmatrix} \mathbf{S}^T. \tag{2.39}$$

donde las señales de disparo son $\mathbf{S} = [S_a,\ S_b,\ S_c,\ S_d,\ S_e,\ S_f]$, siendo $S_i \in \{0,\ 1\}$, y V_{dc} es el voltaje del DC-Bus.

A este modelo del VSI es posible aplicar la Transformada de Clarke, y utilizarlo para el modelo discreto en el espacio de estados de la IM, descrito en la siguiente sección.

2.1.4 Modelo discreto de la IM en el espacio de estados

La representación en el espacio de estados del modelo discreto del sistema se puede escribir como:

$$\mathbf{x}_{k+1} = \mathbf{A}\,\mathbf{x}_k + \mathbf{B}\,\mathbf{u}_k + \mathbf{n}_k \tag{2.40}$$

$$\mathbf{y}_k = \mathbf{C}\,\mathbf{x}_k + \mathbf{m}_k \tag{2.41}$$

donde el vector de estados consiste en las corrientes de estator y de rotor:

$$\mathbf{x}_k = \left[i_{s\alpha(k)},\ i_{s\beta(k)},\ i_{sx(k)},\ i_{sy(k)}, i_{r\alpha(k)},\ i_{r\beta(k)}\right]^T \tag{2.42}$$

en tanto que el vector de entrada está compuesto por los voltajes de estator:

$$\mathbf{u}_k = \left[u_{s\alpha(k)},\ u_{s\beta(k)},\ u_{sx(k)},\ u_{sy(k)}\right]^T \tag{2.43}$$

y las corrientes de estator constituyen el vector de salida:

$$\mathbf{y}_k = \left[i_{s\alpha(k)},\, i_{s\beta(k)},\, i_{sx(k)},\, i_{sy(k)}\right]^T \tag{2.44}$$

$\mathbf{n}_k$ y $\mathbf{m}_k$ representan el ruido de proceso y el ruido de medición, respectivamente.

Debido a su interacción con el VSI, los voltajes del estator poseen una naturaleza discreta, lo cual puede representarse como:

$$\mathbf{u}_k = \mathbf{C_k}\, \mathbf{M}_{Sw} \tag{2.45}$$

Siendo $\mathbf{C_k}$ la matriz de Transformación de Clarke.

A partir de las ecuaciones definidas en la sección 2.1.1, se definen las matrices $\mathbf{A}$ y $\mathbf{B}$ de la siguiente forma:

$$\mathbf{A} = \begin{bmatrix} a_{11} & a_{12} & 0 & 0 & a_{15} & a_{16} \\ a_{21} & a_{22} & 0 & 0 & a_{25} & a_{26} \\ 0 & 0 & a_{33} & 0 & 0 & 0 \\ 0 & 0 & 0 & a_{44} & 0 & 0 \\ a_{51} & a_{52} & 0 & 0 & a_{55} & a_{56} \\ a_{61} & a_{62} & 0 & 0 & a_{65} & a_{66} \end{bmatrix} \quad \mathbf{B} = \begin{bmatrix} b_1 & 0 & 0 & 0 \\ 0 & b_1 & 0 & 0 \\ 0 & 0 & b_2 & 0 \\ 0 & 0 & 0 & b_2 \\ b_3 & 0 & 0 & 0 \\ 0 & b_3 & 0 & 0 \end{bmatrix} \tag{2.46}$$

donde:

$$\begin{array}{lll} a_{11} = a_{22} = 1 - T_s\, c_2\, R_s & a_{12} = -a_{21} = T_s\, c_4 L_m\, \omega_{r(k)} & a_{56} = -a_{65} = -c_5\, \omega_{r(k)}\, T_s\, L_r \\ a_{15} = a_{26} = T_s\, c_4\, R_r & a_{16} = -a_{25} = T_s\, c_4 L_r\, \omega_{r(k)} & b_1 = T_s\, c_2 \\ a_{33} = a_{44} = 1 - T_s\, c_3\, R_s & a_{51} = a_{62} = -T_s\, c_4\, R_s & b_2 = T_s\, c_3 \\ a_{52} = -a_{61} = -T_s\, c_5\, L_m\, \omega_{r(k)} & a_{55} = a_{66} = 1 - T_s\, c_5\, R_r & b_3 = -T_s\, c_4 \end{array}$$

siendo T_s el tiempo de muestreo, y $c_1 - c_5$ se definen como:

$$c_1 = L_s L_r - L_m^2 \tag{2.47}$$

$$c_2 = \frac{L_r}{c_1} \tag{2.48}$$

$$c_3 = \frac{1}{L_{ls}} \tag{2.49}$$

$$c_4 = \frac{L_m}{c_1} \tag{2.50}$$

$$c_5 = \frac{L_s}{c_1} \tag{2.51}$$

La velocidad eléctrica del rotor (ω_r) está relacionada con el torque de la carga (T_l) y el torque generado (T_e) según la ecuación:

$$J_m \, \frac{d}{dt}\omega_r + B_m \, \omega_r = P \, (T_e - T_l) \tag{2.52}$$

donde T_e puede expresarse como:

$$T_e = 3 \, P \, M \, (i_{r\beta} \, i_{s\alpha} - i_{r\alpha} \, i_{s\beta}) \tag{2.53}$$

siendo $M = \frac{L_m}{3}$.

Estas ecuaciones, además de describir el sistema, permiten predecir su comportamiento futuro, por lo que constituyen la base del control predictivo del sistema.

2.2 Control Predictivo de Corriente

El control de la IM hexafásica asimétrica representa un problema de alta complejidad, ya que se trata de un sistema no lineal, de múltiples variables, algunas de las cuales no son medibles, por lo que deben ser estimadas. Además, los parámetros eléctricos del motor varían según el punto de operación [26].

Si bien las estrategias de control comúnmente aplicadas a máquinas multifásicas consisten en extensiones de técnicas de control aplicadas máquinas trifásicas, tales como el control orientado de campo (FOC, del ingés Field Oriented Control) basado en el control proporcional-integral (PI) de corriente, el control de torque, entre otros [23, 27]; en los últimos años nuevas técnicas de control no lineal han sido desarrolladas, como el control predictivo de estados finitos (FCS-MPC, del inglés Finite Control Set-Model Predictive Control), que presenta ventajas en la velocidad de respuesta en estado transitorio en comparación a controladores lineales, presentando mejoras en la respuesta en estado transitorio, con una reducción importante en las corrientes en el plano $x - y$ [28–32].

El FCS-MPC se caracteriza por utilizar el modelo del sistema para predecir su comportamiento futuro. A partir de la predicción de las variables controladas, por medio de la minimización de una función de costo, es posible ejercer el esfuerzo de control óptimo. Entre las ventajas de esta estrategia de control se encuentran:

- Es aplicable a una amplia variedad de sistemas, incluyendo sistemas de múltiples variables.
- Una vez se tiene modelado el sistema a controlar, los conceptos utilizados son intuitivos.
- Permite incluir fenómenos no lineales al sistema de manera sencilla.
- Permite la compensación de tiempos muertos.
- El controlador resultante es fácil de implementar.

La principal desventaja del FCS-MPC es el alto costo computacional, sin embargo, con la creciente capacidad de cómputo de los microcontroladores comerciales este alto costo resulta cada vez menos limitante. A esto debe agregarse que la precisión del modelo matemático del sistema influye directamente en la eficiencia del FCS-MPC, por lo que si existen variaciones de los parámetros en el tiempo se requiere adaptar el modelo para mantener la eficiencia del FSC-MPC [17].

En este caso, se trata de un control predictivo de corriente (PCC, del inglés Predictive Current Control), en el que se hace uso del modelo discreto descrito en las ecuaciones (2.40) y (2.41).

A partir de dichas ecuaciones es posible predecir, para el tiempo $[k]$, las corrientes del estator de la IM hexafásica en el tiempo $[k+1]$. En la Figura 2.3 se presenta un diagrama esquemático de dicho esquema de control.

Se realizan entonces 64 predicciones, una por cada estado posible del VSI, seleccionando como próximo estado del VSI el estado que presente el menor valor de la función de costo seleccionada. En implementaciones prácticas no es posible medir las corrientes del rotor, por debe utilizarse un observador que permita estimar estas corrientes [25]. Sin embargo, para las simulaciones, a modo de aliviar la carga computacional se ha obviado el observador.

2.2.1 Función de costo

La selección de la función de costo permite optimizar variables tales como el contenido de armónicos, las pérdidas de conmutación en el VSI, el rizado en el torque de la máquina, entre otros. Sin embargo, para el caso estudiado, la figura de mérito más importante es el error en el seguimiento de las corrientes de estator predichas en los planos $(\alpha - \beta)$ y

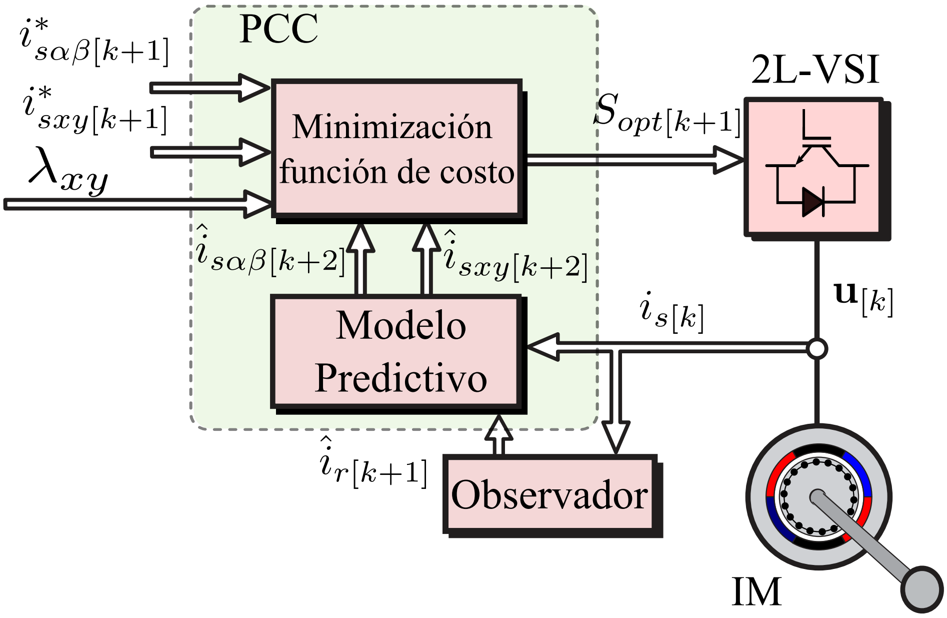

Figura 2.3: Diagrama esquemático de la estrategia de control. El observador no es implementado, para aliviar el costo computacional en las simulaciones.

$(x-y)$ para el siguiente muestreo. Por esta razón, la función de costo seleccionada es una suma ponderada de los errores cuadráticos medios (MSE, del inglés Mean-Square Error) de las corrientes en los planos $\alpha-\beta$ y $x-y$, en la que se incluye un factor de peso (WF, del inglés Weighting Factor), definida por la ecuación:

$$J = |i^*_{s\alpha\beta[k+1]} - i_{s\alpha\beta[k+1]}|^2 + \lambda_{xy}.|i^*_{sxy[k+1]} - i_{sxy[k+1]}|^2 \tag{2.54}$$

donde

$i^*_{s\alpha\beta[k+1]}$: referencia de corriente en el plano $\alpha-\beta$

$i_{s\alpha\beta[k+1]}$: corriente predicha en el plano $\alpha-\beta$

$i^*_{sxy[k+1]}$: referencia de corriente en el plano $x-y$

$i_{sxy[k+1]}$: corriente predicha en el plano $x-y$

λ_{xy}: WF

Sin embargo, debido a que la acción de control seleccionada en un tiempo de muestreo no será aplicada sino hasta el siguiente ciclo de muestreo, ya que el tiempo necesario para la medición, el cálculo de las predicciones y la selección de la acción de control óptima implica un tiempo comparable con el período de muestreo. Para compensar este retardo se considera el segundo horizonte de predicción, lo cual consiste en calcular iterativamente las corrientes de estator para $[k+2]$, y es con estas corrientes que se realiza el cálculo de la función de costo para la selección del estado del VSI a aplicar a la IM hexafásica, de la siguiente manera:

$$J = |i^*_{s\alpha\beta[k+2]} - i_{s\alpha\beta[k+2]}|^2 + \lambda_{xy}.|i^*_{sxy[k+2]} - i_{sxy[k+2]}|^2 \tag{2.55}$$

donde

$$|i^*_{s\alpha\beta[k+2]} - i_{s\alpha\beta[k+2]}|^2 = |i^*_{s\alpha[k+2]} - i_{s\alpha[k+2]}|^2 + |i^*_{s\beta[k+2]} - i_{s\beta[k+2]}|^2$$
$$|i^*_{sxy[k+2]} - i_{sxy[k+2]}|^2 = |i^*_{sx[k+2]} - i_{sx[k+2]}|^2 + |i^*_{sy[k+2]} - i_{sy[k+2]}|^2$$

La selección del WF es un tema actual de investigación, siendo abordado en varios trabajos [33, 34], debido a que una selección adecuada del WF permite minimizar el error en $x-y$ priorizando el seguimiento en $(\alpha-\beta)$. Por lo que en el siguiente capítulo se propone una técnica para la optimización de este factor de peso.

2.3 Resumen

En este capítulo se ha realizado una descripción del modelo matemático de la IM hexafásica asimétrica a utilizar en el presente trabajo, además de presentar la representación del sistema en el espacio de estados, la cual es utilizada para el algoritmo de control implementado. Se introdujo la definición del factor de peso, cuya selección constituye el tema principal de este Trabajo Final de Maestría.

Parte III

MÉTODO PROPUESTO

CAPÍTULO 3

DISEÑO ÓPTIMO DEL FACTOR DE PESO DE LA FUNCIÓN DE COSTO

La selección del factor de peso es un problema complejo, debido a que se trata de un problema de optimización multiobjetivo, reducido en ocasiones a la utilización de métodos heurísticos, buscando una solución sub-óptima al problema [13, 35, 36]. Sin embargo, en los últimos años han surgido trabajos buscando una solución óptima al problema, siendo un enfoque popular el uso de Redes Neuronales Artificiales como en [19].

El problema de optimización multiobjetivo puede generalizarse como una función vectorial $\mathbf{f}$ que mapea un conjunto de K parámetros (las variables de decisión) a un conjunto de D objetivos:

$$min/max(\mathbf{o}) = \mathbf{f}(\mathbf{p}) \tag{3.1}$$

sujetos a:

$$\begin{aligned} \mathbf{o} &= (o_1, o_2, ..., o_D) \in O \\ \mathbf{p} &= (p_1, p_2, ..., p_K) \in P \end{aligned} \tag{3.2}$$

donde $\mathbf{o}$ es el vector de variables objetivo y $\mathbf{p}$ el vector de variables de decisión, O es el espacio objetivo y P es el espacio de parámetros. O bien, expresando en términos de los elementos de cada vector:

$$min/max(o_i) = f_i(\mathbf{p}) \qquad \forall i = 1, 2, 3, \cdots, D. \tag{3.3}$$

En problemas de optimización multiobjetivo normalmente no existe una única solución, sino un conjunto de soluciones alternativas, entre las cuales es posible elegir la mejor solución para el caso estudiado, tomando como criterio las variables de decisión [37].

Este conjunto de soluciones alternativas se dicen entonces que son óptimas en el sentido de que no existen soluciones en el espacio de búsqueda que ofrezcan mejores resultados cuando todas las variables objetivos son consideradas. A estas soluciones se les denomina entonces Óptimos de Pareto.

3.1 Óptimos de Pareto

El concepto de Óptimos de Pareto para un problema de minimización puede definirse de la siguiente forma [38]: considénse dos vectores de decisión $\mathbf{p}_1, \mathbf{p}_2 \in P$. Entonces, se dice que $\mathbf{p}_1$ domina a $\mathbf{p}_2$, escrito $\mathbf{p}_1 \prec \mathbf{p}_2$ si:

$$f_i(\mathbf{p}_1) < f_i(\mathbf{p}_2) \tag{3.4}$$

y que $\mathbf{p}_1$ domina débilmente a $\mathbf{p}_2$, denotado por $p_1 \preceq p_2$ si:

$$f_i(\mathbf{p}_1) \leq f_i(\mathbf{p}_2) \tag{3.5}$$

El Frente de Pareto es el conjunto de todas las soluciones no dominadas, mientras que el Óptimo de Pareto es el conjunto de vectores que corresponde al Frente de Pareto. La solución de un problema multiobjetivo de optimización consiste entonces en encontrar un Frente de Pareto bien distribuido. En términos sencillos, los puntos solución son los pertenecientes a este Frente de Pareto, ya que para cualquier solución del Frente de Pareto no es posible disminuir una de las variables de decisión sin aumentar las demás. En la Figura 3.1 se observa un ejemplo de un Frente de Pareto, en él, los puntos de color verde son puntos pertenecientes al Frente de Pareto, en tanto que los demás puntos son puntos dominados por los del Frente de Pareto. Una vez obtenido el Frente de Pareto, la solución más conveniente debe ser elegida, según los criterios de diseño del sistema que se está optimizando.

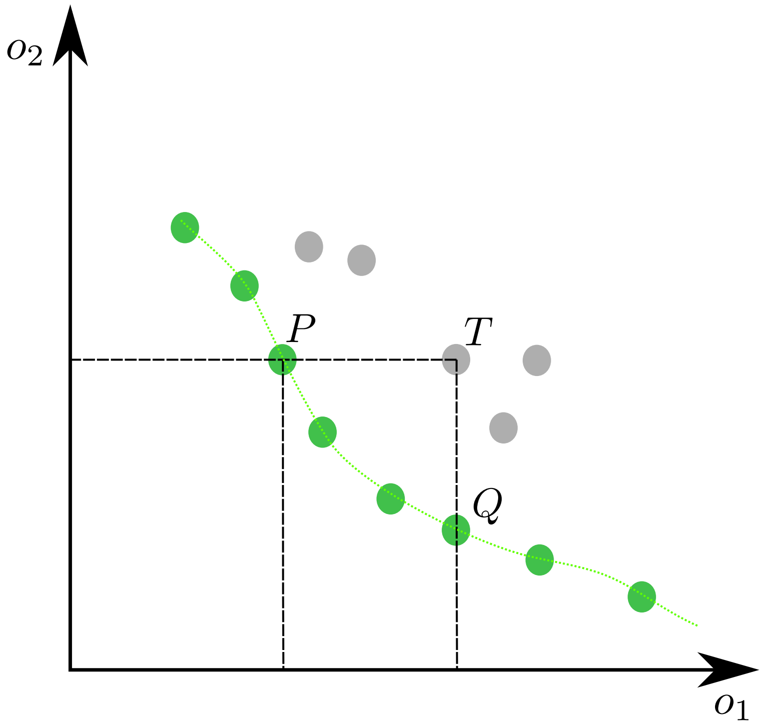

Figura 3.1: Ejemplo de un Frente de Pareto para un problema con dos variables de decisión. Los ejes o_1 y o_2 representan las variables de decisión. Los puntos que se encuentran sobre la línea verde punteada pertenecen al Frente de Pareto y dominan a los puntos de color gris.

Un frente de Pareto puede ser obtenido por diversas técnicas, entre ellas el Algoritmo Genético de Ordenamiento no dominado (NSGA, del inglés Non-dominated Sorting Genetic Algorithm) [39], el NSGA-II, que es una variante del anteriormente citado, con menor complejidad computacional [40], el NPGA (del inglés Niched Pareto Genetich Algorithm) [41, 42] y el algoritmo de Optimización de Enjambre de Partículas (PSO, del inglés Particle Swarm Optimization), el cual es utilizado en el presente trabajo.

3.2 Algoritmo de Optimización de Enjambre de Partículas (PSO)

El Algoritmo PSO es un algoritmo estocástico que se basa en una población (el enjambre), de soluciones posibles (las partículas) que se desplazan en un espacio de búsqueda siguiendo una serie de reglas matemáticas sencillas, propuesto en [43]. Fue inspirado en el comportamiento colectivo de animales, en los que se notado que el comportamiento de cada individuo del enjambre puede influenciar al comportamiento de todo el enjambre, y viceversa, compartiendo información útil y utilizándola junto con la experiencia personal para tomar decisiones y actuar. Este intercambio de información resulta beneficioso para la capacidad de búsqueda, o exploración, y ofrece una relación de compromiso con la velocidad de convergencia y el tiempo de búsqueda requerido.

En el algoritmo PSO las N partículas del enjambre se desplazan en el espacio de búsqueda, el cual es definido por el conjunto de todos los posibles valores para las variables de decisión. Cuando una partícula se desplaza en el espacio de búsqueda, el algoritmo evalúa la variable objetivo de acuerdo a una función de costo $f(\mathbf{p}_n)$. Usualmente, el objetivo del algoritmo PSO es el de minimizar esta función $f(\mathbf{p}_n)$. Cada partícula $\mathbf{p}_n$ posee una velocidad $\mathbf{v}_n$, la cual permite determinar su posición en el espacio de búsqueda para la siguiente iteración, según la ecuación [44]:

$$\mathbf{p}_{n[j+1]} = \mathbf{p}_{n[j]} + \chi\, \mathbf{v}_{n[j]} + \epsilon_{[j]} \tag{3.6}$$

donde $\chi \in [0, 1]$ es un valor que restringe la velocidad de cada partícula y ϵ un vector con elementos aleatorios uniformemente distribuidos, con valores típicos comprendidos en el intervalo $[-1, 1]$. La restricción sobre la velocidad se realiza para definir la influencia de la velocidad en la posición para la siguiente iteración, en tanto que ϵ es un desplazamiento aleatorio que permite aumentar el espacio explorado por el enjambre, buscando de esta manera evitar la convergencia del algoritmo a mínimos locales.

Para determinar la velocidad de cada partícula para cada iteración, se realiza el intercambio de información personal y global entre el enjambre y la partícula, esto se realiza a través de dos variables a saber, la guía personal $\mathbf{Pb}_n$, que consiste en la posición para la cual la partícula obtuvo la menor función de costo f, y la guía global $\mathbf{G_b}$, la cual consiste en la mejor posición encontrada por todo el enjambre. Estas variables se utilizan para calcular la velocidad de la partícula en la siguiente iteración según la ecuación:

$$\mathbf{v}_{n[j+1]} = \hat{w}\, \mathbf{v}_{n[j]} + r_1\, \hat{c}_1\, (\mathbf{Pb}_n - \mathbf{p}_{n[j]}) + r_2\, \hat{c}_2\, (\mathbf{G_b} - \mathbf{p}_{n[j]}) \tag{3.7}$$

donde

r_1, r_2: números aleatorios uniformemente distribuidos en el intervalo $[0, 1]$

c_1, c_2: factores que establecen la influencia de los conocimientos global y personal.

$\hat{w}$: factor de inercia. Controla el compromiso entre la exploración y la velocidad de convergencia.

Como el PSO está basado en un concepto simple, de sencilla implementación, con bajo costo computacional en tiempo y memoria en comparación a otros algoritmos de optimización basados en poblaciones, ha sido extendido al caso multiobjetivo [38, 45], en algunos casos con rendimiento similar a los obtenidos con algoritmos más complejos como el NSGA-II [46, 47], denominándose esta variante algoritmo de Optimización Multiobjetivo de Enjambre de Partículas (MOPSO, del inglés Multi-Objective Particla Swarm Optimization), el cual es descrito en la siguiente sección.

3.3 Algoritmo de Optimización Multiobjetivo de Enjambre de Partículas

El MOPSO se rige por las mismas ecuaciones presentadas en la sección anterior (3.6) y (3.7), radicando la principal diferencia en la selección adecuada de la guía global $\mathbf{Gb}$ y la guía personal $\mathbf{Pb}_n$ para cada iteración. Siendo un problema el hecho de que no existe un concepto claro del mejor personal y el mejor global para el caso en el que se busca la optimización para D objetivos. Una posible solución es la utilización de una función de costo igual a una suma ponderada de las variables objetivo [48], sin embargo esta solución posee el inconveniente de que es difícil controlar la relación de compromiso entre las variables objetivos, además de correr el riesgo de obtener un mínimo local en lugar de obtener óptimos globales. Por esta razón es utilizado el concepto de Óptimos de Pareto como función de costo, de modo que una solución pueda ser elegida del frente de Pareto. Este enfoque ha mostrado buenos resultados en trabajos previos [38, 43, 45], por lo que es utilizado en el presente trabajo.

El MOPSO hace uso de un repositorio $\mathbf{R}_p$ en el que se almacenan las soluciones no dominadas encontradas por el algoritmo en cada iteración. Esto se realiza de la siguiente manera: si una partícula encuentra una nueva posición no dominada, el algoritmo verifica si la actual posición domina a algún elemento de $\mathbf{R}_p$, removiéndolos si es así y agregando la actual posición de la partícula al repositorio. Si bien se han realizado trabajos en los que se ponen restricciones al repositorio, como el agrupamiento de partículas [49], se ha encontrado que esto puede llevar a oscilaciones y contracciones en el Frente de Pareto [50, 51], por lo que en la implementación realizada no se ponen restricciones al repositorio.

Al inicio de la optimización, $\mathbf{R}_p$ se encuentra vacío, y las posiciones y velocidades de las N partículas se inicializan con valores aleatorios, de modo que las partículas se encuentren dentro del espacio de búsqueda. La guía personal y la guía global para cada partícula es inicializada a la posición inicial de la partícula.

En cada iteración j las velocidades $\mathbf{v}_n$ y las posiciones $\mathbf{x}_n$ para cada partícula se actulizan según (3.6) y (3.7) respectivamente. Existe la posibilidad de que la posición así calculada para una partícula se encuentre fuera del espacio de posibles soluciones, esto se corrige utilizando el método "SHR" propuesto en [38], lo cual, asumiendo que la k-ésima componente de la partícula $\mathbf{x}_n$ es mayor a su correspondiente límite B, la magnitud de $\mathbf{v}_n$

es reducida según la expresión:

$$\mathbf{p}_{n[j+1]} = \mathbf{p}_{n[j]} + \sigma(\chi \mathbf{v}_{n[j]} + \epsilon_{[j]}) \tag{3.8}$$

con

$$\sigma = \frac{\mathbf{p}_{nk[j]} - B}{\chi \mathbf{v}_{nk[j]} + \epsilon_k} \tag{3.9}$$

de esta forma, la siguiente posición de la partícula se encontrará en el límite exacto del espacio de búsqueda.

Una vez asegurado que $\mathbf{x}_n$ se encuentra dentro del espacio de búsqueda se procede a evaluar las variables objetivo, agregando al repositorio $\mathbf{R}_p$ todas las soluciones que no son débilmente dominadas por algún elemento del repositorio, en tanto que todos los elementos del repositorio dominados por $\mathbf{x}_n$ son eliminados de $\mathbf{R}_p$, asegurando que el repositorio es un conjunto no dominado. La guía personal y la guía global para cada partícula en cada iteración es seleccionada del repositorio $\mathbf{R}_p$.

3.3.1 Selección de guías personales y global

La selección de $\mathbf{Pb}_n$ y $\mathbf{Gb}$ es una parte muy importante del MOPSO, por lo que debe elegirse una estrategia adecuada para ello. La selección de $\mathbf{Pb}_n$ resulta sencilla, debido a que si la posición actual de la n-ésima partícula, $\mathbf{p}_n$, domina débilmente a $\mathbf{Pb}_n$, entonces $\mathbf{Pb}_n = \mathbf{p}_n$, si $\mathbf{Pb}_n$ y $\mathbf{p}_n$ son mutuamente no dominados, entonces la nueva guía personal es seleccionada aleatoriamente entre ambas. Sin embargo, como todos los elementos del repositorio $\mathbf{R}_p$ son mutuamente no dominados y ningún elemento del repositorio es dominado por $\mathbf{p}_n$, entonces todos estos elementos de $\mathbf{R}_p$ son candidatos a guía global, pues, para alguna variable objetivo, todos los elementos son mejores que cada partícula del enjambre. Por tanto, debe establecerse una estrategia para seleccionar la guía global $\mathbf{Gb}$.

Existen tres principales estrategias para la selección de $\mathbf{Gb}$ [38]:

- ROUNDS: Elementos del repositorio que dominan a la menor cantidad de $\mathbf{p}_n$ son preferentemente asignados como guías globales. Los elementos ya asignados como guías no son considerados como guías de otras partículas hasta que todos los elementos hayan sido asignados, realizando este proceso iterativamente hasta que todas las partículas posean una guía global asignada. De esta forma, se promueve la diversidad en la población del repositorio, ya que este procedimiento atrae al enjambre hacia regiones menos pobladas del espacio de búsqueda, sin embargo es muy costoso computacionalmente.

- RANDOM: para un $\mathbf{p}_n$ dado, se toma el subconjunto de $\mathbf{Gb}$ que domine a $\mathbf{p}_n$ y se selecciona aleatoriamente un elemento de este conjunto, teniendo todos la misma probabilidad de ser seleccionados. Este método tiene el problema de que los elementos de $\mathbf{Gb}$ que se encuentran en regiones poco pobladas del Frente de Pareto tienden a dominar menos partículas, por lo que los elementos del repositorio se acumulan en una región del Frente.

- PROB: esta estrategia representa un compromiso entre las dos anteriores, se modifica RANDOM para favorecer la propagación hacia las zonas menos dispersas del espacio de búsqueda. Si $A_p = \{a \in R_p | a \prec p\}$, es el conjunto de elementos del repositorio que dominan a $\mathbf{p}$, y $P_a = \{p \in P | a \prec p\}$ es el conjunto de partículas dominadas por $\mathbf{a}$, entonces las guías son seleccionadas según:

$$\mathbf{Gb} = \begin{cases} a \in R_p \; con \; probabilidad \propto |P_a|^{-1} & si \; \mathbf{p}_n \in R_p \\ a \in A_{pn} \; con \; probabilidad \propto |P_a|^{-1} & si \; \mathbf{p}_n \notin R_p \end{cases} \tag{3.10}$$

Con repositorios pequeños el costo computacional de PROB no resulta alto, por lo que es el método seleccionado para la implementación realizada en este trabajo.

Con el MOPSO así definido, se procede a llevar estos conceptos al caso específico de estudio.

3.4 Aplicación del MOPSO al diseño del WF del control predictivo de la IM hexafásica asimétrica

En el caso estudiado en este trabajo se considera la función de costo del PCC de la IM hexafásica asimétrica, la cual, según la ecuación (2.54) es:

$$J = |i^*_{s\alpha\beta[k+2]} - i_{s\alpha\beta[k+2]}|^2 + \lambda_{xy}.|i^*_{sxy[k+2]} - i_{sxy[k+2]}|^2$$

El objetivo es el de optimizar el valor de λ_{xy}, de modo a obtener el menor error posible en el seguimiento de las corrientes en los planos $(\alpha - \beta)$ y $(x - y)$. Por tanto, la variable de decisión es λ_{xy}, mientras que los objetivos deben seleccionarse de modo que reflejen los errores en las corrientes mencionadas. Para el presente trabajo se seleccionó como objetivos el RMSE$i_{\alpha\beta}$ y el RMSEi_{xy}, definidos por las ecuaciones (3.11) y (3.12). Se realizó esta elección, en donde se agrupan los errores de cada plano en un sólo objetivo, debido a que se busca minimizar simultáneamente las corrientes en cada eje sin producir un deterioro significativo en las corrientes correspondientes al plano $(\alpha - \beta)$. Al definir la variable de decisión y los objetivos de esta forma, se posee un espacio de búsqueda con un grado de libertad, con dos objetivos a minimizar. De esta forma, el sistema quedaría como se muestra en la Figura 3.2, con el MOPSO calculando los Érentes de Pareto fuera de línea, para las condiciones de trabajo deseadas, y valores apropiados de λ_{xy} son luego proveídos al controlador, según el punto de operación.

$$\mathrm{RMSE}(i_{s\alpha\beta}) = \sqrt{\frac{1}{N}\left(\sum_{k=1}^{N}(i_{s\alpha}[k] - i_{s\alpha}^{*}[k])^2 + \sum_{k=1}^{N}(i_{s\beta}[k] - i_{s\beta}^{*}[k])^3\right)} \tag{3.11}$$

$$\mathrm{RMSE}(i_{sxy}) = \sqrt{\frac{1}{N}\left(\sum_{k=1}^{N}(i_{sx}[k] - i_{sx}^{*}[k])^2 + \sum_{k=1}^{N}(i_{sy}[k] - i_{sy}^{*}[k])^3\right)} \tag{3.12}$$

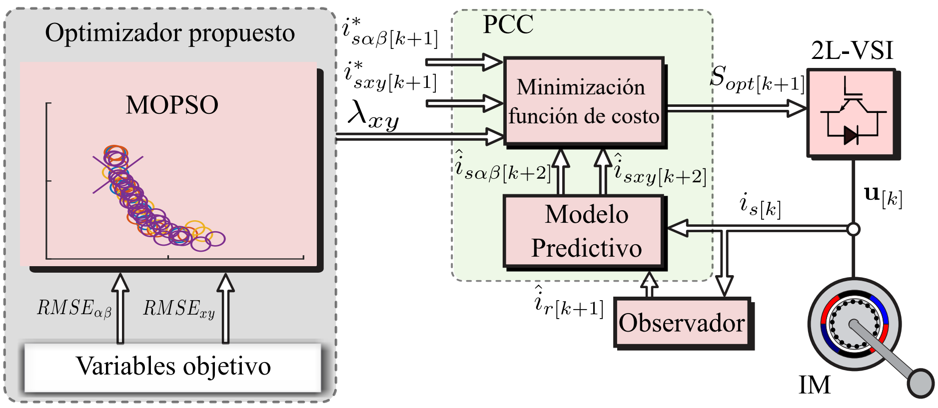

Figura 3.2: Diagrama de bloques del sistema propuesto. El MOPSO obtiene los Frentes de Pareto trabajando fuera de línea

3.5 Resumen

En este capítulo se presentó el concepto de Frentes y Óptimos de Pareto, además de las reglas matemáticas que rigen al algoritmo PSO y su generalización al caso objetivo, para finalmente definir la de decisión y los objetivos para el caso específico del PCC de la IM hexafásica asimétrica.

CAPÍTULO 4

RESULTADOS

En este capítulo se presentan los WF obtenidos con el MOPSO para diferentes velocidades de trabajo de la IM, además de los resultados de pruebas experimentales realizadas con estos valores y cómo estos resultados se comparan con un valor de WF de referencia, obtenido heurísticamente.

4.1 Entorno de simulación

4.1.1 Modelo de la IM hexafásica asimétrica

Se utiliza el entorno de simulación MATLAB/Simulink, en el cual se ha modelado la IM hexafásica conectada a un VSI hexafásico de dos niveles, con un voltaje del DC-Link $V_{DC} = 400$ V. Los parámetros eléctricos y mecánicos de la máquina se encuentran detallados en la Tabla 4.1, estos parámetros corresponden a la bancada de ensayo del Applied Power Electronics Technology Research Group (APET) de la Universidad de Vigo, España.

Parámetro	Valor	Parámetro	Valor
R_s	6.7 Ω	P	1
R_r	7 Ω	B_m	0.0004 $\times 10^{-3}$ N·m·s/rad
L_{ls}	5.85 mH	J	0.07 Kg·m^2/s^2
L_{lr}	55.7 mH		
L_m	708.5 mH		

Tabla 4.1: Parámetros eléctricos y mecánicos de la IM

Para aliviar el costo computacional de la simulación, se omite el estimador de corrientes del rotor, utilizándose directamente los valores calculados en el modelo.

El entorno se configura de modo que para cada velocidad de operación las referencias de corriente i_{qs}^* e i_{ds}^* tengan un valor de 1 A.

Se realizaron pruebas para tres frecuencias de muestreo: 8 kHz, 10 kHz y 16 kHz, realizándose la integración numérica por el método discreto (sin estados continuos) de Simulink, con 100 pasos por cada período de muestreo.

El entorno recibe como entradas la velocidad de operación del motor y el WF a ser analizado. Como salidas se tienen las referencias de corrientes $i_{s\alpha}^*, i_{s\beta}^*, i_{sx}^*, i_{sy}^*$ y las corrientes medidas $i_{s\alpha}, i_{s\beta}, i_{sx}, i_{sy}$. Estas salidas sirven de entrada al algoritmo del MOPSO para la obtención de los frentes de Pareto.

4.1.2 Parámetros del MOPSO

Como se indicó en la Sección 3.4, la variable de decisión constituye el WF de la función de costo del PCC, λ_{xy}, con los objetivos RMSE$i_{s\alpha\beta}$ y RMSEi_{sxy} definidos en (3.11) y (3.12) respectivamente. En la Tabla 4.2 se recopilan los parámetros del MOPSO.

Parámetro	Valor	Parámetro	Valor
c_1	1	χ	1
c_2	0.9	B	[0,1]
$\hat{w}$	0.6	N	10

Tabla 4.2: Parámetros del MOPSO. B: intervalo de búsqueda. N: número de partículas.

4.2 Obtención de los frentes de Pareto

Para cada frecuencia de muestreo se obtuvo frentes de Pareto para tres velocidades distintas, utilizando los RMSE definidos en (3.11) y (3.12). En las Figuras 4.1, 4.2 y 4.3 se observan los frentes obtenidos para 500 rpm, 1000 rpm y 1500 rpm, respectivamente, con 25 iteraciones por calibración, para la frecuencia de muestreo .

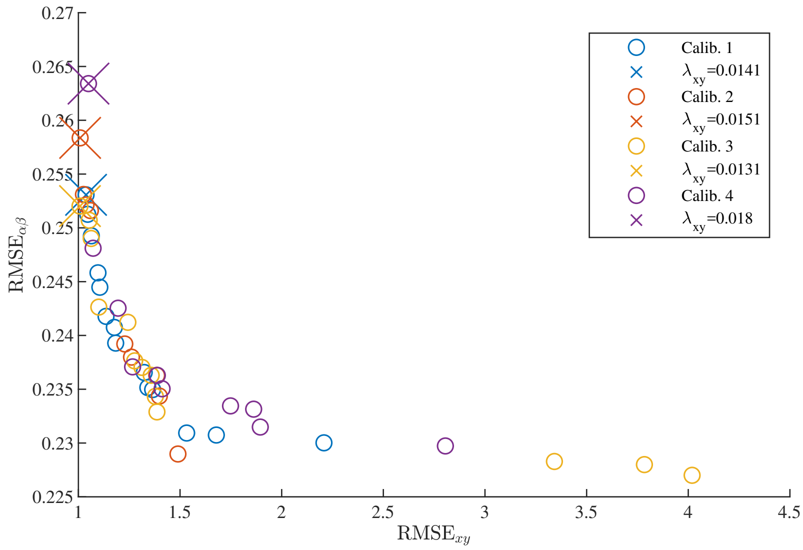

Figura 4.1: Frentes de Pareto para cuatro calibraciones obtenidas con 10 partículas y 25 iteraciones con $\omega_r^* = 500$ rpm, $f_s = 10$ kHz. Los WF óptimos para cada calibración se encuentran marcados con una X.

Estos valores de WF son luego validados por medio de pruebas experimentales, según las figuras de mérito definidas en la siguiente sección.

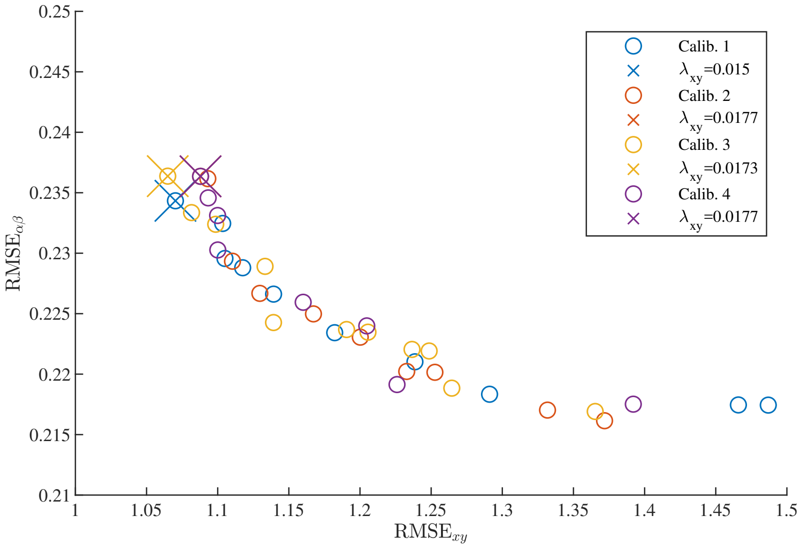

Figura 4.2: Frentes de Pareto para cuatro calibraciones obtenidas con 10 partículas y 25 iteraciones con $\omega_r^* = 1000$ rpm, $f_s = 10$ kHz. Los WF óptimos para cada calibración se encuentran marcados con una X.

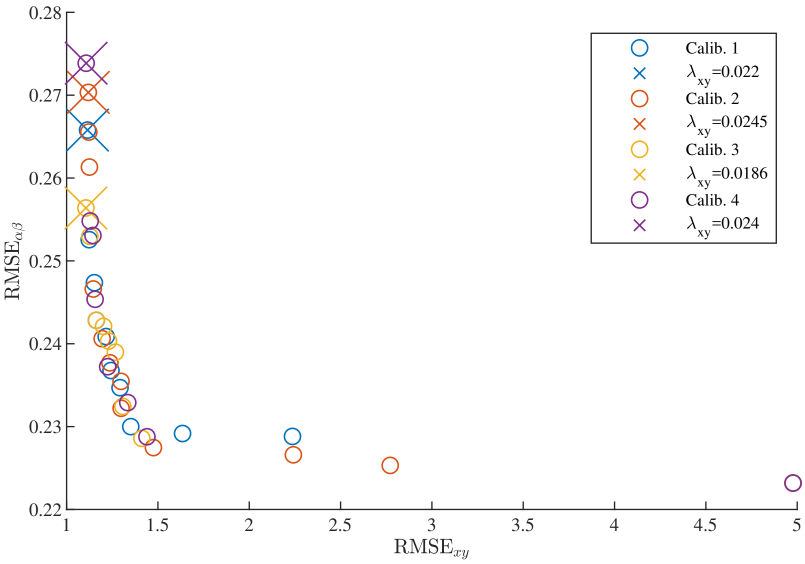

Figura 4.3: Frentes de Pareto para cuatro calibraciones obtenidas con 10 partículas y 25 iteraciones con $\omega_r^* = 1500$ rpm, $f_s = 10$ kHz. Los WF óptimos para cada calibración se encuentran marcados con una X.

4.3 Figuras de mérito

La técnica propuesta es evaluada en estado estacionario, en términos del RMSE entre las corrientes medidas y las de referencia del estator, en los planos $(\alpha - \beta)$ y $(x - y)$, para obtener el error en estado estacionario del seguimiento de corriente.

El RMSE se define por:

$$\mathrm{RMSE}(i_{s\Phi}) = \sqrt{\frac{1}{N}\sum_{k=1}^{N}(i_{s\Phi}[k] - i_{s\Phi}^{*}[k])^2} \tag{4.1}$$

donde $i_{s\Phi}$ son las corrientes medidas del estator, $i_{s\Phi}^{*}$ son las corrientes de referencia del estator y $\Phi \in \{\alpha, \beta, x, y\}$.

Además, se utiliza como figura de mérito el torque del rotor, el cual es medido para las distintas condiciones de trabajo y se evalúa la influencia que el WF tiene sobre el par generado.

4.4 Resultados Experimentales

El rendimiento del controlador con los valores de λ_{xy} obtenidos mediante el MOPSO es probado a través de pruebas experimentales, utilizando las figuras de mérito anteriormente citadas. A modo de comparación, se realizaron mediciones de valores arbitrarios. Estas pruebas fueron realizadas en la bancada de ensayo del Applied Power Electronics Technology Research Group (APET) de la Universidad de Vigo, España; consistente en un VSI hexafásico, compuesto por dos VSI trifásicos convencionales, utilizando un voltaje constante en el bus DC, obtenido de una fuente DC. El VSI es controlado por la plataforma de prototipado dSPACE MABXII DS1401, con MATLAB/Simulink. Los resultados fueron procesados utilizando un script de MATLAB. Los parámetros de la máquina son los mismos que se recogen en la Tabla 4.1.

Las mediciones fueron obtenidas mediante sensores de corriente LA 55-P s, con varias vueltas, de modo a mejorar la precisión en medidas de baja corriente. Estos sensores poseen un ancho de banda frecuencial desde DC hasta 200 kHz. Los valores obtenidos fueron digitalizados a través de un conversor analógico-digital de 16 bits. El ángulo del rotor de la IM hexafásica asimétrica es medido con un encoder incremental del tipo 1024 ppr, a partir de esta medición se realizó el cálculo de la velocidad. Un freno eléctrico fue utilizado como carga mecánica variable de la IM, el cual fue fijado a 1 A, de modo que $i_d^* = i_q^* = 1$ A. Un diagrama de bloques de la bancada se observa en la Figura 4.4.

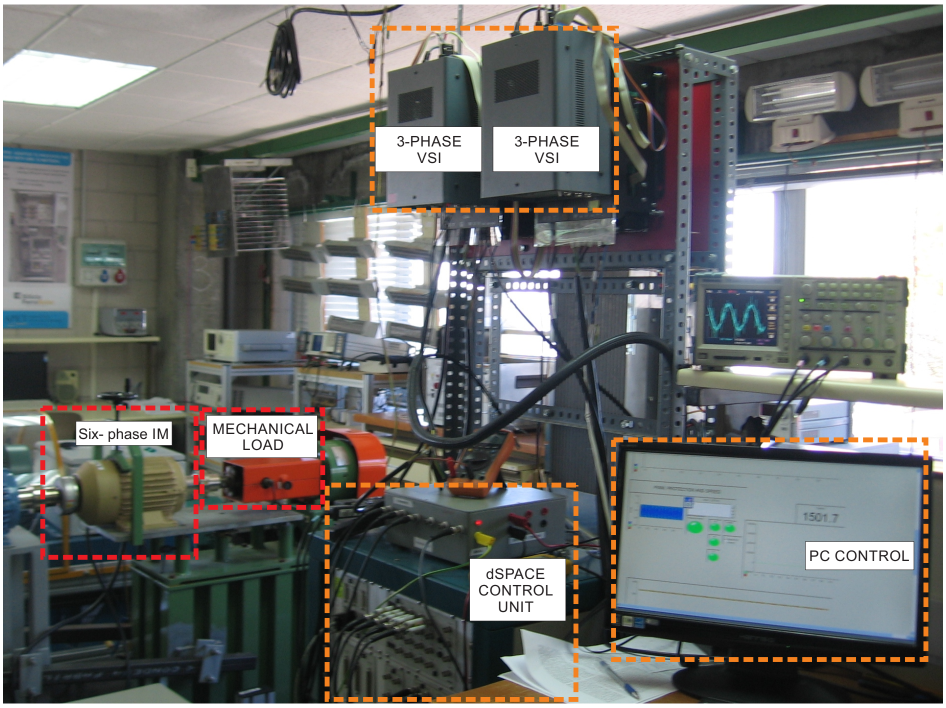

Figura 4.4: Diagrama de bloques de la bancada de prueba, incluyendo la IM, la plataforma dSPACE, el freno eléctrico y el VSI hexafásico.

Las evaluaciones según las figuras de mérito son tabuladas para cada una de las velocidades de referencia, para cada frecuencia de muestreo, en las Tablas 4.3 a 4.5, resaltando los valores obtenidos mediante los Frentes de Pareto. En ellas puede observarse que para $\lambda_{xy} = 0$ se obtienen errores en $(x - y)$ mayores que para los valores extraídos de los Frentes de Pareto, en tanto que para valores de λ_{xy} mayores a los obtenidos a partir de los Frentes de Pareto, se observa un deterioro en las figuras de mérito correspondientes al plano $(\alpha - \beta)$ sin obtenerse mejoras significativas en el plano $(x - y)$. Esto se debe principalmente a tres factores, la naturaleza discreta del VSI, las limitaciones físicas de la IM, ya que las corrientes en el plano $(x - y)$ representan las pérdidas en la IM, las cuales son imposibles de reducir a cero, y limitaciones propias del PCC, como el menor rendimiento a mayores valores de velocidad.

Además, puede observarse en la Tabla 4.4 que para un valor de $\lambda_{xy} = 1.2$, para el caso en que $\omega_r^* = 1500$ rpm, la máquina se vuelve inestable, en tanto que con $\lambda_{xy} = 2$ simplemente no arranca, por lo cual este valor fue excluido de la tabla. Del mismo modo, para la Tabla 4.5 los valores correspondientes a $\omega_r^* = 1500$ rpm fueron excluidos debido a que para estos valores la máquina se vuelve inestable, en tanto que para las demás velocidades, con valores de λ_{xy} mayores a los incluidos en la tabla la máquina no arranca.

Si bien el deterioro de las corrientes en $\alpha - \beta$ cuantificado en las Tablas 4.3 a 4.5 al aumentar el valor de λ_{xy} es numéricamente bajo, debido a la naturaleza del RMSE como figura de mérito, el deterioro de la corriente es notable, como se evidencia en las Figuras 4.5 a 4.6. Las mejoras en el plano $x - y$ se hacen también notorias, sin embargo, esto tiene repercusiones en el torque del motor.

		$\omega_r^* = 500$ rpm		
λ_{xy}	RMSE$_\alpha$	RMSE$_\beta$	RMSE$_x$	RMSE$_y$
0	0.0685	0.0659	3.6544	3.6467
0.0120	0.0752	0.0740	0.4471	0.4411
0.0190	0.0850	0.0840	0.3713	0.3683
0.1	0.1100	0.1074	0.2647	0.2658
1	0.2220	0.2207	0.1293	0.1302
2	0.2945	0.2909	0.1171	0.1171
		$\omega_r^* = 1000$ rpm		
λ_{xy}	RMSE$_\alpha$	RMSE$_\beta$	RMSE$_x$	RMSE$_y$
0	0.0739	0.077091	3.5964	3.5721
0.0179	0.0961	0.0944	0.4111	0.4108
0.0196	0.0961	0.0949	0.4025	0.3996
0.1	0.1306	0.1272	0.2898	0.2880
1	0.2648	0.2561	0.1463	0.1474
2	0.4147	0.4010	0.1280	0.1286
		$\omega_r^* = 1500$ rpm		
λ_{xy}	RMSE$_\alpha$	RMSE$_\beta$	RMSE$_x$	RMSE$_y$
0	0.0812	0.0804	3.4826	3.5658
0.0161	0.0725	0.0731	0.4253	0.4249
0.0196	0.0773	0.0764	0.4086	0.4113
0.1	0.1291	0.1261	0.3162	0.3154
1	0.3013	0.2952	0.1559	0.1562
2	0.4874	0.4768	0.1394	0.1391

Tabla 4.3: RMSE de corrientes de estator $\alpha - \beta$, $x - y$, con $f_s = 16$ kHz, a diferentes ω_r^*.

		$\omega_r^* = 500$	rpm	
λ_{xy}	RMSE$_\alpha$	RMSE$_\beta$	RMSE$_x$	RMSE$_y$
0	0.1049	0.0936	3.9747	3.9391
0.0131	0.1135	0.1126	0.6171	0.6138
0.0180	0.1230	0.1218	0.5294	0.5305
0.1	0.1594	0.1587	0.3826	0.3759
1	0.3114	0.3068	0.1882	0.1884
1.2	0.3335	0.3297	0.1835	0.1826
		$\omega_r^* = 1000$	rpm	
λ_{xy}	RMSE$_\alpha$	RMSE$_\beta$	RMSE$_x$	RMSE$_y$
0	0.1056	0.1088	4.0768	4.0130
0.0150	0.1215	0.1208	0.6409	0.6432
0.0177	0.1265	0.1260	0.6000	0.6002
0.1	0.1929	0.1919	0.4199	0.4187
1	0.3678	0.3698	0.2017	0.2005
1.2	0.4080	0.4085	0.1946	0.1955
		$\omega_r^* = 1500$	rpm	
λ_{xy}	RMSE$_\alpha$	RMSE$_\beta$	RMSE$_x$	RMSE$_y$
0	0.1462	0.1519	4.0806	4.0239
0.0186	0.1110	0.1125	0.6344	0.6366
0.0245	0.1173	0.1178	0.6019	0.6067
0.1	0.1980	0.1976	0.4792	0.4777
1	0.4484	0.4540	0.2187	0.2170
1.2	Uns	–	–	–

Tabla 4.4: RMSE de corrientes de estator $\alpha - \beta$, $x - y$, con $f_s = 10$ kHz, a diferentes ω_r^*.

		$\omega_r^* = 500$	rpm	
λ_{xy}	RMSE$_\alpha$	RMSE$_\beta$	RMSE$_x$	RMSE$_y$
0	0.1275	0.1236	4.2003	4.154
0.0172	0.1512	0.1505	0.6212	0.6231
0.0231	0.1576	0.1569	0.5881	0.5877
0.1	0.1936	0.1938	0.4507	0.4512
1	0.3703	0.3741	0.2357	0.2340
		$\omega_r^* = 1000$	rpm	
λ_{xy}	RMSE$_\alpha$	RMSE$_\beta$	RMSE$_x$	RMSE$_y$
0	0.1458	0.1498	4.4836	4.4340
0.0186	0.1608	0.1609	0.7230	0.7299
0.0241	0.1701	0.1680	0.6773	0.6721
0.1	0.2282	0.2286	0.4921	0.4879
0	0.4330	0.4392	0.2514	0.2474

Tabla 4.5: RMSE de corrientes de estator $\alpha - \beta$, $x - y$, con $f_s = 8$ kHz, a diferentes ω_r^*.

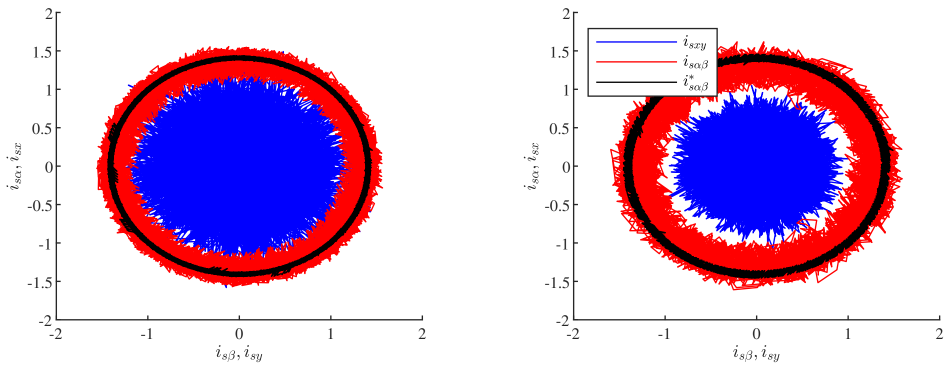

(a) $\lambda_{xy} = 0.0196$ (b) $\lambda_{xy} = 0.1$

Figura 4.5: Corrientes para $\omega_r^* = 1000$ rpm, $f_s = 16$ kHz con distintos valores de factor de peso: (a) $\lambda_{xy} = 0.0196$; (b) $\lambda_{xy} = 0.1$. Para cada caso, a mayor área roja, mayor error en el seguimiento de corriente en el plano $\alpha - \beta$

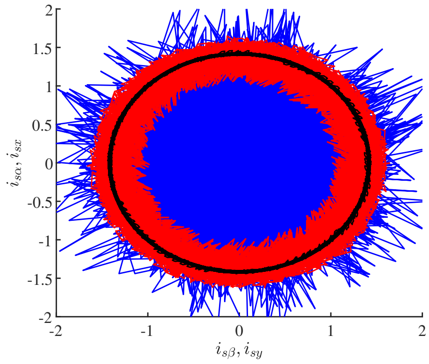

(a) $\lambda_{xy} = 0.0177$

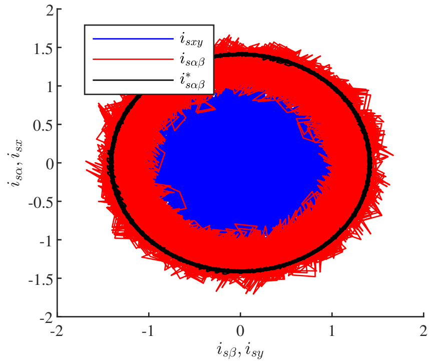

(b) $\lambda_{xy} = 0.1$

Figura 4.6: Corrientes para $\omega_r^* = 1000$ rpm, $f_s = 10$ kHz con distintos valores de factor de peso: (a) $\lambda_{xy} = 0.0177$; (b) $\lambda_{xy} = 0.1$. Para cada caso, a mayor área roja, mayor error en el seguimiento de corriente en el plano $\alpha - \beta$

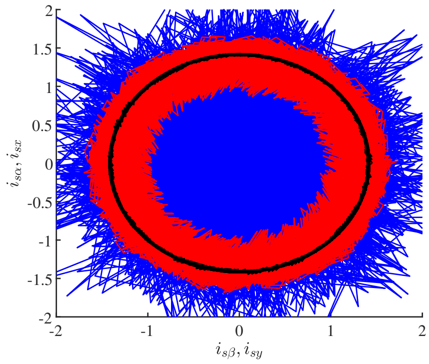

(a) $\lambda_{xy} = 0.0186$

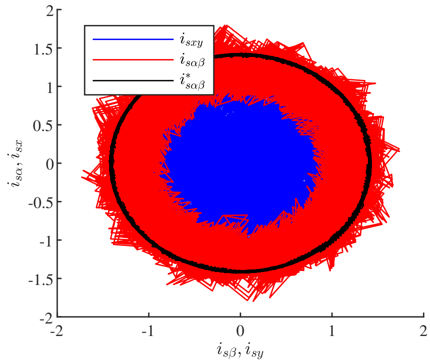

(b) $\lambda_{xy} = 0.1$

Figura 4.7: Corrientes para $\omega_r^* = 1000$ rpm, $f_s = 10$ kHz con distintos valores de factor de peso: (a) $\lambda_{xy} = 0.0177$; (b) $\lambda_{xy} = 0.1$. Para cada caso, a mayor área roja, mayor error en el seguimiento de corriente en el plano $\alpha - \beta$

Al aumentar el error de seguimiento en el plano $\alpha - \beta$, las variables relacionadas al torque y al flujo también son afectadas. Si la componente relacionada al par, i_q, no es capaz de alcanzar el valor de referencia, la capacidad de la IM de alcanzar el torque de referencia se verá reducida. Por otro lado, si la componente de la corriente relacionada al flujo, i_d, no es capaz de alcanzar el valor de referencia, el campo magnético será debilitado y, por tanto, también será debilitado el torque de la IM.

Esto queda evidenciado en las Tablas 4.6 y 4.7, donde se observan las corrientes $d - q$ y los torques obtenidos experimentalmente (como porcentajes del torque de referencia $T_{L(rated)}$) para 16 kHz y 10 kHz, respectivamente, a tres distintas w_r^*. Se incluye además la frecuencia media de conmutación ($f_{sw(avg)}$) para cada caso, la cual se ve afectada por el valor del factor de peso.

$\omega_r^* = 500$ rpm				
λ_{xy}	$i_{q(\text{med})}/i_q^*$ (pu)	$i_{d(\text{med})}/i_d^*$ (pu)	$T_L/T_{L(\text{rated})}$ (%)	$f_{\text{sw(avg)}}$ (kHz)
0.0196	0.97	1	98.33%	5.30
0.1	0.93	0.98	96.88%	5.30
1	0.86	0.96	83.1%	6.20
2	0.76	0.9	77.29%	6.30
$\omega_r^* = 1000$ rpm				
λ_{xy}	$i_{q(\text{med})}/i_q^*$ (pu)	$i_{d(\text{med})}/i_d^*$ (pu)	$T_L/T_{L(\text{rated})}$ (%)	$f_{\text{sw(avg)}}$ (kHz)
0.0196	0.96	0.99	95.42%	4.70
0.1	0.89	0.98	91.04%	4.70
1	0.81	0.94	80.83%	5.20
2	0.63	0.87	63.33%	5.45
$\omega_r^* = 1500$ rpm				
λ_{xy}	$i_{q(\text{med})}/i_q^*$ (pu)	$i_{d(\text{med})}/i_d^*$ (pu)	$T_L/T_{L(\text{rated})}$ (%)	$f_{\text{sw(avg)}}$ (kHz)
0.0190	0.96	0.99	94.17%	4.3
0.1	0.92	0.98	91.04%	4.30
1	0.78	0.93	75.00%	4.30
2	0.53	0.82	52.08%	4.80

Tabla 4.6: Influencia de λ_{xy} en el par de la IM a $f_s = 16$ kHz.

Del análisis de estas Tablas puede concluirse:

- A medida que λ_{xy} aumenta, para una ω_r^*, los errores de seguimiento de i_d^* y i_q^* son mayores. Las razones $i_{d(\mathrm{med})}/i_d^*$ y $i_{q(\mathrm{med})}/i_q^*$ se reducen, reduciendo el torque que puede alcanzar la IM se reduce.

- Si λ_{xy} se mantiene constante, a medida que ω_r^* aumenta, el torque que puede alcanzar la IM se reduce. Este hecho está relacionado con la frecuencia de muestreo y la frecuencia fundamental, ya que al aumentar ω_r^* el rendimiento del control de corriente se ve reducido.

- La frecuencia de conmutación aumenta al aumentar λ_{xy}. Esto ayuda a reducir el rizado en ambos subespacios.

$\omega_r^* = 500$ rpm				
λ_{xy}	$i_{q(\mathrm{med})}/i_q^*$ (pu)	$i_{d(\mathrm{med})}/i_d^*$ (pu)	$T_L/T_{L(\mathrm{rated})}$ (%)	$f_{\mathrm{sw(avg)}}$ (kHz)
0.0186	0.96	0.99	95.42%	3.50
0.1	0.89	0.98	90.83%	3.50
1	0.72	0.96	78.33%	4.10
2	0.70	0.94	75.63%	4.10
$\omega_r^* = 1000$ rpm				
λ_{xy}	$i_{q(\mathrm{med})}/i_q^*$ (pu)	$i_{d(\mathrm{med})}/i_d^*$ (pu)	$T_L/T_{L(\mathrm{rated})}$ (%)	$f_{\mathrm{sw(avg)}}$ (kHz)
0.0177	0.95	0.99	94.17%	3.10
0.1	0.86	0.98	85.21%	3.10
1	0.70	0.94	73.33%	3.50
2	0.62	0.93	61.46%	3.50
$\omega_r^* = 1500$ rpm				
λ_{xy}	$i_{q(\mathrm{med})}/i_q^*$ (pu)	$i_{d(\mathrm{med})}/i_d^*$ (pu)	$T_L/T_{L(\mathrm{rated})}$ (%)	$f_{\mathrm{sw(avg)}}$ (kHz)
0.0180	0.95	0.99	93.13%	2.80
0.1	0.84	0.98	83.33%	2.80
1	0.65	0.91	63.96%	3.00
2	0.51	0.87	51.04%	3.10

Tabla 4.7: Influencia de λ_{xy} en el par de la IM a $f_s = 10$ kHz.

CAPÍTULO 5

CONCLUSIONES Y TRABAJOS FUTUROS

En el presente Trabajo Final de Maestría se ha abordado el problema de optimización del factor de peso de la función de costo del Control Predictivo de Corriente de una Máquina de Inducción Hexafásica Asimétrica, utilizando el algoritmo de Optimización Multiobjetivo de Enjambre de Partículas. Las principales conclusiones se resumen a continuación:

- Se modeló y simuló la máquina de inducción hexafásica asimétrica.
- Se implementó el PCC de la IM hexafásica asimétrica.
- Se implementó el MOPSO para la optimización del WF de la función de costo utilizada en el PCC. Se obtuvieron Frentes de Pareto para distintos puntos de operación de la IM.
- Se obtuvieron varios Frentes de Pareto para los distintos puntos de operación, obteniendo resultados similares para todas las calibraciones de cada punto de operación,

a una cantidad baja de partículas e iteraciones, lo cual demuestra la repetitividad del MOPSO.

- Se realizaron pruebas experimentales con los valores óptimos obtenidos por el MOPSO. Estas pruebas experimentales muestran una mejoría en el desempeño del controlador al utilizar óptimos de Pareto para seleccionar el factor de peso respecto al desempeño obtenido mediante la utilización de valores arbitrarios del factor de peso, demostrando de esta forma ser un método sistemático para la selección del factor de peso, con ventajas respecto al método de prueba y error con el que normalmente es afrontado el problema de selección del factor de peso.

- La mejora en el desempeño se ve en la reducción del error de seguimiento en el plano $x - y$, asociado a las pérdidas, sin provocar un deterioro excesivo en el plano $\alpha - \beta$. Además, los valores obtenidos por el método propuesto demuestran un mejor rendimiento en cuanto al torque de la máquina, respecto a valores arbitrariamente seleccionados, demostrando la importancia de una selección adecuada del factor de peso.

- La selección de un factor de peso inapropiado puede causar inestabilidad o bien impedir el arranque del motor, por lo que es de vital importancia para el diseño del controlador. Este problema es notable principalmente a altas velocidades del rotor y baja frecuencia de muestreo, por lo que está relacionado con la razón entre la frecuencia de muestreo y la frecuencia fundamental, mientras más baja sea esta razón, la selección del factor de peso es de mayor importancia.

- El factor de peso tiene influencia directa sobre la frecuencia de conmutación del VSI, por lo que además de la relación de compromiso entre los seguimientos de corriente en los planos $\alpha - \beta$ y $x - y$, se tiene una relación de compromiso entre el rizado y las pérdidas de conmutación, la cual no ha sido analizada en este trabajo.

5.1 Trabajos Futuros

El diseño óptimo de los factores de peso de la función de costo para el control predictivo es un tema de investigación que aún no se ha abordado en profundidad, que dependiendo de la función de costo utilizada puede ser un punto crítico en el desempeño final del controlador, por este motivo existen varios puntos sobre los que puede profundizarse dentro de esta línea, como:

- Realizar un estudio sistemático de la sensibilidad del PCC al factor de peso, bajo diversas condiciones de corriente y velocidad, utilizando valores de Frentes de Pareto para cuantificar la mejora en el desempeño del controlador utilizando valores óptimos.
- Modificar la función de costo, de modo a incluir en ella otros parámetros como el número de conmutaciones o la distorsión armónica total (THD, del inglés Total Harmonic Distortion) y obtener valores óptimos de los factores de peso utilizando el MOPSO. La inclusión del número de conmutaciones como función de costo puede permitir contemplar la relación de compromiso entre el rizado y las pérdidas de conmutación, y la influencia que estas variables tienen en variables de salida como el torque del motor.
- Utilizar el MOPSO para el diseño de factores de peso de la función de costo del PCC para otras máquinas multifásicas.

REFERENCIAS

[1] M. J. Duran, E. Levi, and F. Barrero, "Multiphase electric drives: Introduction," *Wiley encyclopedia of electrical and electronics engineering*, pp. 1–26, 2017.

[2] E. Levi, "Advances in converter control and innovative exploitation of additional degrees of freedom for multiphase machines," *IEEE Transactions on Industrial Electronics*, vol. 63, no. 1, pp. 433–448, 2015.

[3] M. Jones, S. N. Vukosavic, D. Dujic, and E. Levi, "A synchronous current control scheme for multiphase induction motor drives," *IEEE Transactions on Energy Conversion*, vol. 24, no. 4, pp. 860–868, 2009.

[4] F. Barrero and M. J. Duran, "Recent advances in the design, modeling, and control of multiphase machines—part i," *IEEE Transactions on Industrial Electronics*, vol. 63, no. 1, pp. 449–458, 2016.

[5] A. Tenconi, S. Rubino, and R. Bojoi, "Model predictive control for multiphase motor drives–a technology status review," in *2018 International Power Electronics Conference (IPEC-Niigata 2018-ECCE Asia)*. IEEE, 2018, pp. 732–739.

[6] P. Gonçalves, S. Cruz, and A. Mendes, "Finite control set model predictive control of six-phase asymmetrical machines—an overview," *Energies*, vol. 12, no. 24, p. 4693, 2019.

[7] M. Bermúdez, C. Martín, I. González-Prieto, M. J. Durán, M. R. Arahal, and F. Barrero, "Predictive current control in electrical drives: an illustrated review with case examples using a

five-phase induction motor drive with distributed windings," *IET Electric Power Applications*, vol. 14, no. 8, pp. 1291–1310, 2020.

[8] M. Arahal, F. Barrero, S. Toral, M. Duran, and R. Gregor, "Multi-phase current control using finite-state model-predictive control," *Control Engineering Practice*, vol. 17, no. 5, pp. 579–587, 2009.

[9] M. J. Duran, J. Prieto, F. Barrero, and S. Toral, "Predictive current control of dual three-phase drives using restrained search techniques," *IEEE Transactions on Industrial Electronics*, vol. 58, no. 8, pp. 3253–3263, 2010.

[10] J. Rodas, F. Barrero, M. R. Arahal, C. Martín, and R. Gregor, "Online estimation of rotor variables in predictive current controllers: A case study using five-phase induction machines," *IEEE Transactions on Industrial Electronics*, vol. 63, no. 9, pp. 5348–5356, 2016.

[11] O. Gonzalez, M. Ayala, J. Doval-Gandoy, J. Rodas, R. Gregor, and M. Rivera, "Predictive-fixed switching current control strategy applied to six-phase induction machine," *Energies*, vol. 12, no. 12, p. 2294, 2019.

[12] I. Gonzalez-Prieto, M. J. Duran, J. J. Aciego, C. Martin, and F. Barrero, "Model predictive control of six-phase induction motor drives using virtual voltage vectors," *IEEE Transactions on Industrial Electronics*, vol. 65, no. 1, pp. 27–37, 2017.

[13] M. Ayala, J. Doval-Gandoy, J. Rodas, O. Gonzalez, R. Gregor, and M. Rivera, "A novel modulated model predictive control applied to six-phase induction motor drives," *IEEE Transactions on Industrial Electronics*, 2020.

[14] J. A. Riveros, F. Barrero, E. Levi, M. J. Durán, S. Toral, and M. Jones, "Variable-speed five-phase induction motor drive based on predictive torque control," *IEEE Transactions on Industrial Electronics*, vol. 60, no. 8, pp. 2957–2968, 2012.

[15] Y. Luo and C. Liu, "Pre- and post-fault tolerant operation of a six-phase pmsm motor using fcs-mpc without controller reconfiguration," *IEEE Transactions on Vehicular Technology*, vol. 68, no. 1, pp. 254–263, 2019.

[16] M. R. Arahal, F. Barrero, M. J. Duran, M. G. Ortega, and C. Martín, "Trade-offs analysis in predictive current control of multi-phase induction machines," *Control Engineering Practice*, vol. 81, pp. 105–113, 2018.

[17] J. Rodriguez and P. Cortes, *Predictive control of power converters and electrical drives*. John Wiley & Sons, 2012, vol. 40.

[18] P. Cortés, S. Kouro, B. La Rocca, R. Vargas, J. Rodríguez, J. I. León, S. Vazquez, and L. G. Franquelo, "Guidelines for weighting factors design in model predictive control of power converters and drives," in *2009 IEEE International Conference on Industrial Technology*. IEEE, 2009, pp. 1–7.

[19] T. Dragičević and M. Novak, "Weighting factor design in model predictive control of power electronic converters: An artificial neural network approach," *IEEE Transactions on Industrial Electronics*, vol. 66, no. 11, pp. 8870–8880, 2018.

[20] P. Karamanakos and T. Geyer, “Guidelines for the design of finite control set model predictive controllers,” *IEEE Transactions on Power Electronics*, vol. 35, no. 7, pp. 7434–7450, 2019.

[21] C. S. Lim, E. Levi, M. Jones, N. A. Rahim, and W. P. Hew, “Fcs-mpc-based current control of a five-phase induction motor and its comparison with pi-pwm control,” *IEEE Transactions on Industrial Electronics*, vol. 61, no. 1, pp. 149–163, 2013.

[22] M. Ayala, “Análisis de algoritmos de control predictivo basado en el modelo aplicado al accionamiento hexafásico,” Tesis de Maestría, Universidad Nacional de Asunción, Paraguay, 2017.

[23] E. Levi, R. Bojoi, F. Profumo, H. A. Toliyat, and S. Williamson, “Multiphase induction motor drives - a technology status review,” *IET Electric Power Applications*, vol. 1, no. 4, pp. 489–516, 2007.

[24] E. Levi, “Multiphase electric machines for variable-speed applications,” *IEEE Transactions on Industrial Electronics*, vol. 55, no. 5, pp. 1893–1909, 2008.

[25] J. Rodas, “Aplicación de estimadores on-line de variables rotóricas para la mejora de las prestaciones en variadores de velocidad multifásicos,” Tesis doctoral, Universidad de Sevilla, España, 2016.

[26] R. Gregor, “Aportaciones al control de corriente de máquinas de inducción de seis fases con doble devanado trifásico independiente y asimétrico,” Tesis doctoral, Universidad de Sevilla, España, 2016.

[27] A. G. Yepes, A. Vidal, J. Malvar, O. López, and J. Doval-Gandoy, “Tuning method aimed at optimized settling time and overshoot for synchronous proportional-integral current control in electric machines,” *IEEE Transactions on Power Electronics*, vol. 29, no. 6, pp. 3041–3054, 2014.

[28] F. Barrero, M. R. Arahal, R. Gregor, S. Toral, and M. J. Duran, “A proof of concept study of predictive current control for vsi-driven asymmetrical dual three-phase ac machines,” *IEEE Transactions on Industrial Electronics*, vol. 56, no. 6, pp. 1937–1954, 2009.

[29] F. Barrero, J. Prieto, E. Levi, R. Gregor, S. Toral, M. J. Duran, and M. Jones, “An enhanced predictive current control method for asymmetrical six-phase motor drives,” *IEEE Transactions on Industrial Electronics*, vol. 58, no. 8, pp. 3242–3252, 2011.

[30] I. Gonzalez-Prieto, M. J. Duran, J. J. Aciego, C. Martin, and F. Barrero, “Model predictive control of six-phase induction motor drives using virtual voltage vectors,” *IEEE Transactions on Industrial Electronics*, vol. 65, no. 1, pp. 27–37, 2018.

[31] J. J. Aciego, I. González Prieto, and M. J. Duran, “Model predictive control of six-phase induction motor drives using two virtual voltage vectors,” *IEEE Journal of Emerging and Selected Topics in Power Electronics*, vol. 7, no. 1, pp. 321–330, 2019.

[32] I. González-Prieto, M. J. Durán, M. Bermúdez, F. Barrero, and C. Martín, “Assessment of virtual-voltage-based model predictive controllers in six-phase drives under open-phase

faults," *IEEE Journal of Emerging and Selected Topics in Power Electronics*, vol. 8, no. 3, pp. 2634–2644, 2020.

[33] B. Majmunović, T. Dragičević, and F. Blaabjerg, "Multi objective modulated model predictive control of stand-alone voltage source converters," *IEEE Journal of Emerging and Selected Topics in Power Electronics*, vol. 8, no. 3, pp. 2559–2571, 2020.

[34] M. Novak, T. Dragicevic, and F. Blaabjerg, "Weighting factor design based on artificial neural network for finite set mpc operated 3l-npc converter," in *2019 IEEE Applied Power Electronics Conference and Exposition (APEC)*, 2019, pp. 77–82.

[35] M. Ayala, J. Rodas, R. Gregor, J. Doval-Gandoy, O. Gonzalez, M. Saad, and M. Rivera, "Comparative study of predictive control strategies at fixed switching frequency for an asymmetrical six-phase induction motor drive," in *2017 IEEE International Electric Machines and Drives Conference (IEMDC)*, 2017, pp. 1–8.

[36] M. Ayala, J. Doval-Gandoy, J. Rodas, O. Gonzalez, and R. Gregor, "Current control designed with model based predictive control for six-phase motor drives," *ISA Transactions*, vol. 98, pp. 496 – 504, 2020.

[37] E. Zitzler and L. Thiele, "Multiobjective evolutionary algorithms: a comparative case study and the strength pareto approach," *IEEE Transactions on Evolutionary Computation*, vol. 3, no. 4, pp. 257–271, 1999.

[38] J. E. Alvarez-Benitez, R. M. Everson, and J. E. Fieldsend, "A mopso algorithm based exclusively on pareto dominance concepts," in *International Conference on Evolutionary Multi-Criterion Optimization*. Springer, 2005, pp. 459–473.

[39] N. Srinivas and K. Deb, "Muiltiobjective optimization using nondominated sorting in genetic algorithms," *Evolutionary Computation*, vol. 2, no. 3, pp. 221–248, 1994.

[40] K. Deb, A. Pratap, S. Agarwal, and T. Meyarivan, "A fast and elitist multiobjective genetic algorithm: Nsga-ii," *IEEE Transactions on Evolutionary Computation*, vol. 6, no. 2, pp. 182–197, 2002.

[41] J. rey Horn, N. Nafpliotis, and D. E. Goldberg, "Multiobjective optimization using the niched pareto genetic algorithm," *IlliGAL report*, vol. 93005, 1993.

[42] J. Horn, N. Nafpliotis, and D. E. Goldberg, "A niched pareto genetic algorithm for multiobjective optimization," in *Proceedings of the First IEEE Conference on Evolutionary Computation. IEEE World Congress on Computational Intelligence*, 1994, pp. 82–87 vol.1.

[43] J. Kennedy and R. Eberhart, "Particle swarm optimization," in *Proceedings of ICNN'95-International Conference on Neural Networks*, vol. 4. IEEE, 1995, pp. 1942–1948.

[44] V. Gomez, N. Gomez, J. Rodas, E. Paiva, M. Saad, and R. Gregor, "Pareto optimal pid tuning for px4-based unmanned aerial vehicles by using a multi-objective particle swarm optimization algorithm," *Aerospace*, vol. 7, no. 6, p. 71, 2020.

[45] C. C. Coello and M. S. Lechuga, "Mopso: A proposal for multiple objective particle swarm optimization," in *Proceedings of the 2002 Congress on Evolutionary Computation. CEC'02 (Cat. No. 02TH8600)*, vol. 2. IEEE, 2002, pp. 1051–1056.

[46] M. I. Hlal, V. K. Ramachandaramurthya, S. Padmanaban, H. R. Kaboli, A. Pouryekta, T. Abdullah, and T. Ab Rashid, "Nsga-ii and mopso based optimization for sizing of hybrid pv/wind/battery energy storage system," *International Journal of Power Electronics and Drive Systems*, vol. 1, no. 1, pp. 463–478, 2019.

[47] A. Nourbakhsh, H. Safikhani, and S. Derakhshan, "The comparison of multi-objective particle swarm optimization and nsga ii algorithm: applications in centrifugal pumps," *Engineering Optimization*, vol. 43, no. 10, pp. 1095–1113, 2011.

[48] T. T. Mac, C. Copot, T. T. Duc, and R. De Keyser, "Ar.drone uav control parameters tuning based on particle swarm optimization algorithm," in *2016 IEEE International Conference on Automation, Quality and Testing, Robotics (AQTR)*, 2016, pp. 1–6.

[49] C. A. C. Coello, G. T. Pulido, and M. S. Lechuga, "Handling multiple objectives with particle swarm optimization," *IEEE Transactions on evolutionary computation*, vol. 8, no. 3, pp. 256–279, 2004.

[50] T. Hanne, "On the convergence of multiobjective evolutionary algorithms," *European Journal of Operational Research*, vol. 117, no. 3, pp. 553 – 564, 1999. [Online]. Available: http://www.sciencedirect.com/science/article/pii/S0377221798002628

[51] J. E. Fieldsend, R. M. Everson, and S. Singh, "Using unconstrained elite archives for multi-objective optimization," *IEEE Transactions on Evolutionary Computation*, vol. 7, no. 3, pp. 305–323, 2003.

Parte IV

ANEXOS

A

ARTÍCULOS PUBLICADOS

En el presente apéndice se realiza una recopilación de los artículos publicados en el marco de la Maestría, en el siguiente orden:

1. **H. Fretes**, M. Gomez-Redondo, E. Paiva, J. Rodas and R. Gregor, "A Review of Existing Evaluation Methods for Point Clouds Quality," 2019 Workshop on Research, Education and Development of Unmanned Aerial Systems (RED UAS), Cranfield, United Kingdom, 2019, pp. 247-252, doi: 10.1109/REDUAS47371.2019.8999725.

2. E. Paiva, M. Gomez-Redondo, J. Rodas, Y. Kali, M.Saad, R. Gregor, and **H. Fretes**, "Cascade First and Second Order Sliding Mode Controller of a QuadRotor UAV based on Exponential Reaching Law and Modified Super-Twisting Algorithm," 2019 Workshop on Research, Education and Development of Unmanned Aerial Systems (RED UAS), Cranfield, United Kingdom, 2019, pp. 100-105, doi: 10.1109/REDUAS47371.2019.8999711.

3. F. Martinez, T. Morel, H. Fretes, J. Rodas, Y. Kali and R. Gregor, “Model Predictive Current Control of Dual-Mode Voltage Source Inverter Operations: Islanded and Grid-Connected,” 2020 5th International Conference on Renewable Energies for Developing Countries (REDEC), Marrakech, Morocco, Morocco, 2020, pp. 1-6, doi: 10.1109/REDEC49234.2020.9163850.

Además, se incluye un artículo redactado en el marco del presente Trabajo Final de Maestría, enviado a revista y pendiente de aprobación:

4 **H. Fretes**, J. Rodas, J. Doval-Gandoy, V. Gomez, N. Gomez, M. Novak, and T. Dragičević, “Pareto Optimal Weighting Factor Design of Predictive Current Controller of a Six-Phase Induction Machine based on Particle Swarm Optimization Algorithm”

A.1 Artículo 1

A Review of Existing Evaluation Methods for Point Clouds Quality

Hector Fretes, Marcos Gomez-Redondo, Enrique Paiva, Jorge Rodas, and Raul Gregor

Abstract— **One problem in 3D reconstruction from aerial photographs is the evaluation of the point clouds quality. For point clouds, in general, different authors evaluate their results in different ways. This paper analyzes the existing evaluation methods for the point cloud quality and a new discussion regarding their applicability to aerial photographs is opened. Some of these methods are chosen based on practical issues and applied to a pair of reconstructions. The principal conclusion is that objective methods are the most interesting in photogrammetry applications, particularly the comparison between two point clouds.**

Index Terms— **Aerial Photogrammetry, Digital Photogrammetry, Review, Point Cloud, 3D Reconstruction.**

NOMENCLATURE

DEM	Digital Elevation Model.
DTM	Digital Terrain Model.
GCP	Ground Control Point.
MOS	Mean Objective Score.
ODM	OpenDroneMap.
PSNR	Peak Signal-to-Noise Ratio.
RMS	Root Mean Square.
RMSD	Root Mean Square Deviation.
SFM	Structure From Motion.
UAV	Unmanned Aerial Vehicle.

I. INTRODUCTION

NUMEROUS studies have been made with different reconstruction programs such as Pix4D, Agisoft, and OpenDroneMap, but they mainly compare the advantages and disadvantages of each one in terms of cost, accessibility to the source code, and other aspects rather than objective analysis [1]. For instance, in a study of the feasibility of using a smart camera as the payload for a UAV, a reconstruction with ODM is obtained but the point cloud analysis is not mentioned [2]. Although [3] mainly focus on the design of a low-cost tri rotor UAV, a reconstruction is performed and the results offered by Pix4D are presented with an estimated error that is calculated on the same software from some parameters such as the flight altitude and camera optics. Some authors describe an UAV mapping workflow and suggest some recommendations for the process, present initiatives that facilitate the gathering, hosting and sharing of user-contributed UAV imagery and also open software for digital photogrammetry [4] as well as open hardware [1]. This suggests that the number of 3D reconstructed scenes will be increased notably in the future, given that any user may share and access to data as well as open resources. It is also remarkable the number of works in the segmentation of point clouds, which attempt to extract information from 3D Point clouds, through artificial intelligence algorithms [5] or new descriptors [6]–[8].

M. Gomez-Redondo, H. Fretes, E. Paiva, J. Rodas and R. Gregor are with the Laboratory of Power and Control Systems, Facultad de Ingeniería, Universidad Nacional de Asunción, Luque 2060, Paraguay (e-mail: gomezredondomarcos@gmail.com; hectorfretesac@gmail.com; engapaga@gmail.com; jrodas@ing.una.py; rgregor@ing.una.py).

However, there is not yet a standard in the evaluation of 3D reconstructions in digital aerial photogrammetry, namely, point clouds. The main reason may be thought to be that the complete process is very extensive and authors generally evaluate only a part of the whole reconstruction procedure. For example, a factor involved into the process is the matching process, which is directly related with the number of points in the cloud, noise and affect the quality of the reconstruction, but it is a whole universe in computer science [9]. Taking that into account, this paper reviews point clouds quality evaluation methods in order to propose a standard to aerial reconstructions evaluation, namely, to researchers not very interiorized into computer science. In this way, researchers without too much knowledge could have a standardized method to determine the quality of the reconstruction and compare their results, without too much effort. In the following section, a variety of evaluation methods are presented and classified. In section III the most important evaluation methods for point clouds are summarized. In section IV there is an evaluation example and finally, some conclusions are presented.

II. BRIEF REVIEW OF THE EVALUATION PROCESS IN WORKS PRESENTED TO THE DATE

The evaluation methods can be classified into two major groups, subjective assessment methods and objective quality metrics.

A. Subjective assessment methods

These methods rely on qualitative analysis of the point clouds, based primarily on visual quality of the cloud and practical issues. For example, a sparse cloud is obtained in [10] and the evaluation is just a qualitative analysis of the DEM they have obtained. In another work, a 3D reconstruction system is proposed [11] and is verified through qualitative evaluation of experimental results for a variety of scenes. In [1] a comparison between commercial systems versus open-source systems is made. The author compares practical issues rather than the quality of the obtained reconstruction.

There is another evaluation method known as Mean Opinion Score (MOS), which consists of a subjective analysis of point clouds. The author in [12] present a codec that may be used for high rate transference of point clouds (data compression). In [13] is stated that current state-of-the-art objective metrics do not predict well visual quality, especially under typical distortions such as compression. The geometric distance, using RMS or Hausdorf distance, is applied to point-point, point-plane, and PSNR. Then the author shows the MOS and Point Cloud Quality Rating. In [14] another MOS evaluation is done. The author classifies the evaluation into objective, which is performed by a computer, and subjective, which is performed by the human. He also remarks about the importance of subjective evaluation to reaffirm the correctness of objective evaluation methods. After a brief review, he proposes a subjective evaluation model and some criteria for its application, finishing with an experiment. In [15] a correlation between the objective and subjective scores is assessed. As these works are centered to communication systems the MOS is useful, but when it comes to planialtimetric study, these studies do not seem to be applicable. Furthermore, subjective methods are time and cost expensive, and the reliability of the evaluations can be objectionable. For these reasons, a wide majority of scene reconstruction works use objective quality metrics in order to evaluate their results.

B. *Objective quality metrics*

Objective quality metrics rely on the definition of a parameter of the point cloud and obtaining a metric involving this parameter as the evaluation. Typically, these metrics involve measurements such as euclidean distances, angular distances, reprojection errors, ground control points location, number of points, and may involve the comparison between the evaluated point cloud and a reference model.

There exists some objective quality metrics that can be obtained exclusively from the evaluated point cloud. In [16] 3D point clouds are utilized for landslide scarp recognition. The quality of the 3D model is quantified in terms of point spacing in the cloud and point density, which gives a more complete evaluation of the model than the number of points in the cloud. In [17] a framework for 3D reconstruction from aerial images is presented and its results are compared against the ones of [18] in terms of the number of good-considered points, the mean error projection and execution time. But the more interesting could be the mean error projection [19], [20], because it gives an idea of the noise present in the point cloud.

Finally, the most common way to evaluate the quality seems to be the comparison against a reference [21], [22], [23], [24]. However, there are different kinds of references, depending on the case of study. We differentiate two major groups. The first, in which the exact model is known beforehand. The second, where you have a point cloud obtained by some other means.

1) *Exact model:*

a) Digital model: In some cases, the exact digital model is known, so you can generate a point cloud from it. That is the case of [25], where an evaluation of machining allowance of precision castings is made by comparing 2 point clouds, one of the model and one obtained by measurements. They analyse and compare these two taking into account some characteristics like plane angle, plane-plane distance, point-plane distance, shape ratio, size ratio. In [26] a simulation environment, FEATS, is presented. With this environment, the corresponding ground truth 3D point coordinate for each reconstructed 3D point is known, so that the error between these two points is easily calculated. In [27], a surface normal estimation for a set of unorganized points is revisited. They use available online data for their experiments. They propose measuring the average error per point in degrees' since their interest focus on surface normal estimation accuracy. This could be an interesting option for evaluating surface normals, rather than the cloud point. They test the algorithm rather than the point cloud. This kind of comparisons are really demonstrative but the need of the exact model in order to evaluate the reconstruction poses a problem for aerial photogrammetry, in which said model is not available.

b) Real model: The comparison could also be made against empirical measurements of the scene, which is not either a practical method when it comes to aerial photogrammetry, because of the time and cost demands of obtaining the model. In [28] they evaluate the quality of a commercial SFM Dense multi View 3D reconstruction software. In order to do this, a contrast against total station data and range scan data is performed. The author shows representative illustrations of the distance between different parts of the cloud points. Afterward, a table of Euclidean distances between different points is shown, comparing the results of the SFM-DMVR with the other data sources and then with the empirical measurements on the real monument. This last method was also used in [29]. In 2011, [30] compares different variants of the Hough transform regarding their reliability in detecting planes. They also introduce a new approach to design the accumulator. In concern with the evaluation, they made a quantitative as well as a qualitative evaluation of all the variants in five different scenes, taking into account the number of planes detected, angles and also the time consumed by every variant. In this paper, the evaluation is a comparison against a real model where the planes are known beforehand. So these characteristics are also representative in case of having two point clouds. They also conclude that Randomized Hough Transform is the method of choice when dealing with 3-dimensional data due to the time performance, but as far as it seems, the scene must be multiplanar rather than curve in order to use these evaluations. In [31] the analysis of the Super-Sauze landslide is performed. They compare two data sets and obtain a velocity profile of the land. They evaluate the quality of the DTM obtained so as to validate their results. The evaluation consists in quantifying the error by comparing 199 GCP locations to their measured locations giving a mean error and standard deviation in meters. In [32] the 3D models obtained are validated using field measurements of objects in the scene and 3D surfaces obtained by total stations as reference. The use of total stations allows obtaining a reference with a predefined accuracy and resolution to contrast the results.

2) Point cloud obtained by other methods: Another approach consists in the comparison of point clouds obtained by different methods, software or technologies. This is the more easily applicable method regarding aerial photogrammetry. In [31] they also compare 2 DTMs of the same scene and give the RMS and maximum deviations for this validation. In [33] an open-source-based process pipeline to develop a 3D model is described. An analysis of popular feature detectors is made, comparing a maximum number of robust feature keypoints detected, average computation time and even distribution of keypoints. The suitability of feature detectors for different scenes is also studied, based on repeatability and a high number of correspondences for each detector in a given scene. The relative accuracy of the 3D point clouds obtained is then analyzed by comparison with the Pix4D output using the Euclidean distances between pairs of clouds. In 2018, GRAPHOS has been introduced [34]. It is another open-source software that can process the imagery up to the dense point cloud. It is missing only the georeferencing for the full reconstruction. It mainly has an educational purpose but it also presents a metric for the point cloud evaluation, the median absolute deviation (MAD). In [35] a rapid 3D reconstruction method based in image queue, considering continuity and relevance of UAV camera images is presented. The method is first evaluated using the DTU Robot Image Data Sets [36] by comparison of the clouds obtained with the proposed method and the clouds provided by the dataset. Then is tested with aerial images taken from UAV's flights, the results of these tests are analyzed in terms of the number of points in the final clouds.

III. Interesting evaluation methods for planialtimetric aplications

A. Objective evaluation metrics

These methods seem to be the most appropriate in aerial photogrammetry. The most popular are P2Point and P2Plane. These two evaluate mostly the noise present in the cloud point. For any of these methods, the definition of a distance function is needed. There are two standard distances: RMSD and Hausdorff metric.

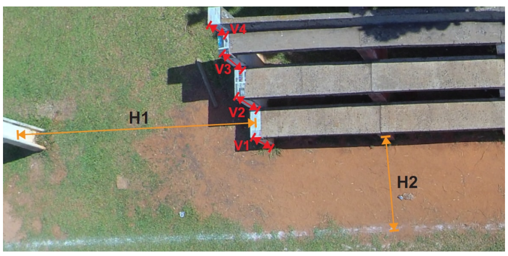

Fig. 1. Measured distances in the scene.

TABLE I

Empirical measuremets in the scene. Results for the euclidean norm of some segments in the cloud obtained by WebODM.

Segment	Point cloud distance [cm]	Measured distance [cm]	Error [cm]	Percentage error (%)
H1	497	487	-10	2.05
H2	194.2	180	-14	7.77
V1	69	69	0	0
V2	51	56	5	8.93
V3	49	56	7	12.5
V4	47	30	17	56.67

B. Direct comparison of some metric.

Another existing method employed into the cloud point evaluation, however, its simplicity, is to take measurements on the real scene and then contrast some distances and angles with the obtained on the reconstruction. This method is useful when the empiric measurement does not represent an obstacle, namely, small scenes and regular geometric shapes (planes, circles) so as to obtain all the information needed without too much effort. Another aspect of this analysis is that you only need one point cloud, given that you compare the reconstruction directly with the scene. One problem this method has is that a dense point cloud is needed, otherwise, the determination of points may be difficult to achieve. This kind of analysis could be applied in photogrammetry of urban areas or wherever the model could be considered as multiplanar, maybe with the help of some segmentation method for obtaining the different planes in the scene.

IV. Results and discussion

For the evaluation, a set of 13 aerial images from an altitude of 20 meters were used. Photographs were taken with the Autel X-Star Premium drone. These photographs were used for the reconstruction of two point clouds. One point cloud with WebODM and the other with Regard3d.

For the comparison against the real model, measurements of a set of six segments were taken in the scene as they are shown in Fig. 1 and tabulated in TABLE I and TABLE II.

The problem found with this method is that human error might be introduced during measurement, from both the scene and the cloud, especially when a segment is not easily

TABLE II

Empirical measuremets in the scene. Results for the euclidean norm of some segments in the cloud obtained by Regard3D.

Segment	Point cloud distance [cm]	Measured distance [cm]	Error [cm]	Percentage error (%)
H1	497	487	-4.41	2.05
H2	176	180	4.2	2.22
V1	69	69	-6.69	0
V2	58	56	1.19	3.57
V3	56	56	-2.7	0
V4	34	30	0.2	13.33

TABLE III
DISTANCES BETWEEN CLOUDS

Method	Mean	Std. deviation
Point-point	0.629	0.540
Point-plane	0.0.552	0.454

identifiable in the cloud, as in the case of the segment V4 in TABLE I. Low point density and noise in the region of interest are factors that increase the probability of human error.

Afterwards, both cloud points were compared using point-point and point-plane distance and the results are presented in TABLE III.

Fig. 2 shows the distribution of the distances along with the scene and in Fig. 3 a histogram of this distribution is presented, in which the number of points against the distance is plotted.

It can be seen that the highest distances between the clouds appear at the edges of the scene, where the radial distortion existing in the cloud reconstructed with ODM is maximum, while in the center of the models obtained the distances between them are low, which shows a high correspondence between the two models in that area.

The results of the point-plane distance measurement are given by Fig. 4 and Fig. 5. It can be seen that the mean distance is lower than the one obtained for the point-point distance, and even in the regions where the cloud obtained with WebODM presents high distortion, the distance is lower for the point-plane distance. This indicates that even though distortion and the error for individual points of the scene are high, the model can still be representative of the scene, particularly for applications such as obtaining a Digital Elevation Model of the scene.

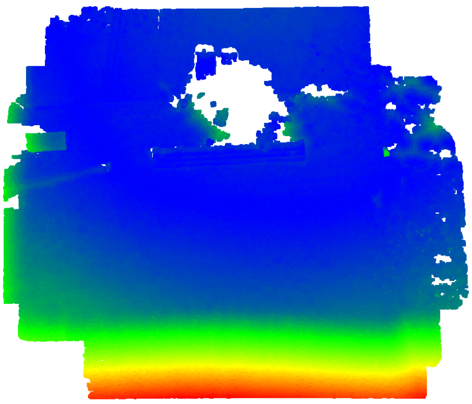

Fig. 2. Point to point distances between clouds.

V. CONCLUSIONS AND FUTURE OF POINT CLOUD EVALUATION

Although subjective methods could provide a preliminary evaluation of a point cloud, they are not of interest for aerial photogrammetry, in which accuracy and precision are required by most applications, because in order to provide a reliable result require evaluation by various subjects, which impacts in time and monetary costs.

Direct measurement in the scene for comparison against the point cloud should be the ideal evaluation method, but

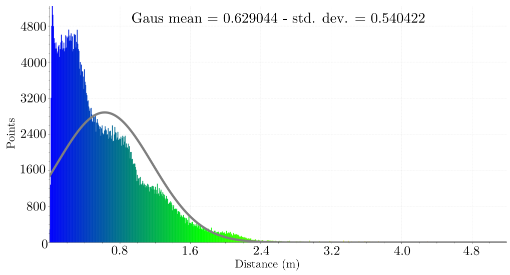

Fig. 3. Point to point distances histogram.

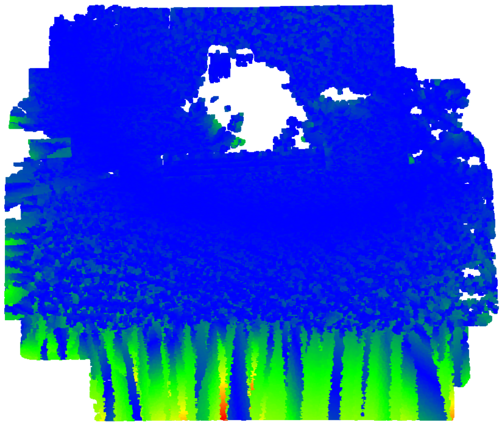

Fig. 4. Point to plane distances between clouds.

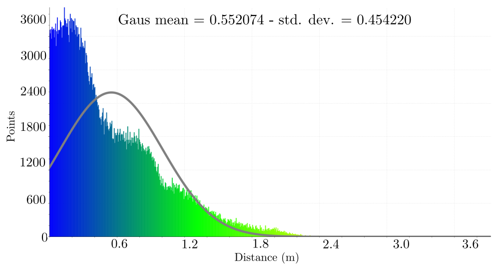

Fig. 5. Point to plane distances histogram.

becomes impractical when it comes to digital photogrammetry applied to aerial photographies, because of the size of the scenes and the potential measurement errors introduced by low point density and noise in the clouds.

The most interesting evaluation method for this case seems to be the comparison between two point clouds obtained by different means, which reduces human interference and guarantees less error in the evaluation of the cloud obtained. The comparison method between the clouds depends highly on the application of the point cloud. If the main application is the utilization of the cloud for planialtimetric studies and DEMs, the point-plane comparison method provides a better evaluation of the cloud, because points with high individual error can still be representative of the surfaces studied. It is noted that for a complete evaluation of a cloud, evaluation by two or more methods should be realized, as an unique objective metric does not necessarily correlate to good visual quality, and a particular method could fit better for a certain application, such as the aforementioned point-plane distance for DEMs.

Future challenges in evaluation methods include the characterization of surfaces in the model, as current evaluation methods, such as the comparison of GCP location and point-point distance, provide metrics for individual points but ignore the regions of the cloud between those points. Techniques such as point cloud segmentation [7], [37] could be explored for this purpose, as the could provide boundaries information which could help in the characterization of surfaces in the scene, while eliminating disparities between different data sets of the same scene produced over time (such as vegetation growth, constructions, among others).

Another challenge is the correlation between the given metrics and the visual quality of the point cloud. In this aspect, segmentation could also provide new metrics in the form of object classification and identification [5], where the number of objects detected could give a metric that correlates to the visual quality of the point cloud.

This correlation between the metrics and visual quality, the surface characterization, and the development of an objective metric that comprises the existing metrics are the main goals of research on evaluation methods, in order to simplify the evaluation process into a unique metric for every possible application of the point cloud.

Acknowledgment

This publication was made in the framework of the project PINV15-0136 called "Vehículos aéreos no tripulados (UAV) en aplicaciones de fotogrametría para el análisis planialtimétrico y cálculo de volumen" funded by Consejo Nacional de Ciencia y Tecnología (CONACYT) from Paraguay.

References

[1] P. Burdziakowski, "Evaluation of open drone map toolkit for geodetic grade aerial drone mapping–case study," in *17th International Multidisciplinary Scientific GeoConference SGEM 2017*, 2017.

[2] J. Park, H. Jeong, J. Kim, and C. Choi, "Development of open source-based automatic shooting and processing uav imagery for orthoimage using smart camera uav," *The International Archives of Photogrammetry, Remote Sensing and Spatial Information Sciences*, vol. 41, p. 941, 2016.

[3] A. Segales, R. Gregor, J. Rodas, D. Gregor, and S. Toledo, "Implementation of a low cost uav for photogrammetry measurement applications," in *2016 International Conference on Unmanned Aircraft Systems (ICUAS)*. IEEE, 2016, pp. 926–932.

[4] P. Johnson, B. Ricker, and S. Harrison, "Volunteered drone imagery: Challenges and constraints to the development of an open shared image repository," 2017.

[5] A. Aijazi, P. Checchin, and L. Trassoudaine, "Segmentation based classification of 3d urban point clouds: A super-voxel based approach with evaluation," *Remote Sensing*, vol. 5, no. 4, pp. 1624–1650, 2013.

[6] G. Arbeiter, S. Fuchs, R. Bormann, J. Fischer, and A. Verl, "Evaluation of 3d feature descriptors for classification of surface geometries in point clouds," in *2012 IEEE/RSJ International Conference on Intelligent Robots and Systems*. IEEE, 2012, pp. 1644–1650.

[7] B. Douillard, J. Underwood, N. Kuntz, V. Vlaskine, A. Quadros, P. Morton, and A. Frenkel, "On the segmentation of 3d lidar point clouds," in *2011 IEEE International Conference on Robotics and Automation*. IEEE, 2011, pp. 2798–2805.

[8] P. Tang, D. Huber, B. Akinci, R. Lipman, and A. Lytle, "Automatic reconstruction of as-built building information models from laser-scanned point clouds: A review of related techniques," *Automation in construction*, vol. 19, no. 7, pp. 829–843, 2010.

[9] L. A. Alexandre, "3d descriptors for object and category recognition: a comparative evaluation," in *Workshop on Color-Depth Camera Fusion in Robotics at the IEEE/RSJ International Conference on Intelligent Robots and Systems (IROS), Vilamoura, Portugal*, vol. 1, no. 3, 2012, p. 7.

[10] J. Meza, A. G. Marrugo, E. Sierra, M. Guerrero, J. Meneses, and L. A. Romero, "A structure-from-motion pipeline for topographic reconstructions using unmanned aerial vehicles and open source software," in *Colombian Conference on Computing*. Springer, 2018, pp. 213–225.

[11] X. Chen, Q. Wu, and S. Wang, "Research on 3d reconstruction based on multiple views," in *2018 13th International Conference on Computer Science Education (ICCSE)*, Aug 2018, pp. 1–5.

[12] R. Mekuria, K. Blom, and P. Cesar, "Design, implementation, and evaluation of a point cloud codec for tele-immersive video," *IEEE Transactions on Circuits and Systems for Video Technology*, vol. 27, no. 4, pp. 828–842, 2016.

[13] E. Alexiou and T. Ebrahimi, "On subjective and objective quality evaluation of point cloud geometry," in *2017 Ninth International Conference on Quality of Multimedia Experience (QoMEX)*. IEEE, 2017, pp. 1–3.

[14] J. Zhang, W. Huang, X. Zhu, and J.-N. Hwang, "A subjective quality evaluation for 3d point cloud models," in *2014 International Conference on Audio, Language and Image Processing*. IEEE, 2014, pp. 827–831.

[15] A. Javaheri, C. Brites, F. Pereira, and J. Ascenso, "Subjective and objective quality evaluation of 3d point cloud denoising algorithms," in *2017 IEEE International Conference on Multimedia & Expo Workshops (ICMEW)*. IEEE, 2017, pp. 1–6.

[16] A. Al-Rawabdeh, H. Fangning, A. Moussa, N. El-Sheimy, and A. Habib, "Using an unmanned aerial vehicle-based digital imaging system to derive a 3d point cloud for landslide scarp recognition." *Remote Sensing*, vol. 8, no. 2, p. 95, 2016.

[17] D. Lapandic, J. Velagic, and H. Balta, "Framework for automated reconstruction of 3d model from multiple 2d aerial images," in *2017 International Symposium ELMAR*, Sep. 2017, pp. 173–176.

[18] S. Emami, D. Baggio, K. Ievgen, and N. Mahmood, *Mastering OpenCV with Practical Computer Vision Projects*, ser. Community experience distilled. Packt Publishing, 2012. [Online]. Available: https://books.google.com.py/books?id=GXewmAEACAAJ

[19] J. Yu and C. Park, "3d structure reconstruction from aerial imagery," in *2016 IEEE International Conference on Consumer Electronics-Asia (ICCE-Asia)*, Oct 2016, pp. 1–2.

[20] H. Cui, S. Shen, W. Gao, and Z. Wang, "Progressive large-scale structure-from-motion with orthogonal msts," in *2018 International Conference on 3D Vision (3DV)*, Sep. 2018, pp. 79–88.

[21] C. F. R. C. A. V. D. Tian, H. Ochimizu, "Geometric distortion metrics for point cloud compression." *2017 IEEE International Conference*

on Image Processing (ICIP), Image Processing (ICIP), 2017 IEEE International Conference on, p. 3460, 2017.

[22] E. Alexiou and T. Ebrahimi, "Point cloud quality assessment metric based on angular similarity," in *2018 IEEE International Conference on Multimedia and Expo (ICME)*, July 2018, pp. 1–6.

[23] G. Meynet, J. Digne, and G. Lavoué, "Pc-msdm: A quality metric for 3d point clouds," in *2019 Eleventh International Conference on Quality of Multimedia Experience (QoMEX)*, June 2019, pp. 1–3.

[24] D. Marelli, S. Bianco, L. Celona, and G. Ciocca, "A blender plug-in for comparing structure from motion pipelines," in *2018 IEEE 8th International Conference on Consumer Electronics - Berlin (ICCE-Berlin)*, Sep. 2018, pp. 1–5.

[25] X. Li, W. Li, H. Jiang, and H. Zhao, "Automatic evaluation of machining allowance of precision castings based on plane features from 3d point cloud," *Computers in Industry*, vol. 64, no. 9, pp. 1129–1137, 2013.

[26] J. Degol, J. Y. Lee, R. Kataria, D. Yuan, T. Bretl, and D. Hoiem, "Feats: Synthetic feature tracks for structure from motion evaluation," in *2018 International Conference on 3D Vision (3DV)*, Sep. 2018, pp. 352–361.

[27] K. Jordan and P. Mordohai, "A quantitative evaluation of surface normal estimation in point clouds," in *2014 IEEE/RSJ International Conference on Intelligent Robots and Systems*. IEEE, 2014, pp. 4220–4226.

[28] A. Koutsoudis, B. Vidmar, G. Ioannakis, F. Arnaoutoglou, G. Pavlidis, and C. Chamzas, "Multi-image 3d reconstruction data evaluation," *Journal of Cultural Heritage*, vol. 15, no. 1, pp. 73–79, 2014.

[29] M. Gomez-Redondo, H. Fretes, J. Rodríguez-Piñeiro, J. Rodas, and R. Gregor, "Automatic scene reconstruction algorithm for planialtimetric applications," in *2018 IEEE International Conference on Automation/XXIII Congress of the Chilean Association of Automatic Control (ICA-ACCA)*. IEEE, 2018, pp. 1–6.

[30] D. Borrmann, J. Elseberg, K. Lingemann, and A. Nüchter, "The 3d hough transform for plane detection in point clouds: A review and a new accumulator design," *3D Research*, vol. 2, no. 2, p. 3, 2011.

[31] U. Niethammer, M. James, S. Rothmund, J. Travelletti, and M. Joswig, "Uav-based remote sensing of the super-sauze landslide: Evaluation and results," *Engineering Geology*, vol. 128, pp. 2–11, 2012.

[32] S. K. Gupta and D. P. Shukla, "Application of drone for landslide mapping, dimension estimation and its 3d reconstruction." *JOURNAL OF THE INDIAN SOCIETY OF REMOTE SENSING*, vol. 46, no. 6, pp. 903 – 914, n.d.

[33] P. S. Singh, M. Sharma, V. Saikhom, D. Chutia, C. Gupta, A. Chouhan, and P. L. N. Raju, "Towards generation of effective 3d surface models from uav imagery using open source tools." *Current Science (00113891)*, vol. 114, no. 2, pp. 314 – 321, 2018.

[34] D. Gonzalez-Aguilera, L. López-Fernández, P. Rodriguez-Gonzalvez, D. Hernandez-Lopez, D. Guerrero, F. Remondino, F. Menna, E. Nocerino, I. Toschi, A. Ballabeni *et al.*, "Graphos–open-source software for photogrammetric applications," *The Photogrammetric Record*, vol. 33, no. 161, pp. 11–29, 2018.

[35] Y. Qu, J. Huang, and X. Zhang, "Rapid 3d reconstruction for image sequence acquired from uav camera." *Sensors (Basel, Switzerland)*, vol. 18, no. 1, 2018.

[36] T. Sølund, A. G. Buch, N. Krüger, and H. Aanæs, "A large-scale 3d object recognition dataset," in *2016 Fourth International Conference on 3D Vision (3DV)*. IEEE, 2016, pp. 73–82.

[37] J. Kim and J. Cho, "Delaunay triangulation-based spatial clustering technique for enhanced adjacent boundary detection and segmentation of lidar 3d point clouds." *Sensors (Basel, Switzerland)*, vol. 19, no. 18, p. 3926, 2019.

A.2 Artículo 2

The 2019 International Workshop on Research, Education and Development on Unmanned Aerial Systems (RED-UAS 2019)
Cranfield University, Cranfield, UK

Cascade First and Second Order Sliding Mode Controller of a QuadRotor UAV based on Exponential Reaching Law and Modified Super-Twisting Algorithm

E. Paiva[1], M. Gomez-Redondo[1], J. Rodas[1], Y. Kali[2], M. Saad[2], R. Gregor[1], H. Fretes[1]

***Abstract*— Unmanned aerial vehicles have become a disruptive technology, which has experienced exponential growth in several applications. The control of these vehicles is a fairly wide area and the cascade PID controller is the most used in practice. However, this latter structure doesn't ensure high performances in the presence of unmodelled dynamics, uncertainties and external abrupt disturbances. To that end, this work proposes a new method that consists of a non-linear cascade configuration of the variable structure control between first order sliding mode based on exponential reaching law and modified super-twisting second order sliding mode algorithm. The developed method is tested on simulation on a quadrotor system, the results obtained demonstrate good performance for trajectory tracking and as well as other non-linear controller options, it is robust against unmodeled dynamics and disturbances.**

I. INTRODUCTION

Unmanned Aerial Vehicles (UAV) are systems present in multiple applications related to agriculture such as control and prevention of plant diseases, weeds identification, insect pests and production estimates [1], photogrammetry since UAVs allow fast, accurate and economical scanning of a surface compared to terrestrial, satellite and manned aerial methods [2], inspections of power lines replacing traditional methods such as helicopters or cars, which are often expensive, slow and potentially dangerous [3], load transporting system for environments where geographical conditions are unfavourable [4], [5], security such as remote traffic monitoring and frontier patrols [6], and others [7]. These applications are developed in different operating environments, with a variety of disturbances such as wind and uncertainties that can cause instability.

Currently, there are multiple control algorithms that allow the tracking and stabilization of UAVs, linear controllers such as PID, pole placement or LQR [8] are powerful methods to control systems, but if operating conditions modify the dynamics of the system, the gains of each controller must be changed for stabilization. non-linear control systems are controllers that use the mathematical model of the system studied, within the classification of the controllers are feedback linearization, backstepping, fuzzy logic controllers and sliding mode.

Sliding Mode (SM) is a famous robust nonlinear techniques and well-known for its effectiveness and powerful properties that attract the community of automation researcher [9]. Indeed, the three good features of SM controller are: robustness against a large class of uncertainties, development's simplicity and finite-time convergence. This method uses discontinuous input signals that switch highly to force the system's states to converge in finite-time to the so-called switching function and then to move throughout this surface towards the equilibrium point. SM controller has been tested in simulation and in real time on different nonlinear systems such as electric drive machines [10], [11], highly coupled robot systems [12], [13] and underactuated nonlinear systems as UAVs [14]. Nevertheless, its real-time application still restricted because of the problem of the chattering phenomenon [15]. This problem is considered as the major disadvantage of SM controller since it can lead to very bad performances and the wear of the system's mechanical parts.

In literature, many researchers tried to solve this problem [16]–[19]. The most attractive proposed solution consists of an augmented SM that is known under the name Second Order Sliding Mode (SOSM) [20]. Unlike the classical SM, the SOSM control signals that fed into the system are continuous [21], [22] since the the switching signals act on the derivative of the control inputs. However, its real-time implementation still limited due to the lack of required informations (measurement of the first time derivative of the selected switching function). This problem has been solved by the proposition of the Super-Twisting Algorithm (STA) [23]–[27].

In this paper, considering a quadrotor UAV that is a non-linear underactuated system because its number of degrees of freedom is greater than the number of independent control inputs. The contribution of this work focuses on the proposed sliding mode controller in cascade [28], with an outer position control loop based on the exponential reaching law (ERL) and an inner Attitude/Altitude control loop based on Modified Super-Twisting Algorithm (Modified STA). This cascade configuration is commonly seen in practice with PIDs for pixhawk-based UAV control. The original contribution is to make the inner control loop faster than the outer control loop while ensuring robustness against

[1]Enrique Paiva, Marcos Gomez-Redondo, Jorge Rodas, Raul Gregor and Hector Fretes are with the Laboratory of Power and Control Systems, Facultad de Ingeniería, Universidad Nacional de Asunción, Luque, Paraguay. (enpaiva93@gmail.com, gomezredondomarcos@gmail.com, jrodas@ing.una.py, rgregor@ing.una.py)

[2]Yassine Kali and Maarouf Saad are with the Department of Electrical Engineering, École de Technologie Supérieure, Montreal, QC H3C 1K3, Canada. (y.kali88@gmail.com, maarouf.saad@etsmtl.ca)

978-1-7281-6600-1/19/$31.00 ©2019 IEEE

uncertainties, unmodelled dynamics and perturbations.

The present paper is divided into six sections as follows. In the following section, the full position and attitude mathematical models of the quadrotor UAV system. In Section IV, the simplify position and attitude mathematical models to use in the controller. In Section V the sliding mode controller. In Section VI, numerical simulations of the UAV studied to show the performance of the proposed controller in the presence of perturbation and unknown dynamics. The conclusion is in the last section.

II. Mathematical Model

The system consists of a UAV quadrotor (Fig. 1). The complete mathematical model of the position and attitude is detailed in (1) and (2), respectively [29].

$$\ddot{P} = \left(\frac{R^T}{\mathrm{m}}\right)\left(F - \mathrm{m}\,\dot{R}\,\dot{P} - \mathrm{m}\left(W\,\dot{\Theta} \times R\,\dot{P}\right)\right) \tag{1}$$

$$F = \begin{bmatrix} 0 \\ 0 \\ \tau_1 \end{bmatrix} + \mathrm{m\,g}\,R \begin{bmatrix} 0 \\ 0 \\ 1 \end{bmatrix}$$

$$\ddot{\Theta} = (J\,W)^{-1}\left(\tau - \left(W\,\dot{\Theta} \times J\,W\,\dot{\Theta}\right) - J\,\dot{W}\,\dot{\Theta}\right) \tag{2}$$

where $P = [X, Y, Z]^T$ represents the vector inertial position of an UAV (North, East and Down), $\Theta = [\phi, \theta, \psi]^T$ represents the vector of Euler angles, g is the gravity constant, m denotes the mass of the vehicule, $J = \mathrm{diag}(J_x, J_y, J_z)$ represents the inertia matrix, τ_1 is the sum of the vertical forces generated by each propeller, $\tau = [\tau_\phi, \tau_\theta, \tau_\psi]^T$ denotes the torque vector with its roll, pitch and yaw components.

On the other hand, $W \in \mathcal{R}^{3\times3}$ denotes the matrix of Euler defined by:

$$W = \begin{bmatrix} 1 & 0 & -s_\theta \\ 0 & c_\phi & c_\theta\, s_\phi \\ 0 & -s_\phi & c_\theta\, c_\phi \end{bmatrix}.$$

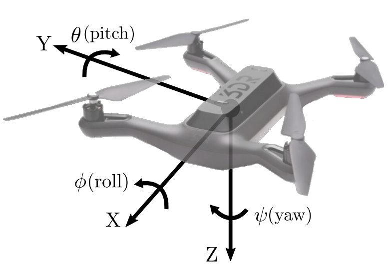

Fig. 1. Quadrotor UAV.

and $R \in \mathcal{R}^{3\times3}$ denotes the matrix transformation to the body frame given by:

$$R^T = \begin{bmatrix} c_\theta c_\psi & s_\phi s_\theta c_\psi - c_\phi s_\psi & c_\phi s_\theta c_\psi + s_\phi s_\psi \\ c_\theta s_\psi & s_\phi s_\theta s_\psi + c_\phi c_\psi & c_\phi s_\theta s_\psi - s_\phi c_\psi \\ -s_\theta & s_\phi c_\theta & c_\phi c_\theta \end{bmatrix}$$

with $c_x = \cos(x)$ and $s_x = \sin(x)$.

The control torque inputs are:

$$\begin{bmatrix} \tau_1 \\ \tau_\phi \\ \tau_\theta \\ \tau_\psi \end{bmatrix} = \underbrace{\begin{bmatrix} -1 & -1 & -1 & -1 \\ l_2 & -l_2 & -l_2 & l_2 \\ l_1 & l_1 & -l_1 & -l_1 \\ -1 & 1 & -1 & 1 \end{bmatrix}}_{\mathrm{T}} \begin{bmatrix} f_1 \\ f_2 \\ f_3 \\ f_4 \end{bmatrix} \tag{3}$$

where f_1, f_2, f_3 and f_4 represent the thrust produced by the four rotors, l_1 and l_2 are the lengths shown in Fig. 2.

In addtion, each force is computed using the inverse of the above matrix equality as:

$$\begin{bmatrix} f_1 \\ f_2 \\ f_3 \\ f_4 \end{bmatrix} = T^{-1} \begin{bmatrix} \tau_1 \\ \tau_\phi \\ \tau_\theta \\ \tau_\psi \end{bmatrix}. \tag{4}$$

III. Mathematical Model for Controller

Since (1) and (2) are complex representations and difficult to implement in-flight controllers, a simplified representation of them was obtained as shown below:

$$\ddot{X} = \frac{\tau_1}{\mathrm{m}}\left(\sin(\phi)\sin(\psi) + \cos(\phi)\sin(\theta)\cos(\psi)\right) \tag{5}$$

$$\ddot{Y} = \frac{\tau_1}{\mathrm{m}}\left(\cos(\phi)\sin(\theta)\sin(\psi) - \sin(\phi)\cos(\psi)\right) \tag{6}$$

$$\ddot{Z} = \frac{\tau_1}{\mathrm{m}}\left(\cos(\phi)\cos(\theta)\right) + \mathrm{g} \tag{7}$$

$$\ddot{\phi} = \frac{\tau_\phi}{J_x} + \frac{\tau_\theta}{J_y}\sin(\phi)\tan(\theta) + \frac{\tau_\psi}{J_z}\cos(\phi)\tan(\theta) \tag{8}$$

$$\ddot{\theta} = \frac{\tau_\theta}{J_y}\cos(\phi) - \frac{\tau_\psi}{J_z}\sin(\phi) \tag{9}$$

$$\ddot{\psi} = \frac{\tau_\theta}{J_y}\sin(\phi)\sec(\theta) + \frac{\tau_\psi}{J_z}\cos(\phi)\sec(\theta). \tag{10}$$

This set of equations are regrouped as follows:

$$\begin{aligned} \dot{\chi}_1 &= \chi_2, \\ \dot{\chi}_2 &= \mathrm{F}(\chi) + \mathrm{G}(\chi)\,u + h. \end{aligned} \tag{11}$$

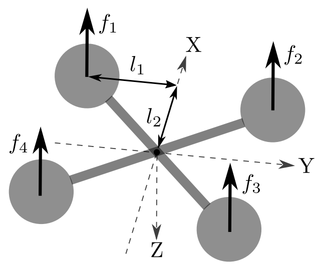

Fig. 2. Force diagram of the Quadrotor UAV.

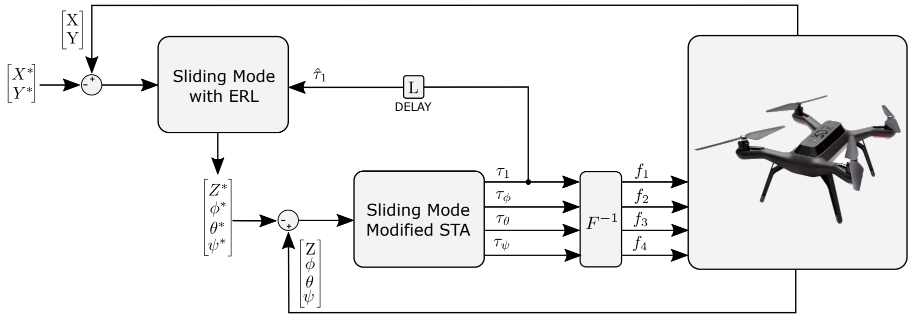

Fig. 3. Block diagram of the closed-loop quadrotor UAV.

where $\chi_1 = [X, Y, Z, \phi, \theta, \psi]^T$ is the state variables vector with and $h \in \mathcal{R}^6$ represents the uncertain vector with unmodeled dynamics and/or perturbations. Based on (5)-(10), the following equivalences are given:

$$\mathrm{F}(\chi) = \begin{bmatrix} 0 & 0 & \mathrm{g} & 0 & 0 & 0 \end{bmatrix}^T$$

$$\mathrm{G}(\chi) = \begin{bmatrix} g_{11} & g_{12} & 0 & 0 & 0 & 0 \\ g_{21} & g_{22} & 0 & 0 & 0 & 0 \\ 0 & 0 & g_{33} & 0 & 0 & 0 \\ 0 & 0 & 0 & g_{44} & g_{45} & g_{46} \\ 0 & 0 & 0 & 0 & g_{55} & g_{56} \\ 0 & 0 & 0 & 0 & g_{65} & g_{66} \end{bmatrix}$$

$$\begin{aligned} g_{11} &= \frac{\hat{\tau}_1 \cos(\psi)}{\mathrm{m}} & g_{12} &= \frac{\hat{\tau}_1 \sin(\psi)}{\mathrm{m}} \\ g_{21} &= \frac{\hat{\tau}_1 \sin(\psi)}{\mathrm{m}} & g_{22} &= -\frac{\hat{\tau}_1 \cos(\psi)}{\mathrm{m}} \\ g_{33} &= \frac{\cos(\phi)\cos(\theta)}{\mathrm{m}} & g_{44} &= \frac{1}{J_x} \\ g_{45} &= \frac{\sin(\phi)\tan(\theta)}{J_y} & g_{46} &= \frac{\cos(\phi)\tan(\theta)}{J_z} \\ g_{55} &= \frac{\cos(\phi)}{J_y} & g_{56} &= -\frac{\sin(\theta)}{J_z} \\ g_{65} &= \frac{\sin(\phi)\sec(\theta)}{J_y} & g_{66} &= \frac{\cos(\phi)\sec(\theta)}{J_z} \\ u &= [u_1, u_2]^T \\ u_1 &= [\cos(\phi)\sin(\theta),\ \sin(\phi)] \\ u_2 &= [\tau_1,\ \tau_\phi,\ \tau_\theta,\ \tau_\psi]\,. \end{aligned}$$

In the control matrix $\mathrm{G}_1(\chi)$, $\hat{\tau}_1$ represents the following delayed vertical force:

$$\hat{\tau}_1(t) = \tau_1(t - L),$$

where L is the time delay which is often selected to be the sampling time.

IV. Sliding Mode Controller

The proposed method consists of a cascade sliding mode based on a Proportional-Derivative sliding surface. The inner control loop uses Modified STA to control of attitude and altitude of UAV, whereas the outer control loop uses SM controller with ERL in the UAV position controller and generates the reference signals for the inner control loop Fig. 3. The developed controller will ensure the convergence of the system's state χ_1 to the desired trajectory vector $\chi_1^* = [X^*, Y^*, Z^*, \phi^*, \theta^*, \psi^*]^T$ with ϕ^* and θ^* are computed as:

$$\begin{bmatrix} \phi^* \\ \theta^* \end{bmatrix} = \sin^{-1}\left(\begin{bmatrix} u_2 \\ u_1/\cos(\sin^{-1}(u_2)) \end{bmatrix} \right).$$

The trajectory tracking error is represented by $e = \chi_1 - \chi_1^*$ and the sliding surface selected in this paper is:

$$S = \dot{e} + K_p\, e \tag{12}$$

where $K_p = \mathrm{diag}(K_{p1}, K_{p2}, \cdots, K_{p6})$ is a diagonal positive definite matrix. Now, let us use (11) to compute the time derivative of the selected linear switching function S as follows:

$$\begin{aligned} \dot{S} &= \ddot{e} + K_p\, \dot{e} \\ &= \dot{\chi}_2 - \ddot{\chi}_1^* + K_p\, \dot{e} \\ &= \mathrm{F}(\chi) + \mathrm{G}(\chi)\, u - \ddot{\chi}_1^* + K_p\, \dot{e}. \end{aligned} \tag{13}$$

The vector of cascade sliding mode controller, combined sliding mode with ERL [30] and Modified STA [28] is:

$$\dot{S} = \begin{bmatrix} -\dfrac{K_{11}}{N(S_1)}\,\mathrm{sign}(S_1) - K_{12}\, S_1 + \dot{\varpi}_1 \\ -\dfrac{K_{21}}{N(S_2)}\,\mathrm{sign}(S_2) - K_{22}\, S_2 + \dot{\varpi}_2 \\ -K_{31}\, |S_3|^{0.5}\,\mathrm{sign}(S_3) - K_{32}\, S_3 + \dot{\varpi}_3 \\ -K_{41}\, |S_4|^{0.5}\,\mathrm{sign}(S_4) - K_{42}\, S_4 + \dot{\varpi}_4 \\ -K_{51}\, |S_5|^{0.5}\,\mathrm{sign}(S_5) - K_{52}\, S_5 + \dot{\varpi}_5 \\ -K_{61}\, |S_6|^{0.5}\,\mathrm{sign}(S_6) - K_{62}\, S_6 + \dot{\varpi}_6 \end{bmatrix} \tag{14}$$

where $N(S_i) = \delta_0 + (1 - \delta_0)\,\mathrm{e}^{-a\,|S_i|^p}$ for $i = 1, 2$ with $0 < \delta_0 < 1$ and $a, p > 0$ [31].

$$\dot{\varpi} = \begin{bmatrix} 0 \\ 0 \\ -K_{33}\,\mathrm{sign}(S_3) - K_{34}\,\varpi_3 \\ -K_{43}\,\mathrm{sign}(S_4) - K_{44}\,\varpi_4 \\ -K_{53}\,\mathrm{sign}(S_5) - K_{54}\,\varpi_5 \\ -K_{63}\,\mathrm{sign}(S_6) - K_{64}\,\varpi_6 \end{bmatrix} \tag{15}$$

with the sign function:

$$\operatorname{sign}(S_i) = \begin{cases} 1, & \text{if } S_i > 0, \\ 0, & \text{if } S_i = 0, \\ -1, & \text{if } S_i < 0. \end{cases} \tag{16}$$

Hence, combining (13) and (14) gives the following control law expression:

$$\begin{aligned} u =& \mathrm{G}^{-1}(\chi)\left(\ddot{\chi}_1^* - K_p\,\dot{e} - \mathrm{F}(\chi)\right) \\ &+ \mathrm{G}^{-1}(\chi) \begin{bmatrix} -\dfrac{K_{11}}{N(S_1)}\operatorname{sign}(S_1) - K_{12}\,S_1 + \dot{\varpi}_1 \\ -\dfrac{K_{21}}{N(S_2)}\operatorname{sign}(S_2) - K_{22}\,S_2 + \dot{\varpi}_2 \\ -K_{31}\,|S_3|^{0.5}\operatorname{sign}(S_3) - K_{32}\,S_3 + \dot{\varpi}_3 \\ -K_{41}\,|S_4|^{0.5}\operatorname{sign}(S_4) - K_{42}\,S_4 + \dot{\varpi}_4 \\ -K_{51}\,|S_5|^{0.5}\operatorname{sign}(S_5) - K_{52}\,S_5 + \dot{\varpi}_5 \\ -K_{61}\,|S_6|^{0.5}\operatorname{sign}(S_6) - K_{62}\,S_6 + \dot{\varpi}_6 \end{bmatrix} \end{aligned} \tag{17}$$

The detailed stability analysis can be found in [28], [32].

V. Simulation Results

In this section, Matlab/Simulink is the software used to simulate the performance of the cascade sliding mode controller. The simplified mathematical model allows simulating conditions of unmodeled dynamics and we added Gaussian noise on each state variable (Fig. 4).

The physical parameters are shown in the Table I.

TABLE I
Quadrotor UAV's parameters.

Parameters	Value
Mass, m	4 Kg
Moment of inertia, J_x	0.111132 Kg.m^2
Moment of inertia, J_y	0.13282 Kg.m^2
Moment of inertia, J_z	0.249039 Kg.m^2
Length, l_1	0.2 m
Length, l_2	0.2 m
Gravity, g	9.81 m.s^{-2}

The gains for sliding surface are K_p=diag$(1, 1, 1, 5, 5, 5)$ and for cascade sliding mode controller are in Table II. All these gains were found heuristically.

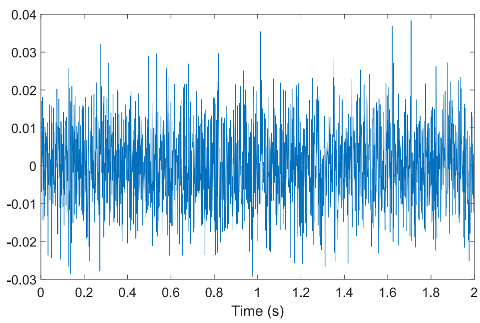

Fig. 4. Disturbances on each position and each Euler Angle of UAV.

The time delay between outer/inner controls loop is $L = 0.006$ s, while the sampling time for outer loop control is 10^{-2} s and for the inner control loop is 0.004 s.

TABLE II
Sliding Mode controller gains.

Gains	Values	Gains	Values	Gains	Values
K_{11}	0.1	K_{41}	1.5	K_{61}	1
K_{12}	0.5	K_{42}	7.5	K_{62}	5
K_{21}	0.1	K_{43}	7.5	K_{63}	5
K_{22}	0.5	K_{44}	7.5	K_{64}	5
K_{31}	2	K_{51}	0.1	δ_0	0.1
K_{32}	2	K_{52}	1	p	3
K_{33}	2	K_{53}	1	a	2
K_{34}	2	K_{54}	1		

The simulation consists of tracking a square path with different values of orientation angles (ψ). The tracking results are in Fig. 5 and Fig. 6, along with the desired paths. The Fig. 7 corresponds to the thrusts for the UAV generated by the controller and the three-dimensional path is shown in Fig. 8.

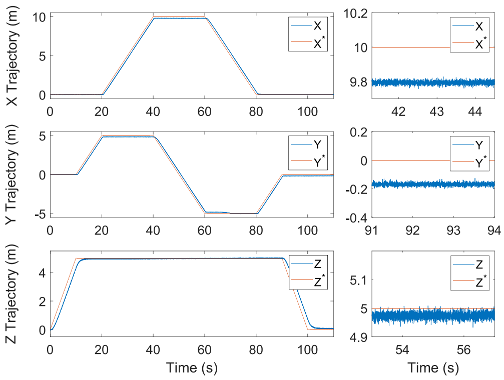

Fig. 5. Simulation results of position tracking.

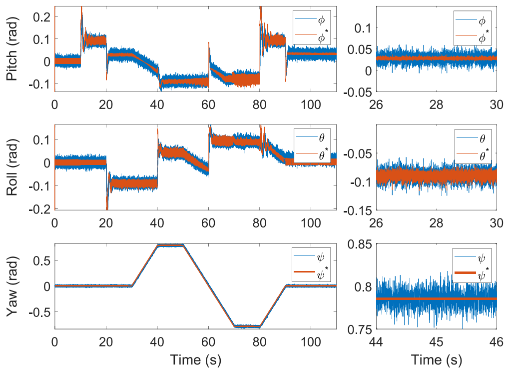

Fig. 6. Simulation results of attitude tracking.

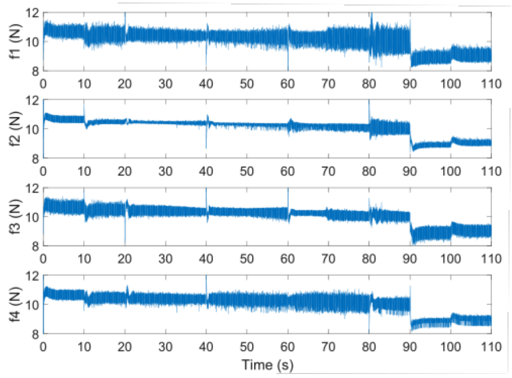

Fig. 7. Simulation results of control inputs.

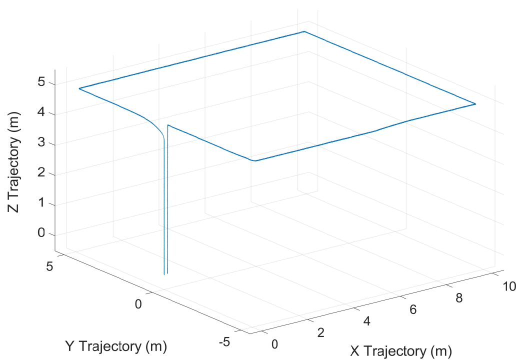

Fig. 8. 3D position tracking.

In summary, it is observed that there are errors in an average of 0.20 m for the transient and steady-state conditions as depicted in Fig. 5. The reasons can be, on one hand, due to the sub-optimal gains obtained heuristically, and, on the other hand, due to the choice of the sliding surface. Also, in Fig. 7, we can see that the chattering effect is in a range of 2 N and its high switching frequency is a known characteristic of the continuous sliding mode controller. Note that the obtained results can be improved by (i) adding an integral part in the sliding surface which also will increase the complexity for the determination of the gains, (ii) with better gain values using optimization algorithms. Nevertheless, by analyzing the tracking trajectory, the obtained results are satisfactory, taking into account the curve of the desired trajectory (Fig. 5 and Fig. 6) and the uncertainties.

VI. Conclusions

In this work, a cascade sliding mode controller was simulated with exponential reaching law in the outer control loop and Modified STA in the inner control loop, under noise conditions and unmodelled dynamics the controller performs well and can be improved by optimizing the controller's gains. This choice belongs to the fact that the inner control loop must be faster than the outer control loop. This condition is satisfied since the modified STA allows faster convergence and higher precision. The proposed combination has been tested on simulations where the results obtained showed good tracking performance even if the used model was highly uncertain.

Acknowledgements

The authors would like to thank to the Paraguayan Government for the financial support through CONACYT research project (PINV15-0136).

References

[1] Z. Yingkun, "Flight path planning of agriculture uav based on improved artificial potential field method," in *2018 Chinese Control And Decision Conference (CCDC)*, June 2018, pp. 1526–1530.

[2] M. Gomez-Redondo, H. Fretes, J. Rodríguez-Piñeiro, J. Rodas, and R. Gregor, "Automatic scene reconstruction algorithm for planialtimetric applications," in *2018 IEEE International Conference on Automation/XXIII Congress of the Chilean Association of Automatic Control (ICA-ACCA)*, Oct 2018, pp. 1–6.

[3] V. N. Nguyen, R. Jenssen, and D. Roverso, "Intelligent monitoring and inspection of power line components powered by uavs and deep learning," *IEEE Power and Energy Technology Systems Journal*, vol. 6, no. 1, pp. 11–21, March 2019.

[4] A. Altan, O. Aslan, and R. Hacıoğlu, "Real-time control based on narx neural network of hexarotor uav with load transporting system for path tracking," in *2018 6th International Conference on Control Engineering Information Technology (CEIT)*, Oct 2018, pp. 1–6.

[5] Z. Liu, X. Liu, J. Chen, and C. Fang, "Altitude control for variable load quadrotor via learning rate based robust sliding mode controller," *IEEE Access*, vol. 7, pp. 9736–9744, 2019.

[6] Z. Xu, H. Shi, N. Li, C. Xiang, and H. Zhou, "Vehicle detection under uav based on optimal dense yolo method," in *2018 5th International Conference on Systems and Informatics (ICSAI)*, Nov 2018, pp. 407–411.

[7] H. Shakhatreh, A. H. Sawalmeh, A. Al-Fuqaha, Z. Dou, E. Almaita, I. Khalil, N. S. Othman, A. Khreishah, and M. Guizani, "Unmanned aerial vehicles (uavs): A survey on civil applications and key research challenges," *IEEE Access*, vol. 7, pp. 48 572–48 634, 2019.

[8] C. Liu, J. Pan, and Y. Chang, "Pid and lqr trajectory tracking control for an unmanned quadrotor helicopter: Experimental studies," in *2016 35th Chinese Control Conference (CCC)*, July 2016, pp. 10 845–10 850.

[9] V. Utkin, J. Guldner, and J. Shi, *Sliding mode control in electromechanical systems*. Taylor-Francis, 1999.

[10] Y. Kali, J. Rodas, M. Ayala, M. Saad, R. Gregor, K. Benjelloun, J. Doval-Gandoy, and G. Goodwin, "Discrete-time sliding mode with time delay estimation of a six-phase induction motor drive," in *IECON 2018 - 44th Annual Conference of the IEEE Industrial Electronics Society*, Oct 2018, pp. 5807–5812.

[11] Y. Kali, M. Ayala, J. Rodas, M. Saad, J. Doval-Gandoy, R. Gregor, and K. Benjelloun, "Current control of a six-phase induction machine drive based on discrete-time sliding mode with time delay estimation," *Energies*, vol. 12, no. 1, 2019.

[12] Y. Feng, X. Yu, and Z. Man, "Non-singular terminal sliding mode control of rigid manipulators," *Automatica*, vol. 38, no. 12, pp. 2159 – 2167, 2002.

[13] Y. Kali, M. Saad, K. Benjelloun, and M. Benbrahim, "Sliding mode with time delay control for mimo nonlinear systems with unknown dynamics," in *2015 International Workshop on Recent Advances in Sliding Modes (RASM)*, April 2015, pp. 1–6.

[14] K. Runcharoon and V. Srichatrapimuk, "Sliding mode control of quadrotor," in *TAEECE, International Conference on Technological Advances in Electrical, Electronics and Computer Engineering*, May 2013, pp. 552–557.

[15] I. Boiko and L. Fridman, "Analysis of chattering in continuous sliding-mode controllers," *IEEE Transactions on Automatic Control*, vol. 50, no. 9, pp. 1442–1446, Sept 2005.

[16] M. Tseng and M. Chen, "Chattering reduction of sliding mode control by low-pass filtering the control signal," *Asian Journal of Control*, vol. 12, no. 3, pp. 392–398, 2010.

[17] D. Lee, H. Jin Kim, and S. Sastry, "Feedback linearization vs. adaptive sliding mode control for a quadrotor helicopter," *International Journal of Control, Automation and Systems*, vol. 7, no. 3, pp. 419–428, Jun 2009.

[18] Y. Kali, J. Rodas, R. Gregor, M. Saad, and K. Benjelloun, "Attitude tracking of a tri-rotor uav based on robust sliding mode with time delay estimation," in *2018 International Conference on Unmanned Aircraft Systems (ICUAS)*, June 2018, pp. 346–351.

[19] L. Besnard, Y. B. Shtessel, and B. Landrum, "Quadrotor vehicle control via sliding mode controller driven by sliding mode disturbance observer," *Journal of the Franklin Institute*, vol. 349, no. 2, pp. 658 – 684, 2012.

[20] A. Levant, "Higher-order sliding modes, differentiation and output-feedback control," *International Journal of Control*, vol. 76, no. 9-10, pp. 924–941, 2003.

[21] Y. Kali, M. Saad, and K. Benjelloun, "Non-singular terminal second order sliding mode with time delay estimation for uncertain robot manipulators," in *ICINCO, International Conference on Informatics in Control, Automation and Robotics*, 2017, pp. 226–232.

[22] Y. Kali, M. Saad, K. Benjelloun, and A. Fatemi, "Discrete-time second order sliding mode with time delay control for uncertain robot manipulators," *Robotics and Autonomous Systems*, vol. 94, pp. 53 – 60, 2017.

[23] A. Benallegue, A. Mokhtari, and L. Fridman, "High-order sliding-mode observer for a quadrotor UAV," *International Journal of Robust and Nonlinear Control*, vol. 18, no. 4-5, pp. 427–440, 2008.

[24] I. González-Hernández, S. Salazar, F. Munoz, and R. Lozano, "Super-twisting control scheme for a miniature quadrotor aircraft: Application to trajectory-tracking problem," in *ICUAS, International Conference on Unmanned Aircraft Systems*, June 2017, pp. 1547–1554.

[25] I. González-Hernández, F. M. Palacios, S. S. Cruz, E. S. E. Quesada, and R. L. Leal, "Real-time altitude control for a quadrotor helicopter using a super-twisting controller based on high-order sliding mode observer," *International Journal of Advanced Robotic Systems*, vol. 14, no. 1, pp. 1–15, 2017.

[26] E. Ibarra and P. Castillo, "Nonlinear super twisting algorithm for UAV attitude stabilization," in *ICUAS, International Conference on Unmanned Aircraft Systems*, June 2017, pp. 640–645.

[27] Y. Kali, M. Saad, K. Benjelloun, and C. Khairallah, "Super-twisting algorithm with time delay estimation for uncertain robot manipulators," *Nonlinear Dynamics*, vol. 93, no. 2, pp. 557–569, Jul 2018.

[28] E. Paiva, J. Rodas, Y. Kali, R. Gregor, and M. Saad, "Robust flight control of a tri-rotor uav based on modified super-twisting algorithm," in *2019 International Conference on Unmanned Aircraft Systems (ICUAS)*, June 2019, pp. 551–556.

[29] R. W. Beard and T. W. McLain, *Small Unmanned Aircraft: Theory and Practice*. Princeton, NJ, USA: Princeton University Press, 2012.

[30] C. J. Fallaha, M. Saad, H. Y. Kanaan, and K. Al-Haddad, "Sliding-mode robot control with exponential reaching law," *IEEE Transactions on Industrial Electronics*, vol. 58, no. 2, pp. 600–610, Feb 2011.

[31] Y. Kali, M. Saad, and K. Benjelloun, *Control of Robot Manipulators Using Modified Backstepping Sliding Mode*. Singapore: Springer Singapore, 2019, pp. 107–136.

[32] Y. Kali, K. Benjelloun, M. Saad, and M. Benbrahim, "Non-singular terminal sliding mode with time delay control for uncertain 2nd order nonlinear systems," in *2017 14th International Multi-Conference on Systems, Signals Devices (SSD)*, March 2017, pp. 625–630.

A.3 Artículo 3

Model Predictive Current Control of Dual-Mode Voltage Source Inverter Operations: Islanded and Grid-Connected

1st Fatima Martinez
Maestría en Ingeniería Electrónica
Universidad Cono Sur de las Américas
Asunción, Paraguay
fmartinez@alumnomie.ucsa.edu.py

2nd Thalia Morel
Maestría en Ingeniería Electrónica
Universidad Cono Sur de las Américas
Asunción, Paraguay
tmorel@alumnomie.ucsa.edu.py

3rd Hector Fretes
Maestría en Ingeniería Electrónica
Universidad Cono Sur de las Américas
Asunción, Paraguay
hfretes@alumnomie.ucsa.edu.py

4th Jorge Rodas
Universidad Nacional de Asunción
Luque, Paraguay
jrodas@ing.una.py

5th Yassine Kali
École de Technologie Superiéure
Montreal, Canada
y.kali88@gmail.com

6th Raul Gregor
Universidad Nacional de Asunción
Luque, Paraguay
rgregor@ing.una.py

***Abstract*—Model predictive control (MPC) has been a research topic for power converters control due to its simplicity, easy inclusion of constraints, fast dynamic response, among others. This work proposes the use of MPC as a current regulator of a voltage source inverter (VSI) in a dual-mode operation. On one hand, the VSI is used to provide current to a load from a photovoltaic panel, being in islanded condition. On the other hand, the VSI is used as an active power filter for the reactive power compensation for a grid-connected condition. Simulation results are provided to show the benefits of the proposed controller.**

***Index Terms*—Active power filter, current control, photovoltaic systems, model predictive control, voltage source inverter.**

NOMENCLATURE

APF	Active power filter.
DG	Distributed generation.
FFT	Fast Fourier transform.
MPC	Model predictive control.
PCC	Predictive current control.
PV	Photovoltaic.
RES	Renewable energy sources.
THD	Total harmonic distortion.
VSI	Voltage source inverter.

I. INTRODUCTION

In the last years, the renewable energy sources (RES) and power quality have captured the attention of the international scientific community. This has been mainly justified, on the one hand, for the need to meet energy demands, and on the other hand, for the need to optimize the available energy resources [1], [2]. In both applications, power electronic converters play an important role due to this devices are capable of modifying the input voltage and current characteristics in order to interconnect RES with the distribution grid under the concept of distributed generation (DG), feed an islanded load or improve the power quality [3]. Besides, several new power converter topologies have been proposed in the literature, such as matrix converters [4], [5] multilevel converters [6], [7] neutral-point clamped converter [8], [9] among others, the two-level voltage source inverter (VSI) is still the most used in industry applications [10], [11]. One of the most commonly used three-phase converter topology is based on three H-bridge cells [12].

The design of suitable controllers for power converters applied to DG is an issue of paramount importance to researchers. For the particular case of control of VSIs, different new techniques have been studied and applied in the past decades, such as the sliding-mode control [13], [14], dead-beat control [15], [16], or the model predictive control (MPC) [17], [18], among others. As a consequence of the fast development of digital signal processors, the finite-set MPC has become a promising control method for power converters due to its advantages, such as a fast-tracking response, a high control bandwidth, and providing a very simple way of including system nonlinearities and constraints [19].

This paper proposes the MPC for a complex control strategy with multiple objectives, using the predictive current control (PCC) for a dual-mode VSI operation. Is based on [12] where a PCC was carried out to compensate reactive power in the load as well as to compensate current in the neutral. In this case, the PCC will be applied to the output of the two-level H-bridge converter, in one case working as an active power filter (APF) while, in the other case, to feed a load through the VSI. In both cases, instantaneous measurements are carried out in order to know the reactive power to be compensated, this compensation is carried out by injecting a reactive current that is 180 degrees out of phase proceeding from the reactive power of the system.

In order to guarantee a more continuous system, the converter relies on photovoltaic (PV) panels as the main source of choice for the energy required which has a DC-link to store the energy, whether to compensate reactive power or to supply energy to the load according to its functionality. This control was chosen for the robustness of the MPC control and its effectiveness in controlling the desired parameters [20]. The prediction of the output current is obtained with the actuation of the circuit interrupters that determines the voltage level. The voltage chosen is the one that provides the least error between the measured and the predicted current in the cost function, to achieve the expected follow-up. A cost function has been identified where each specific sector is evaluated at each sampling time, based on controlled variables such as the actual filter voltage [12]. The large take-up of renewable energy-based power generation and integration with the existing energy system introduces energy quality problems, such as harmonics and reliability issues, so the integration of renewable energy with improved energy quality is the current trend in research [21]. A passive filter of first order RL is used at the output to improve the quality of the current, since it is the case of a balanced load is not necessary to use a higher order passive filter [22].

II. Mathematical model of the system

The mathematical model of the system is divided in VSI and APF operation modes. Fig. 1 shows the circuit diagram of both cases of the dual-mode operation of the system under study. On one hand, Fig. 1(a) shows the mode of operation as APF connected to the grid. On the other hand, in case of grid disconnection, it automatically switches to its operation as Islanded VSI, shown in Fig 1(b), where PV panels are used as a power source.

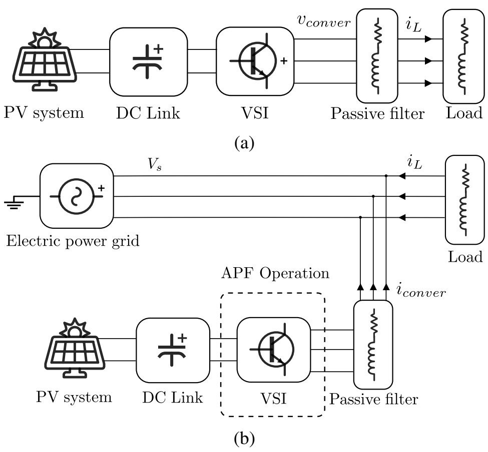

Fig. 1: Scheme of the systems under: (a) Islanded VSI, (b) Grid-Connected APF.

A. VSI operation mode

By means of Kirchhoff's law, for each phase is obtained [23]:

$$v_{R_f} + v_L - v_{conver} + v_{L_f} = 0,$$

$$R_f i_L + v_L - v_{conver} + L_f \frac{d}{dt} i_L = 0, \tag{1}$$

thus,

$$L_f \frac{d}{dt} i_L = v_{conver} - R_f i_L - v_L. \tag{2}$$

The next equation is the discrete form of (2).

$$i_{L[n+1]} = \frac{T_m}{L_f} \left[v_{conver[n]} - v_{L[n]} \right] + i_{L[n]} D \tag{3}$$

being

$$D = \left[1 - \frac{T_m R_f}{L_f} \right],$$

where v_{R_f} is the voltage on the passive filter resistor, v_{Lf} the voltage on the passive filter inductor, v_{conver} the active power filter voltage output, i_L is the converter output current, T_m the sampling time, L_f the passive filter inductance, v_L the load voltage and R_f the passive filter resistance.

B. APF operation mode

By following the same procedure as the previous section, the following equations arise:

$$v_{R_f} + v_S - v_{conver} + v_{L_f} = 0,$$

$$R_f i_{conver} + v_S - v_{conver} + L_f \frac{d}{dt} i_{conver} = 0, \tag{4}$$

thus,

$$L_f \frac{d}{dt} i_{conver} = -v_{conver} - R_f i_{conver} - v_S. \tag{5}$$

By discretizing (5) we have:

$$i_{conver[n+1]} = \frac{T_m}{L_f} \left[v_{conver[n]} - v_{S[n]} \right] + i_{conver[n]} D, \tag{6}$$

where v_s is the voltage source and i_{conver} the converter output current.

All the above-mentioned equations will be used for PCC implementation. Moreover, three bridges are used for each phase of the VSI, as shown in Fig. 2 presenting four possible switching state for each phase of the VSI. Each of them has its respective activation's in the circuit and respective output voltages as shown on the Table I. Note that The H-bridge converter used in each phase offers a greater guarantee of continuity in the event of breakdowns in any of the phases and working independently in the case of load variations, which is why the APF has advantages. Also, compared to a multi-level converter, it requires less maintenance due to the smaller number of switches [24].

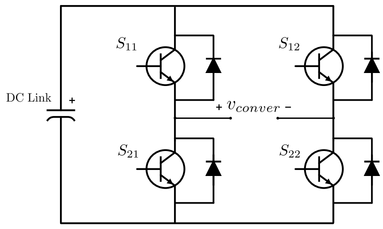

Fig. 2: Two-level H-bridge VSI topology.

TABLE I: Commutation states and outputs for one phase of the converter.

S_{11}	S_{12}	S_{21}	S_{22}
0	0	DC_{link}	DC_{link}
0	DC_{link}	DC_{link}	0
DC_{link}	0	0	DC_{link}
DC_{link}	DC_{link}	0	0

C. PV system description

Although there are different equivalent circuits for the PV cell depending on the simplifications made within [25], the most commonly used is the equivalent circuit shown in Fig. 3. The $I(V)$ characteristic of a PV cell is a non-linear equation with multiple parameters classified by those provided by the manufacturers, those known as constants and those that must be computed. Most of the data sheets provided by manufacturers do not provide sufficient information on parameters that depend on weather conditions, such as irradiance and temperature. Therefore, it is necessary to make some assumptions regarding the physical nature of cell behavior in order to establish a mathematical model of the cell and PV module [25]. The equations needed to obtain the output current I of each PV cell are presented in [26].

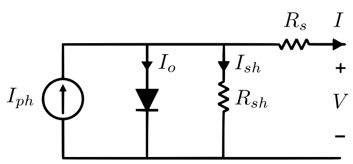

Fig. 3: Equivalent circuit of the PV cell.

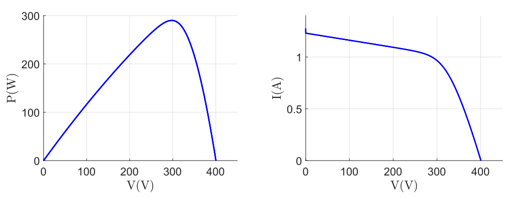

(a) (b)

Fig. 4: Simulation results of PV array characteristics. (a) power-voltage, (b) current-voltage.

TABLE II: Characteristics of TWSE-aSi-100W-1 PV module.

P_{mp}	99.84 W	N_s	159
I_{mp}	0.96 A	n	1.34
V_{mp}	104 V	k_i	0.086 A
I_{sc}	1.22 A	K	1.25e-11
V_{oc}	138 V	q	1.6e-19
R_s	18.33 Ω	E_{go}	1.1
R_{sh}	471.33 Ω	IL	1.26

Moreover, PV module has a unique current-voltage and power-voltage curve characteristic for each irradiation and temperature conditions. In Fig. 4a the $P(V)$ characteristics are shown, the parameters of irradiance and temperature used are under the standard test conditions of 1000 W/m^2 and 25 °C respectively. In the same way, the $I(V)$ characteristics are presented graphically in Fig. 4b.

From the parameters of the PV panel found in Table II , the simulation of the PV module has been conducted, and used as an energy source for the system. The characteristics of the PV panel have been selected due to the need of the system, using three PV panels in series to achieve the purpose.

III. PCC DESIGN

The PCC is one of the MPC, where the load current is the control objective. This process can be divided into three stages. First, identifying all the possible switching states, then initialize the optimal switching value and cost function, predict the load currents, calculate the cost function which minimizes the current error on the inverter, and lastly, apply the optimal switching state. Fig 5 shows the diagram of the predictive current controller applied to one phase of the inverter.

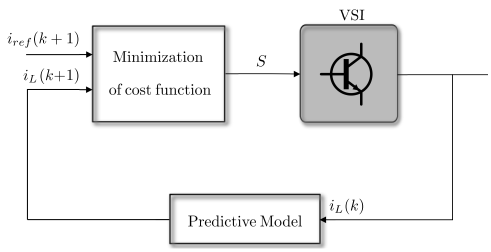

Fig. 5: Diagram of the predictive current controller applied to the two-level VSI.

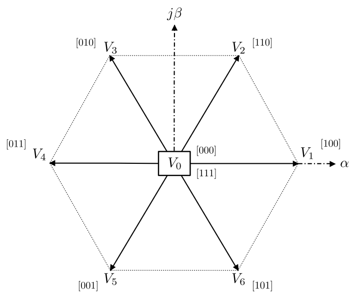

Fig. 6: Space vector diagram for two-level VSI.

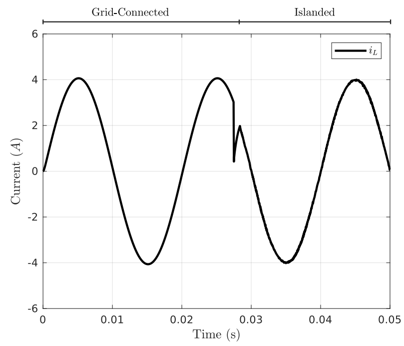

Fig. 7: Load current.

This current estimation is made through (8), by introducing the following modification:

$$i_{L_a[n+1]} = \frac{T_m}{L_f} V_{DC} + \left[1 - \frac{T_m R_f}{L_f}\right] i_{L_m[n]} + \frac{T_m}{L_f} v_{L_m[n]}, \quad (7)$$

$$i_{L_a[n+1]} = \frac{T_m}{L_f} V_{DC} + \left[1 - \frac{T_m R_f}{L_f}\right] i_{L_m[n]} - \frac{T_m}{L_f} v_{S_m[n]}, \quad (8)$$

being i_{L_a} the estimated current for phase A, i_{L_m} the measured current, v_c the voltage corresponding to a given value of the trigger vector and v_{L_m} the voltage measured in the load.

A. *Cost function*

The cost function is used to include the desired behavior of the PCC. In this case, the estimation of the output current is perform 4 times in order to consider all possible trigger voltage vectors. The value of the load current is estimated at each sampling time T_m. All the possible voltage vectors and switching states generated by the VSI are shown in Fig. 6. Then, the trigger vector that provides the lowest value for the cost function is selected and applied during the next sampling time. At each sampling period, the PCC calculates the cost function for each of the possible trigger vectors for each phase of the converter. In this study, the selected cost function is that of the square of the error [6]:

$$f_c = \left(i_{ref} - i_{L_a}\right)^2, \quad (9)$$

where i_{L_a} represents the estimated current of phase A while $i_{L_{ref}}$ is the reference current. For lower cost function values the output current is expected to approximate more closely to the reference current.

IV. Simulation Results

In order to validate the PCC for the dual-mode operation of the VSI, a Matlab/Simulink model of the system has been designed. The electrical parameters of the VSI used for the simulation are the following: DC_{link} = 308.8 V, the frequency of the source f_r = 50 Hz, the filter inductance L_f = 45 mH, the filter resistance R_f = 0.2 Ω, the load inductance L_l = 50 mH, the load resistance R_l = 76.5 Ω, and the parameters of the semiconductor $R_{on_{IGBT}}$ = 1m Ω, $R_{s_{IGBT}}$ = 100K Ω and $C_{s_{IGBT}}$ = 0.5 F. Also, for the PCC, a custom MATLAB function is implemented using the following parameters: T_m = 45ms, to appreciate the continuity of the service in the current after the connection of the VSI the reference used is i_{ref} = 4 $\angle 0$ ° A.

First, the load is grid-connected and the VSI is workings as APF. Fig. 7 shows a simulation window of 45 ms where the VSI provides power to the load. Note that the interruption of the grid supply can occur at any time, and this case is happening at t = 27.5 ms. Therefore, the change of functionality of the VSI, occurs at the moment of power breakdown. Initially, the reference current is obtained from the measurement of the reactive power of the system to be compensated. It can be seen from the same figure that the VSI needs about 1 ms to reach the reference.

The reference currents when working as an APF are obtained by means of the Clark and Park transformations. Fig. 8 shows the tracking and the comparison with the reference current in both modes of operation, with the mode of operation switch also occurring at T_m = 45ms.

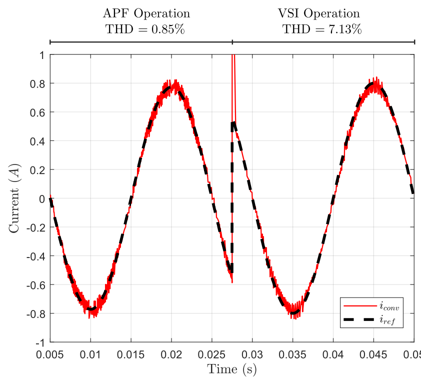

Fig. 8: Current tracking using MPC in the dual-mode converter.

A. APF results

Then, when the VSI operation is as an APF, it keeps the reactive power at zero. In this case, it has been reduced from 360 kVAR to 0 kVAR, from the point of view of the grid. Fig. 9 shows the reactive power when the APF is applied to the system at $t = 0.01$ s. In order to see the time response of the system in case of a sudden change, the APF was exposed to a load change. Therefore, a step in the current tracking can be seen from 0.8 A to 0.97 A. As a consequence, the injected power by the APF has changed from 360 kVAR to 390 kVAR, which can be seen in Fig. 10.

A Fast Fourier Transform (FFT) analysis has been performed in order to evaluate the total harmonic distortion (THD) of the proposed system. Fig. 11 shows an analysis in the converter current when it is operating as an APF. The THD of the injected current is observed from the point of view of the grid supply. The value of current THD observed from the power supply source is 0.85 %. Then, the VSI will be evaluated when it has been used as the power converter, to interconnect the PV to the load.

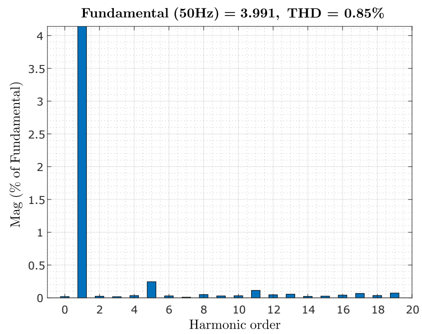

Fig. 11: FFT analysis of the current and THD in the APF.

B. VSI results

The VSI mode of operation is automatically activated in the case of grid disconnection, remaining in Islanded mode with a power source provided by solar panels.

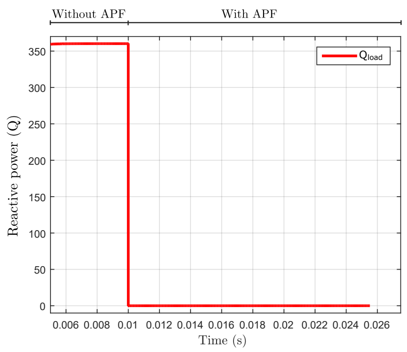

Fig. 9: Reactive power compensation by using the VSI as APF.

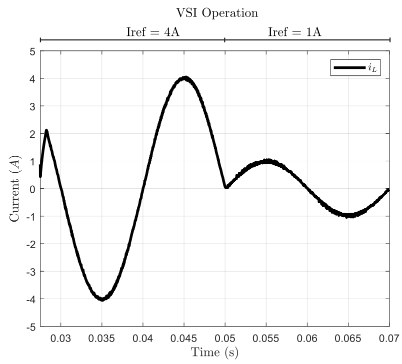

Fig. 12: Load current in VSI mode with change of reference.

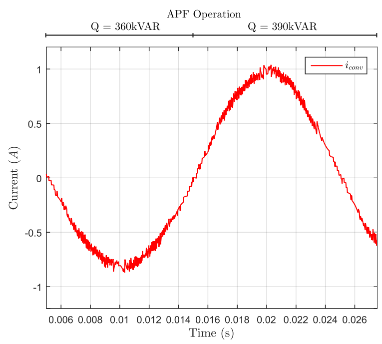

Fig. 10: APF current with change of reactive power.

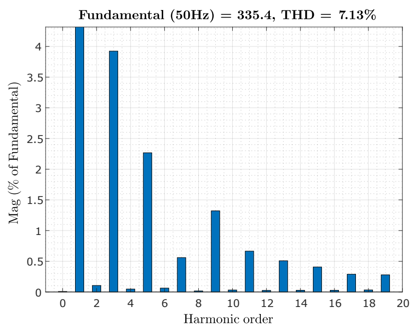

Fig. 13: FFT analysis of the voltage and THD in the VSI.

As in the APF mode of operation, a sudden change of the reference current in the load was made to see the performance of the PCC, from 4 $\angle 0^\circ$ A to 1 $\angle 180^\circ$ A, as can be seen in Fig. 12.

Lastly, in Fig. 13, an FFT analysis was also conducted to show the THD of the system while working in an islanded power source mode, while feeding the load in isolated form the voltage distortion has a value of 7.13 % with a high percentage of odd harmonics.

V. Conclusion

In this paper, predictive current control of a VSI in dual-mode operation has been presented and validated. Simulation results have shown good tracking response of the proposed control. Therefore, the VSI can successfully work as an APF in the presence of the energy supply and, as VSI managing deliver energy to the load from the PV panels. In both cases, the PCC has a good current tracking. When the VSI is used as APF a low THD is also obtained. However, in the other case, a higher THD was obtained. This latter can be reduced by the introduction of a modulation stage in the proposed PCC.

Acknowledgment

The authors wish to thank the financial support from the Paraguayan Science and Technology National Council (CONACYT) through the “Maestría en Ingeniería Electrónica” (POSG17-69) and a special thank you to Prof. Julio Pacher for his help.

References

[1] A. Kumar, B. Sah, A. R. Singh, Y. Deng, X. He, P. Kumar, and R. Bansal, “A review of multi criteria decision making towards sustainable renewable energy development,” *Renewable and Sustainable Energy Reviews*, vol. 69, pp. 596–609, 2017.

[2] M. I. Mosaad and H. Ramadan, “Power quality enhancement of grid-connected fuel cell using evolutionary computing techniques,” *International Journal of Hydrogen Energy*, vol. 43, no. 25, pp. 11 568–11 582, 2018.

[3] B. Ren, X. Sun, S. Chen, and H. Liu, “A compensation control scheme of voltage unbalance using a combined three-phase inverter in an islanded microgrid,” *Energies*, vol. 11, no. 9, p. 2486, 2018.

[4] J. Rodas, R. Gregor, Y. Takase, D. Gregor, and D. Franco, “Multi-modular matrix converter topology applied to the six-phase wind energy generator,” in *2015 50th International Universities Power Engineering Conference (UPEC)*. IEEE, 2015, pp. 1–6.

[5] J. Rodriguez and P. Cortes, *Predictive control of power converters and electrical drives*. John Wiley & Sons, 2012, vol. 40.

[6] R. Gregor, L. Comparatore, A. Renault, J. Rodas, J. Pacher, S. Toledo, and M. Rivera, “A novel predictive-fixed switching frequency technique for a cascade h-bridge multilevel statcom,” in *IECON 2016-42nd Annual Conference of the IEEE Industrial Electronics Society*. IEEE, 2016, pp. 3672–3677.

[7] J. Rodriguez, J.-S. Lai, and F. Z. Peng, “Multilevel inverters: a survey of topologies, controls, and applications,” *IEEE Transactions on Industrial Electronics*, vol. 49, no. 4, pp. 724–738, 2002.

[8] L. Ning, L. Wanting, Z. Hui, W. Shuzheng, and X. Liansong, “A novel modulation strategy of three level npc converter,” in *2018 13th IEEE Conference on Industrial Electronics and Applications (ICIEA)*. IEEE, 2018, pp. 1347–1351.

[9] S. Kamran and J. Muñoz, “Study of a state-of-the art m-statcom,” in *2015 IEEE International Conference on Industrial Technology (ICIT)*. IEEE, 2015, pp. 2733–2738.

[10] F. Gavilan, D. Caballero, S. Toledo, E. Maqueda, R. Gregor, J. Rodas, M. Rivera, and I. Araujo-Vargas, “Predictive power control strategy for a grid-connected 2l-vsi with fixed switching frequency,” in *2016 IEEE International Autumn Meeting on Power, Electronics and Computing (ROPEC)*. IEEE, 2016, pp. 1–6.

[11] M. V. M. Kumar and M. K. Mishra, “Three-leg inverter-based distribution static compensator topology for compensating unbalanced and non-linear loads,” *IET power electronics*, vol. 8, no. 11, pp. 2076–2084, 2015.

[12] A. Renault, M. Rivera, L. Comparatore, J. Pacher, J. Rodas, and R. Gregor, “Model predictive current control with neutral current elimination for h-bridge two-level active power filters,” in *2016 IEEE Ecuador Technical Chapters Meeting (ETCM)*, Oct 2016, pp. 1–5.

[13] M. Huang, Q. Tan, H. Li, and W. Wu, “Improved sliding mode control method of single-phase lcl filtered vsi,” in *2018 9th IEEE International Symposium on Power Electronics for Distributed Generation Systems (PEDG)*. IEEE, 2018, pp. 1–5.

[14] E.-C. Chang, “Study and application of intelligent sliding mode control for voltage source inverters,” *Energies*, vol. 11, no. 10, p. 2544, 2018.

[15] S. Buso, S. Fasolo, L. Malesani, and P. Mattavelli, “A dead-beat adaptive hysteresis current control,” *IEEE Transactions on Industry Applications*, vol. 36, no. 4, pp. 1174–1180, 2000.

[16] A. A. Hossam-Eldin, M. Maghraby, and H. A. Ashour, “Mppt and dead-beat control for power management of hybrid micro-grid applications ahmed. a. hossam-eldin,” *system*, vol. 10, no. 11, p. 12, 2000.

[17] V. Sabatini, A. Lidozzi, L. Solero, A. Formentini, P. Zanchetta, and S. Bifaretti, “Real-time implicit model predictive control for 3-phase vsi,” in *2018 IEEE Energy Conversion Congress and Exposition (ECCE)*. IEEE, 2018, pp. 4015–4020.

[18] Z. Yi, A. J. Babqi, Y. Wang, D. Shi, A. H. Etemadi, Z. Wang, and B. Huang, “Finite-control-set model predictive control (fcs-mpc) for islanded hybrid microgrids,” in *2018 IEEE Power & Energy Society General Meeting (PESGM)*. IEEE, 2018, pp. 1–5.

[19] R. Guzman, L. G. de Vicuña, A. Camacho, J. Miret, and J. M. Rey, “Receding-horizon model-predictive control for a three-phase vsi with an lcl filter,” *IEEE Transactions on Industrial Electronics*, vol. 66, no. 9, pp. 6671–6680, 2018.

[20] H. J. Fard, “Design and implementation of predictive controllers on the rectifier and quasi impedance-source inverter in a wind energy conversion system based on permanent magnet synchronous generator.” *International Journal on Smart Sensing & Intelligent Systems*, vol. 10, no. 2, 2017.

[21] C. N. Mukundan and P. Jayaprakash, “Cascaded h-bridge multilevel inverter based grid integration of solar power with pq improvement,” in *2018 IEEE International Conference on Power Electronics, Drives and Energy Systems (PEDES)*. IEEE, 2018, pp. 1–6.

[22] P. A. Dahono, “A new control method to reduce low-frequency output current ripples of polyphase rectifiers,” in *2007 Power Conversion Conference-Nagoya*. IEEE, 2007, pp. 1099–1104.

[23] Y. Liao, J. You, J. Yang, Z. Wang, and L. Jin, “Disturbance-observer-based model predictive control for battery energy storage system modular multilevel converters,” *Energies*, vol. 11, no. 9, p. 2285, 2018.

[24] L. Comparatore, R. Gregor, J. Rodas, J. Pacher, A. Renault, and M. Rivera, “Model based predictive current control for a three-phase cascade h-bridge multilevel statcom operating at fixed switching frequency,” in *2017 IEEE 8th International Symposium on Power Electronics for Distributed Generation Systems (PEDG)*. IEEE, 2017, pp. 1–6.

[25] H. Bellia, R. Youcef, and M. Fatima, “A detailed modeling of photovoltaic module using matlab,” *NRIAG Journal of Astronomy and Geophysics*, vol. 3, no. 1, pp. 53–61, 2014.

[26] L. Morínigo, T. Morel, J. Rodas, and R. Gregor, “Predictive current control for a neutral point clamped inverter considering sic-mosfet as switches and using a photovoltaic power source,” *AEIT International Annual Conference*, 2019.

A.4 Artículo 4

Pareto Optimal Weighting Factor Design of Predictive Current Controller of a Six-Phase Induction Machine based on Particle Swarm Optimization Algorithm

Hector Fretes, Jorge Rodas, *Senior Member, IEEE,* Jesus Doval-Gandoy, *Member, IEEE,* Victor Gomez, Nicolas Gomez, Mateja Novak, *Member, IEEE,* and Tomislav Dragičević, *Senior Member, IEEE*

***Abstract*—Finite-set model predictive control (FS-MPC) as predictive current control (PCC) is considered an interesting option for the stator current control of multiphase machines due to their control flexibility and easy inclusion of constraints. The weighting factors (WFs) of PCC need to be tuned for the variables of interest such as the machine losses $x-y$ currents, which is typically performed by trial and error procedure. Tuning methods based on neural networks or the coefficient of variation were proposed for three phase inverter and motor drive application. However, the extension of this concept to the multiphase machine application is not straightforward, and only empirical procedure has been reported. In this context, this paper proposes an optimal method to tune the WF of the PCC based on the multi-objective particle swarm optimization (MOPSO) algorithm. A Pareto dominance concept is used for the MOPSO to find the optimal WF values for the PCC comparing parameters of root-mean-square error of the stator tracking currents. Simulation and experimental results are provided to validate the proposed offline tuning procedure of the PCC of a six-phase induction machine, where the improvements of RMSE can be more than 500 % for $x-y$ subspace, with minor effect in $\alpha-\beta$ subspace.**

***Index Terms*—Model predictive control, multiphase induction machine, pareto optimal, particle swarm optimization, stator currents control, weighting factor.**

I. INTRODUCTION

MULTIPHASE machines can be found today in several commercial products such as wind turbines, electric buses, high-speed elevators, ships, among others [1]. The main advantage of this topology compared to the conventional three-phase one is its higher reliability with intrinsic fault-tolerance capability [2]. However, for multiphase machines, it is necessary to control not only the $\alpha-\beta$ stator currents but also those in the secondary $x-y$ subspace which are related to the machine losses [3]. A huge number of stator current controllers has been proposed for multiphase machines, from linear to non-linear techniques [4]. In this latter category, the finite-set model predictive control (FS-MPC) as predictive current control (PCC) has been one of the most popular choices in the last decade [5], [6].

PCC of multiphase machines has been proposed for the first time in [7]. Since then, many improvements for the PCC methods have been proposed for the same system, mostly to solve some issues related to FS-MPC such as high computational burden [8], mathematical model improvement [9], fixed-switching frequency [10], among others. Other contributions more related to multiphase machines were performed for $x-y$ current reduction [11], [12], predictive torque control [13] and post-fault operation [14]. In all the before-mentioned FS-MPC approaches, the cost function (CF) is used to determine the desired behavior of the systems. In multi-objective FS-MPC, the CF includes the weighting factor (WF), the value of which has been usually determined by trial and error procedure for multiphase machine systems providing a trade-off among the variables of interest [15].

The proper tuning of WFs is of paramount importance in order to obtain an optimal control performance. For that reason, it is still an open problem and several approaches have been proposed to tackle this issue. In [16] some guidelines are summarized for CFs without WF, with CFs with secondary terms and with CFs with equally important terms. This guideline is based on the heuristic strategy and it is an extension of [17]. Although the proposed guideline can help us to reduce the number of tuning trials, it still depends on the empirical procedures. Recently, an artificial neural network (ANN) approach is employed to select the WFs automatically [18]. Nonetheless, numerous simulations or experiments are still inevitable to extract the sample data. In [19] a summary of the latest WF tuning techniques for the most used power electronic converters and electric motor drives are presented. However, it does not consider the tuning procedure of multiphase machines. In [20] a WF guideline for a five-phase induction machine (IM) has been proposed. However, the proposal is still a heuristic strategy and the obtained WF values are not the same for all multiphase IMs [15].

In this paper, an optimal tuning procedure is proposed based on multi-objective particle swarm optimization (MOPSO)

Corresponding author: Jorge Rodas.

H. Fretes, J. Rodas V. Gomez, N. Gomez are with the Laboratory of Power and Control Systems, Facultad de Ingeniería, Universidad Nacional de Asunción, Paraguay (e-mail: hectorfretesac@gmail.com, jrodas@ing.una.py, sebasg7@gmail.com, ni_co182@hotmail.com).

J. Doval-Gandoy is with the Applied Power Electronics Technology Research Group, Universidad de Vigo, Spain (e-mail: jdoval@uvigo.es)

M. Novak is with the Department of Energy Technology, Aalborg University, Denmark (e-mail: nov@et.aau.dk).

T. Dragičević is with the Department of Electrical Engineering, Technical University of Denmark, Denmark (e-mail: tomdr@elektro.dtu.dk).

algorithm. This algorithm is able to find optimal WF values, achieving an optimal trade-off among the user-defined figure of merits such as root-mean-squared (RMS) tracking error of $\alpha-\beta$ and $x-y$ stator currents. Moreover, the concept of Pareto optimality is also combined in this paper with the MOPSO algorithm to quickly find sets of optimal calibrations of the WFs parameters. The users can choose the trade-off according to their needs.

The rest of the paper is organized as follows. The mathematical model of the two 2-level voltage source inverter (2L-VSI) and electric drive systems are explained in Section II. PCC technique is also introduced in the same section. In Section III the proposed MOPSO algorithm is explained. An analysis based on simulation and experimental results is presented in Section IV. Finally, conclusions and future trends are summarised in Section V.

II. Preliminaries

A. Six-phase IM and 2L-VSI model

The analyzed system consists of an asymmetrical six-phase IM with two isolated neutral points, fed by 2L-VSI, shown in Fig. 1. After using the vector space decomposition (VSD) approach, the decoupling transformation $\mathbf{T}$ gives $\alpha-\beta$ subspace which is related to flux/torque producing components and loss-producing $x-y$ subspace and a zero-sequence subspace. Then, by using an amplitude invariant criterion, $\mathbf{T}$ is defined as follows:

$$\mathbf{T}=\frac{1}{3}\begin{bmatrix} 1 & \frac{\sqrt{3}}{2} & -\frac{1}{2} & -\frac{\sqrt{3}}{2} & -\frac{1}{2} & 0 \\ 0 & \frac{1}{2} & \frac{\sqrt{3}}{2} & \frac{1}{2} & -\frac{\sqrt{3}}{2} & -1 \\ 1 & -\frac{\sqrt{3}}{2} & -\frac{1}{2} & \frac{\sqrt{3}}{2} & -\frac{1}{2} & 0 \\ 0 & \frac{1}{2} & -\frac{\sqrt{3}}{2} & \frac{1}{2} & \frac{\sqrt{3}}{2} & -1 \\ 1 & 0 & 1 & 0 & 1 & 0 \\ 0 & 1 & 0 & 1 & 0 & 1 \end{bmatrix}. \quad (1)$$

Usually, the discrete model of the system in state-space representation is represented as follows:

$$\mathbf{x}_{k+1}=\mathbf{A}\,\mathbf{x}_k+\mathbf{B}\,\mathbf{u}_k+\mathbf{n}_k \quad (2)$$

$$\mathbf{y}_k=\mathbf{C}\,\mathbf{x}_k+\mathbf{m}_k \quad (3)$$

where stator and rotor current are included in the state vector $\mathbf{x}_k$

$$\mathbf{x}_k=\left[i_{s\alpha(k)},\, i_{s\beta(k)},\, i_{sx(k)},\, i_{sy(k)}, i_{r\alpha(k)},\, i_{r\beta(k)}\right]^T \quad (4)$$

while the stator voltages represent the input vector:

$$\mathbf{u}_k=\left[u_{s\alpha(k)},\, u_{s\beta(k)},\, u_{sx(k)},\, u_{sy(k)}\right]^T \quad (5)$$

and the stator currents are included the output vector:

$$\mathbf{y}_k=\left[i_{s\alpha(k)},\, i_{s\beta(k)},\, i_{sx(k)},\, i_{sy(k)}\right]^T \quad (6)$$

and $\mathbf{n}_k$ is the process noise and $\mathbf{m}_k$ the measurement noise. The stator voltages have a discrete nature (Fig. 2) due to the 2L-VSI model and the relationship between them is represented as:

$$\mathbf{u}_k=V_{\mathrm{dc}}\,\mathbf{T}\,\mathbf{M} \quad (7)$$

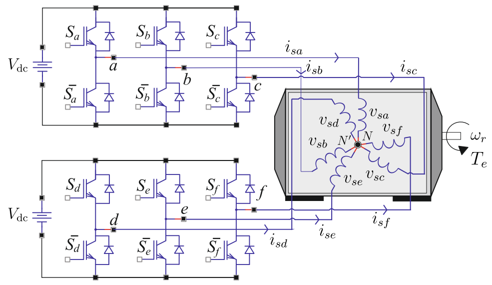

Fig. 1. Schematic diagram of the 2L-VSI.

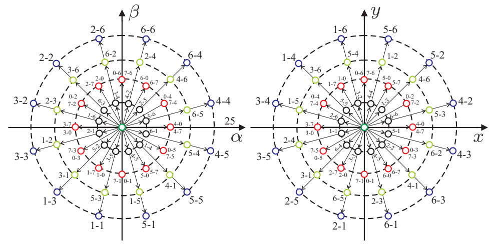

Fig. 2. Projections of the voltage vectors in the $\alpha-\beta$ (left) and $x-y$ (right) subspaces for a six-phase IM. The number that defines each voltage is identified by two octal numbers corresponding to the binary numbers $[S_a\ S_b\ S_c]$ and $[S_d\ S_e\ S_f]$.

where the gating signals are $\mathbf{S}=[S_a,\, S_b,\, S_c,\, S_d,\, S_e,\, S_f]$, being $S_i\in\{0,\,1\}$, V_{dc} is the dc-bus voltage and the 2L-VSI model is:

$$\mathbf{M}=\frac{1}{3}\begin{bmatrix} 2 & 0 & -1 & 0 & -1 & 0 \\ 0 & 2 & 0 & -1 & 0 & -1 \\ -1 & 0 & 2 & 0 & -1 & 0 \\ 0 & -1 & 0 & 2 & 0 & -1 \\ -1 & 0 & -1 & 0 & 2 & 0 \\ 0 & -1 & 0 & -1 & 0 & 2 \end{bmatrix}\mathbf{S}^T. \quad (8)$$

The matrices $\mathbf{A}$, $\mathbf{B}$ are defined as follows:

$$\mathbf{A}=\begin{bmatrix} a_{11} & a_{12} & 0 & 0 & a_{15} & a_{16} \\ a_{21} & a_{22} & 0 & 0 & a_{25} & a_{26} \\ 0 & 0 & a_{33} & 0 & 0 & 0 \\ 0 & 0 & 0 & a_{44} & 0 & 0 \\ a_{51} & a_{52} & 0 & 0 & a_{55} & a_{56} \\ a_{61} & a_{62} & 0 & 0 & a_{65} & a_{66} \end{bmatrix} \quad (9)$$

$$\mathbf{B}=\begin{bmatrix} b_1 & 0 & 0 & 0 \\ 0 & b_1 & 0 & 0 \\ 0 & 0 & b_2 & 0 \\ 0 & 0 & 0 & b_2 \\ b_3 & 0 & 0 & 0 \\ 0 & b_3 & 0 & 0 \end{bmatrix} \quad (10)$$

where:

$$\begin{array}{ll} a_{11} = a_{22} = 1 - T_s\, c_2\, R_s & a_{55} = a_{66} = 1 - T_s\, c_5\, R_r \\ a_{15} = a_{26} = T_s\, c_4\, R_r & a_{33} = a_{44} = 1 - T_s\, c_3\, R_s \\ a_{16} = -a_{25} = T_s\, c_4 L_r\, \omega_{r(k)} & a_{51} = a_{62} = -T_s\, c_4\, R_s \\ a_{52} = -a_{61} = -T_s\, c_5\, L_m\, \omega_{r(k)} & b_1 = T_s\, c_2 \\ a_{56} = -a_{65} = -c_5\, \omega_{r(k)}\, T_s\, L_r & b_2 = T_s\, c_3 \\ a_{12} = -a_{21} = T_s\, c_4 L_m\, \omega_{r(k)} & b_3 = -T_s\, c_4 \end{array}$$

T_s is the sampling time and $c_1 - c_5$ are defined as: $c_1 = L_s L_r - L_m^2$, $c_2 = \frac{L_r}{c_1}$, $c_3 = \frac{1}{L_{ls}}$ $c_4 = \frac{L_m}{c_1}$ $c_5 = \frac{L_s}{c_1}$. The electrical parameters of the system are R_s, R_r, $L_r = L_{lr}+L_m$, $L_s = L_{ls} + L_m$, L_r and L_m. The rotor electrical speed (ω_r) has a relationship with load torque (T_l) and generated torque (T_e) as follows:

$$J_m\, \dot{\omega}_r + B_m\, \omega_r = P\,(T_e - T_l) \tag{11}$$

where B_m and J_m are the friction and the inertia coefficient, respectively, P is the number of pole pairs and T_e is:

$$T_e = 3\, P\, M\, (i_{r\beta}\, i_{s\alpha} - i_{r\alpha}\, i_{s\beta}) \tag{12}$$

where M is the magnetizing inductance.

B. PCC of a Six-Phase IM

FS-MPC uses the model of the system to analyze its future behavior. In this case, the PCC uses the discrete model of the system (2) to predict (at time k) the $k+1$ six-phase IM's stator currents. To consider the delay compensation, $\hat{\mathbf{x}}_{k+2}$ is obtained iteratively using the predictive model. The unmeasured rotor currents are estimated by using the Kalman filter [9], [21].

$$J = |e_{\alpha\beta}|^2 + \lambda_{xy}.|e_{xy}|^2 \tag{13}$$

where:

$$e_{\alpha\beta} = i^*_{s\alpha\beta[k+1]} - i_{s\alpha\beta[k+1]}$$
$$e_{xy} = i^*_{sxy[k+1]} - i_{sxy[k+1]}.$$

III. Proposed WF Design

To find the best values for the WF parameter λ_{xy}, the RMS tracking error of the $\alpha - \beta$ and $x - y$ stator currents are evaluated and used as performance indicators or objectives, making this multiple objective optimization problems. ANN has been used along with weighted sum of objectives as an approach to obtain the WF parameters by [18]. However, the control designer still has limited control over the trade-off among the objectives and this control is not intuitive, due to the ANN method consists of obtaining the different responses of the system for a range of WF values and then obtaining the minimum with another method, i.e. the Matlab min function. Nevertheless, the location of the minimum value depends on the relationship between the objective weights which the user defines manually. Alternatively, by using the Pareto optimally concept, the control designer can choose the best set of λ_{xy} with knowledge of the behavior of this trade-off. Among the various multi-objective algorithms that make use of the Pareto optimality concept, two algorithms that are widely used in different applications are the multi-objective particle swarm optimization (MOPSO) and non-dominated sorting genetic algorithm (NSGA-II). These algorithms have proved to be similar in terms of performance. In [22], both algorithms are used to optimize the sizing of hybrid energy storage systems, concluding that the NSGA-II resulted to be more accurate while the MOPSO was faster. Furthermore, in [23] both algorithms are compared in a water pump system design problem, obtaining better results in term of efficiency of the pump with the MOPSO algorithm. In this work, MOPSO algorithm was chosen mainly because of its simplicity and also because it offers an easy way to control the trade-off between speed of convergence and depth of exploration, as presented in [24].

A. Particle Swarm Optimization (PSO) Algorithm

The PSO algorithm is a stochastic population-based algorithm first proposed in [25], offering a way of trading-off the speed of convergence and the time needed for the exploration. In the PSO algorithm, all of the particles in the swarm move in a search-space defined by the independent variables of the problem which, in this case, corresponds to the WF λ_{xy}. When a particle moves, the algorithm evaluates the parameters taken by the corresponding particle according to a Fitness function $\mathbf{f}(\mathbf{p}_n)$. Usually, the objective of the PSO algorithm is to minimize $\mathbf{f}(\mathbf{p}_n)$. Each particle $\mathbf{p}_n$ in the swarm of N particles has a velocity of $\mathbf{v}_n$, which determines its location in the search-space for the next iteration $j+1$ [24]:

$$\mathbf{p}_{n[j+1]} = \mathbf{p}_{n[j]} + \chi\, \mathbf{v}_{n[j]} + \epsilon_{[j]} \tag{14}$$

where $\chi \in [0,1]$ is a constraint value used to limit the velocity of each particle and ϵ is a vector with random uniformly distributed components in the range $[-1,1]$. This allows the algorithm to increase the range of exploration of the swarm to avoid local minima. The velocity $\mathbf{v}_n$ of the particles is modified so that these move towards the best position found so far by the particle. Personal guide $\mathbf{Pb}_n$ (or Personal best), and the Global guide $\mathbf{Gb}$ (Global best, i.e. the best position found by the whole swarm) achieve an exchange of information among the particles. All of this is accomplished by updating the velocity vector by using the following equation:

$$\mathbf{v}_{n[j+1]} = \hat{w}\,\mathbf{v}_{n[j]} + r_1\,\hat{c}_1\,(\mathbf{P}_n - \mathbf{p}_{n[j]}) + r_2\,\hat{c}_2\,(\mathbf{Gb} - \mathbf{p}_{n[j]}) \tag{15}$$

where r_1 and r_2 are random evenly distributed numbers in the range of [0,1], $\hat{c}_1$ and $\hat{c}_2$ are control factors that establish the influence of global and personal knowledge. Finally, $\hat{w}$ is a factor of inertia, which controls the trade-off between convergence and exploration.

B. Pareto Optimal Principle

Since the PSO is based on a simple concept and is both fast and computationally inexpensive, it has been extended to handle multi-objective optimization problems. The majority of MOPSO algorithms share the same basic approach—a swarm of a certain number of agents is initialized randomly, and that number will remain constant until the end of the run.

In optimization problems with multiple objectives, a set of D objectives have to be optimized. These D objectives (o_i) depend on a vector $\mathbf{p}$ of K decision variables:

$$o_i = \mathbf{f}(\mathbf{p}_n) \qquad \forall i = 1, 2, 3, \cdots, D. \tag{16}$$

According to the Pareto optimal principle [26], a vector p_1 strictly dominates another one p_2 (denoted $p_1 \prec p_2$) if:

$$\mathbf{f}_i(p_1) < \mathbf{f}_i(p_2) \qquad \forall i = 1, 2, 3, \cdots, D, \tag{17}$$

and p_1 weakly dominates p_2 (denoted $p_1 \preceq p_2$) if:

$$\mathbf{f}_i(p_1) \leq \mathbf{f}_i(p_2) \qquad \forall i = 1, 2, 3, \cdots, D. \tag{18}$$

The Pareto front is the set of all non-dominated solutions while the Pareto optimal is a set of vectors that correspond to the Pareto front. In a multi-objective optimization problem, the target is usually to find a well-distributed Pareto front. In this paper, the RMS tracking errors of the $\alpha - \beta$ and $x - y$ stator currents are considered as objectives for the optimization. All values are obtained by using the mathematical model of the electric motor and current controller described in the previous sections. The main difficulty of using the PSO for multiple objective problems is how to choose the best guides. As with other multiple objective algorithms, the concept of Pareto optimal is used, so that the controller designer can choose a convenient solution from the Pareto front. This approach has shown good results in previous works in [26] and [27]. As a consequence, this method has been chosen for this paper due to its simplicity. For the implementation of the MOPSO, a repository $\mathbf{R_p}$ is used to store all of the non-dominated particles up to the current iteration. This repository is updated with every iteration, tending to become the Pareto front of the problem. The updating method is executed as follows: when a particle finds a new non-dominated position, the MOPSO algorithm checks if the particle dominates its previous personal guide or any element from $\mathbf{R_p}$ and removes them if that is the case, adding then the new particle to $\mathbf{R_p}$. If the previous personal best is also non dominated, the new personal best is chosen randomly between the previous one and the new particle. The selection of the global guide for each particle $\mathbf{R_p}$ is based on "PROB" method described in [26] for selecting the best global guides.

IV. Simulation and Experimental Results

To validate the proposed WF tune procedure, the MOPSO is first simulated by using a custom-designed Matlab/Simulink file and the following parameters of a real six-phase IM: $R_s = 6.7\ \Omega$, $R_r = 7\ \Omega$, $L_{ls} = 5.85$ mH, $L_{lr} = 55.7$ mH, $L_m = 708.5$ mH and $J_m = 0.07$ Kg·m^2/s^2. PCC structure and the experimental setup is shown in Fig. 3 and Fig. 4, respectively. The MOPSO parameters are $\hat{c}_1 = 1$, $\hat{c}_2 = 0.9$ and $\hat{w} = 0.6$. Three rotor speed references (ω_r^*) 500 rpm, 1000 rpm and 1500 rpm were considered, while the $d - q$ stator current references are $i_d^* = 1$ A and $i_q^* = 1$ A. Three sampling frequencies (f_s) 8 kHz, 10 kHz and 16 kHz were also considered. For each ω_r^* and f_s, four calibrations were made, with $N = 10$ particles and 25 iterations. However, for the 1500 rpm case, an extra pair of the calibration was made,

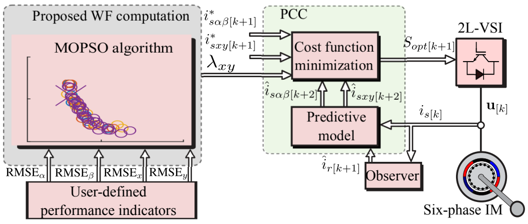

Fig. 3. PCC structure including the proposed WF computation based on MOPSO algorithm.

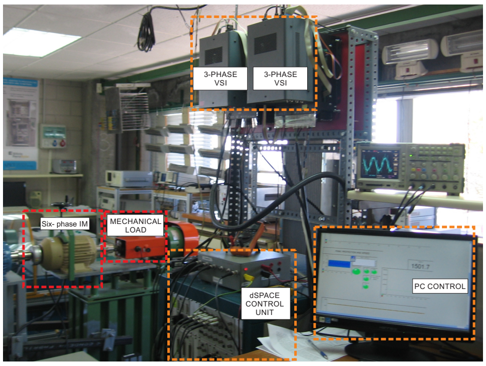

Fig. 4. Block diagram of the test bench including the six-phase IM, the dSPACE platform, the eddy current brake and the six-phase VSI.

with 50 iterations each, in order to verify if a higher number of iterations can give better results. The obtained Pareto fronts for $f_s = 10$ kHz and their respective optimal values can be seen in Fig. 5. Note that the scale of the vertical axis is different (zoomed) from the scale of the horizontal axis. A total of four Pareto Fronts are presented in each figure, one for each calibration, distinguished by colors. The circles correspond to points of the Pareto Fronts, any of these points are optimal values that can be selected according to the designer's criteria. For this paper, the selected points are chosen by minimizing the following expression:

$$\eta = \sqrt{\text{RMSE}_{\alpha\beta}^2 + \text{RMSE}_{xy}^2}. \tag{19}$$

Points that meet these criteria for each calibration are shown in the figures, with their corresponding values of λ_{xy}. The similar point's location for each calibration shows the repetitiveness of the proposed method.

Then, experimental validation were made with a $V_{dc} = 400$ V. For each ω_r^* and f_s, an optimal λ_{xy} provided by the MOPSO algorithm (shaded rows in all tables) is chosen and compared with another λ_{xy} randomly chosen.

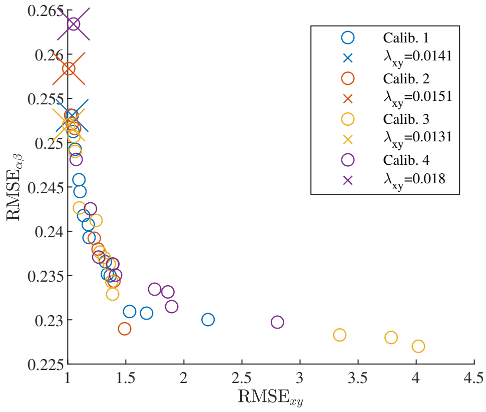

(a)

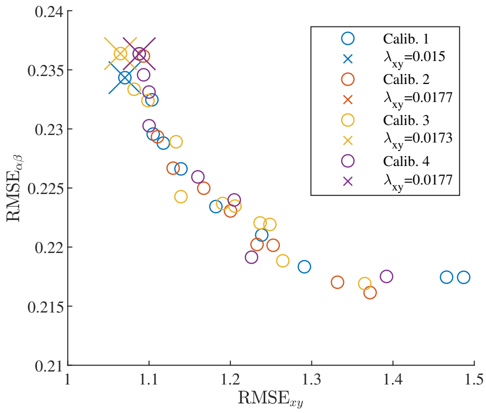

(b)

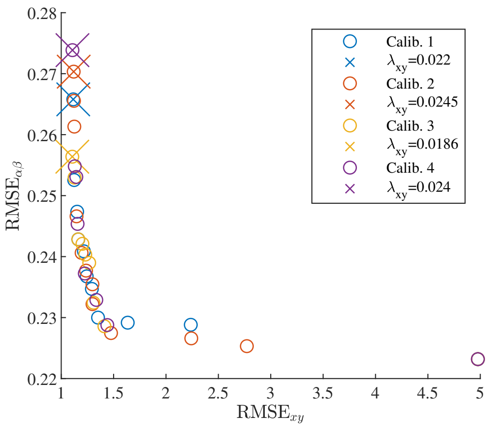

(c)

Fig. 5. Pareto fronts obtained with $f_s = 10$ kHz for (a) $\omega_r^* = 500$ rpm, (b) $\omega_r^* = 1000$ rpm, and (c) $\omega_r^* = 1500$ rpm.

TABLE I
STEADY STATE TEST OF STATOR CURRENTS $\alpha - \beta$, $x - y$, RMSE (A) WITH $f_s = 16$ KHZ AND DIFFERENT ω_r^*.

		$\omega_r^* = 500$ rpm		
λ_{xy}	RMSE$_\alpha$	RMSE$_\beta$	RMSE$_x$	RMSE$_y$
0	0.0685	0.0659	3.6544	3.6467
0.0120	0.0752	0.0740	0.4471	0.4411
0.0190	0.0850	0.0840	0.3713	0.3683
0.1	0.1100	0.1074	0.2647	0.2658
1	0.2220	0.2207	0.1293	0.1302
2	0.2945	0.2909	0.1171	0.1171
		$\omega_r^* = 1000$ rpm		
λ_{xy}	RMSE$_\alpha$	RMSE$_\beta$	RMSE$_x$	RMSE$_y$
0	0.0739	0.077091	3.5964	3.5721
0.0179	0.0961	0.0944	0.4111	0.4108
0.0196	0.0961	0.0949	0.4025	0.3996
0.1	0.1306	0.1272	0.2898	0.2880
1	0.2648	0.2561	0.1463	0.1474
2	0.4147	0.4010	0.1280	0.1286
		$\omega_r^* = 1500$ rpm		
λ_{xy}	RMSE$_\alpha$	RMSE$_\beta$	RMSE$_x$	RMSE$_y$
0	0.0812	0.0804	3.4826	3.5658
0.0161	0.0725	0.0731	0.4253	0.4249
0.0196	0.0773	0.0764	0.4086	0.4113
0.1	0.1291	0.1261	0.3162	0.3154
1	0.3013	0.2952	0.1559	0.1562
2	0.4874	0.4768	0.1394	0.1391

Table I reports the experimental results for $f_s = 16$ kHz, and the mentioned three speeds. It shows that when the maximum priority is put on $\alpha - \beta$ subspace by using $\lambda_{xy} = 0$, the minimum RMSE is obtained for that subspace, and the maximum is obtained for $x - y$ for all rotor speeds. If the WF increases, the RMSE$_{\alpha\beta}$ increases while the RMSE$_{xy}$ improves. The obtained WF for the MOPSO algorithm shows that with a small value of λ_{xy}, the RMSExy improves significantly while RMSE$_{\alpha\beta}$ hardly increases. Further increasing the value of the WF improves the RMSExy with diminishing returns, at the cost of a notable increasing of the RMSE$_{\alpha\beta}$. The same conclusions can be done for Table II and Table III, which report the experimental results for $f_s = 10$ kHz and $f_s = 8$ kHz, respectively.

According also to Table I, the best performance is obtained for $\omega_r^* = 500$ rpm. This is also consistent since the relationship between $f_s = 16$ kHz and the frequency of the fundamental component is higher than in the other cases, so the PCC is more efficient. The same analysis can be done if the results of Tables I, II, and III are compared at the same speed. For a given speed, the results of Table III are worse than those of Table II and these are worse than those of Table I. Note that for the highest WF tested as well as the highest rotor speed, at 10 kHz, PCC becomes unstable (Uns). For 8 kHz the PCC does not work for any WF λ_{xy} values at 1500 rpm.

The reference and measured currents for $\omega_r^* = 1500$ rpm and $f_s = 10$ kHz, with the value obtained by the MOPSO algorithm plotted in Fig. 6 values are shown in Fig. 6 (b) which shows the lowest $\alpha - \beta$ current ripple and the lowest $x - y$ currents compared to the others obtained randomly. Similar

TABLE II
STEADY STATE TEST OF STATOR CURRENTS $\alpha-\beta$, $x-y$, RMSE (A) WITH $f_s = 10$ KHZ AND DIFFERENT ω_r^*.

		$\omega_r^* = 500$	rpm	
λ_{xy}	RMSE$_\alpha$	RMSE$_\beta$	RMSE$_x$	RMSE$_y$
0	0.1049	0.0936	3.9747	3.9391
0.0131	0.1135	0.1126	0.6171	0.6138
0.0180	0.1230	0.1218	0.5294	0.5305
0.1	0.1594	0.1587	0.3826	0.3759
1	0.3114	0.3068	0.1882	0.1884
1.2	0.3335	0.3297	0.1835	0.1826
		$\omega_r^* = 1000$	rpm	
λ_{xy}	RMSE$_\alpha$	RMSE$_\beta$	RMSE$_x$	RMSE$_y$
0	0.1056	0.1088	4.0768	4.0130
0.0150	0.1215	0.1208	0.6409	0.6432
0.0177	0.1265	0.1260	0.6000	0.6002
0.1	0.1929	0.1919	0.4199	0.4187
1	0.3678	0.3698	0.2017	0.2005
1.2	0.4080	0.4085	0.1946	0.1955
		$\omega_r^* = 1500$	rpm	
λ_{xy}	RMSE$_\alpha$	RMSE$_\beta$	RMSE$_x$	RMSE$_y$
0	0.1462	0.1519	4.0806	4.0239
0.0186	0.1110	0.1125	0.6344	0.6366
0.0245	0.1173	0.1178	0.6019	0.6067
0.1	0.1980	0.1976	0.4792	0.4777
1	0.4484	0.4540	0.2187	0.2170
1.2	Uns	–	–	–

TABLE III
STEADY STATE TEST OF STATOR CURRENTS $\alpha-\beta$, $x-y$, RMSE (A) WITH $f_s = 8$ KHZ AND DIFFERENT ω_r^*.

		$\omega_r^* = 500$	rpm	
λ_{xy}	RMSE$_\alpha$	RMSE$_\beta$	RMSE$_x$	RMSE$_y$
0	0.1275	0.1236	4.2003	4.154
0.0172	0.1512	0.1505	0.6212	0.6231
0.0231	0.1576	0.1569	0.5881	0.5877
0.1	0.1936	0.1938	0.4507	0.4512
1	0.3703	0.3741	0.2357	0.2340
		$\omega_r^* = 1000$	rpm	
λ_{xy}	RMSE$_\alpha$	RMSE$_\beta$	RMSE$_x$	RMSE$_y$
0	0.1458	0.1498	4.4836	4.4340
0.0186	0.1608	0.1609	0.7230	0.7299
0.0241	0.1701	0.1680	0.6773	0.6721
0.1	0.2282	0.2286	0.4921	0.4879
0	0.4330	0.4392	0.2514	0.2474

figures were obtained for others sampling frequencies and they were not included for the sake of conciseness.

As the WF λ_{xy} increases, the control effort on the $x-y$ subspace variables increases while the control effort on the $\alpha-\beta$ subspace variables decreases. This entails, as shown in Tables I, II, and III that the RMSE decreases for variables in the $x-y$ subspace while it increases for variables related to the $\alpha-\beta$ subspace. This greater control effort in the $x-y$ subspace also has an effect on the reference tracking error. In this sense, if the tracking error of the variables in the $\alpha-\beta$ subspace, variables related to torque and flux, worsens, the six-phase IM torque will be affected. If the current component

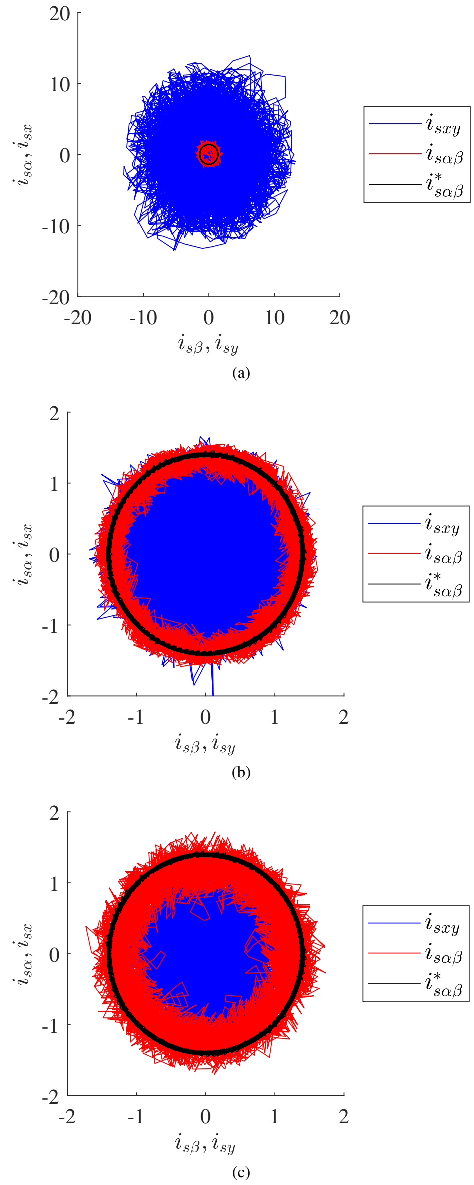

Fig. 6. Stator currents obtained with $f_s = 10$ kHz, $\omega_r^* = 1500$ rpm, for (a) $\lambda_{xy} = 0$, (b) $\lambda_{xy} = 0.0245$, and (c) $\lambda_{xy} = 0.1$.

related to torque, namely i_q, is not capable of reaching the setpoint, the six-phase IM's ability to reach the torque value set by the reference will be reduced. On the other hand, if the current component related to the flux, namely i_d, is not able to reach the setpoint, the field will be weakened and therefore the six-phase IM's torque.

TABLE IV
INFLUENCE OF THE WF λ_{xy} ON THE TORQUE CHARACTERISTICS OF THE SIX-PHASE IM UNDER $f_s = 16$ KHZ, $i_q^* = i_{q(\text{rated})}$, AND $i_d^* = i_{d(\text{rated})}$.

$\omega_r^* = 500$ rpm				
λ_{xy}	$i_{q(\text{actual})}/i_q^*$ (pu)	$i_{d(\text{actual})}/i_d^*$ (pu)	$T_L/T_{L(\text{rated})}$ (%)	$f_{\text{sw(avg)}}$ (kHz)
0.0196	0.97	1	98.33%	5.30
0.1	0.93	0.98	96.88%	5.30
1	0.86	0.96	83.1%	6.20
2	0.76	0.9	77.29%	6.30
$\omega_r^* = 1000$ rpm				
λ_{xy}	$i_{q(\text{actual})}/i_q^*$ (pu)	$i_{d(\text{actual})}/i_d^*$ (pu)	$T_L/T_{L(\text{rated})}$ (%)	$f_{\text{sw(avg)}}$ (kHz)
0.0196	0.96	0.99	95.42%	4.70
0.1	0.89	0.98	91.04%	4.70
1	0.81	0.94	80.83%	5.20
2	0.63	0.87	63.33%	5.45
$\omega_r^* = 1500$ rpm				
λ_{xy}	$i_{q(\text{actual})}/i_q^*$ (pu)	$i_{d(\text{actual})}/i_d^*$ (pu)	$T_L/T_{L(\text{rated})}$ (%)	$f_{\text{sw(avg)}}$ (kHz)
0.0190	0.96	0.99	94.17%	4.3
0.1	0.92	0.98	91.04%	4.30
1	0.78	0.93	75.00%	4.30
2	0.53	0.82	52.08%	4.80

TABLE V
INFLUENCE OF THE WF λ_{xy} ON THE TORQUE CHARACTERISTICS OF THE SIX-PHASE IM UNDER $f_s = 10$ KHZ, $i_q^* = i_{q(\text{rated})}$, AND $i_d^* = i_{d(\text{rated})}$.

$\omega_r^* = 500$ rpm				
λ_{xy}	$i_{q(\text{actual})}/i_q^*$ (pu)	$i_{d(\text{actual})}/i_d^*$ (pu)	$T_L/T_{L(\text{rated})}$ (%)	$f_{\text{sw(avg)}}$ (kHz)
0.0186	0.96	0.99	95.42%	3.50
0.1	0.89	0.98	90.83%	3.50
1	0.72	0.96	78.33%	4.10
2	0.70	0.94	75.63%	4.10
$\omega_r^* = 1000$ rpm				
λ_{xy}	$i_{q(\text{actual})}/i_q^*$ (pu)	$i_{d(\text{actual})}/i_d^*$ (pu)	$T_L/T_{L(\text{rated})}$ (%)	$f_{\text{sw(avg)}}$ (kHz)
0.0177	0.95	0.99	94.17%	3.10
0.1	0.86	0.98	85.21%	3.10
1	0.70	0.94	73.33%	3.50
2	0.62	0.93	61.46%	3.50
$\omega_r^* = 1500$ rpm				
λ_{xy}	$i_{q(\text{actual})}/i_q^*$ (pu)	$i_{d(\text{actual})}/i_d^*$ (pu)	$T_L/T_{L(\text{rated})}$ (%)	$f_{\text{sw(avg)}}$ (kHz)
0.0180	0.95	0.99	93.13%	2.80
0.1	0.84	0.98	83.33%	2.80
1	0.65	0.91	63.96%	3.00
2	0.51	0.87	51.04%	3.10

To demonstrate this behaviour, the six-phase IM was tested in constant torque control mode under the same three ω_r^* 500 rpm, 1000 rpm and 1500 rpm with different WFs λ_{xy}. All tests were carried out under conditions of constant reference torque equal to the nominal torque, i.e. the current references in $d-q$ axes were set to their nominal values. The results are presented in Table IV (for $f_s = 16$ kHz) and Table V (for $f_s = 10$ kHz).

By analyzing Table IV, it can be concluded what follows:

1) As the WF λ_{xy} increases, for a ω_r^*, the tracking errors of i_d^* and i_q^* are larger. The $i_{d(\text{actual})}/i_d^*$ and $i_{q(\text{actual})}/i_q^*$ ratios are reduced, and therefore the achievable torque is smaller (smaller $T_L/T_{L(\text{rated})}$ ratio).
2) On the other hand, if the WF λ_{xy} is kept constant as the ω_r^* is increased, the achievable torque is lower (lower $T_L/T_{L(\text{rated})}$ ratio). This issue was already explained previously and it is related to the fact that by increasing the ω_r^* the relationship between the f_s and the fundamental frequency is reduced and therefore the performance of the current control is reduced.
3) The average switching frequency $f_{\text{sw(avg)}}$ has a dependence inversely proportional to the modulation index (ac/dc voltage ratio). As the ω_r^* increases, the ac voltage increases and, consequently, the switching frequency f_{sw} decreases.
4) The f_{sw} increases with increasing the WF λ_{xy}. This helps to reduce current ripple in both subspaces.

Table V shows the torque characteristics analysis for $f_s = 10$ kHz. The same conclusions indicated above can be drawn from the analysis of the results included in Table V. On the other hand, if the results of Table IV and those of Table V are compared, it can be seen that the reference tracking is worse for lower values of f_s and consequently the achievable torque for the same reference is lower.

V. CONCLUSION

In this paper, an offline optimization method for tuning the WF of a classic PCC for a six-phase IM application is presented. In this application λ_{xy}, which is related to $x-y$ IM currents, is typically the only WF that requires tuning. The proposed is based on the MOPSO algorithm, and uses Pareto optimally for its fitness function so that the user can choose a desirable solution from the Pareto front, thereby ensuring that the solutions are aligned with the purposes of the user. The obtained gain values have been analyzed experimentally in the PCC structure that is commonly used as an alternative to proportional-integral current control in the field-oriented-control approach. The results obtained by using the values provided by the MOPSO algorithm show better optimization of the RMS of $\alpha-\beta$ and $x-y$ IM's stator currents, compared to the results obtained by trial and error method. Moreover, through a proper tuning of the WF the user can maximize the achievable torque and the same time minimize the reference tracking and the RMSE.

The inclusion of more performance parameters in the MOPSO algorithm, i.e. the reduction of the total harmonic distortion or the number of the switching commutation should be investigated in future research. The comparison of the proposed MOPSO method and the ANN method and/or NSGA-II is also an interesting topic to address.

REFERENCES

[1] M. J. Duran, E. Levi, and F. Barrero, "Multiphase electric drives: Introduction," *Wiley encyclopedia of electrical and electronics engineering*, pp. 1–26, 2017.

[2] E. Levi, “Advances in converter control and innovative exploitation of additional degrees of freedom for multiphase machines,” *IEEE Transactions on Industrial Electronics*, vol. 63, no. 1, pp. 433–448, 2015.
[3] M. Jones, S. N. Vukosavic, D. Dujic, and E. Levi, “A synchronous current control scheme for multiphase induction motor drives,” *IEEE Transactions on Energy Conversion*, vol. 24, no. 4, pp. 860–868, 2009.
[4] F. Barrero and M. J. Duran, “Recent advances in the design, modeling, and control of multiphase machines—Part I,” *IEEE Transactions on Industrial Electronics*, vol. 63, no. 1, pp. 449–458, 2016.
[5] P. Gonçalves, S. Cruz, and A. Mendes, “Finite control set model predictive control of six-phase asymmetrical machines—an overview,” *Energies*, vol. 12, no. 24, p. 4693, 2019.
[6] M. Bermúdez, C. Martín, I. González-Prieto, M. J. Durán, M. R. Arahal, and F. Barrero, “Predictive current control in electrical drives: an illustrated review with case examples using a five-phase induction motor drive with distributed windings,” *IET Electric Power Applications*, vol. 14, no. 8, pp. 1291–1310, 2020.
[7] M. Arahal, F. Barrero, S. Toral, M. Duran, and R. Gregor, “Multi-phase current control using finite-state model-predictive control,” *Control Engineering Practice*, vol. 17, no. 5, pp. 579–587, 2009.
[8] M. J. Duran, J. Prieto, F. Barrero, and S. Toral, “Predictive current control of dual three-phase drives using restrained search techniques,” *IEEE Transactions on Industrial Electronics*, vol. 58, no. 8, pp. 3253–3263, 2010.
[9] J. Rodas, F. Barrero, M. R. Arahal, C. Martín, and R. Gregor, “Online estimation of rotor variables in predictive current controllers: A case study using five-phase induction machines,” *IEEE Transactions on Industrial Electronics*, vol. 63, no. 9, pp. 5348–5356, 2016.
[10] O. Gonzalez, M. Ayala, J. Doval-Gandoy, J. Rodas, R. Gregor, and M. Rivera, “Predictive-fixed switching current control strategy applied to six-phase induction machine,” *Energies*, vol. 12, no. 12, p. 2294, 2019.
[11] I. Gonzalez-Prieto, M. J. Duran, J. J. Aciego, C. Martin, and F. Barrero, “Model predictive control of six-phase induction motor drives using virtual voltage vectors,” *IEEE Transactions on Industrial Electronics*, vol. 65, no. 1, pp. 27–37, 2017.
[12] M. Ayala, J. Doval-Gandoy, J. Rodas, O. Gonzalez, R. Gregor, and M. Rivera, “A novel modulated model predictive control applied to six-phase induction motor drives,” *IEEE Transactions on Industrial Electronics*, 2020.
[13] J. A. Riveros, F. Barrero, E. Levi, M. J. Durán, S. Toral, and M. Jones, “Variable-speed five-phase induction motor drive based on predictive torque control,” *IEEE Transactions on Industrial Electronics*, vol. 60, no. 8, pp. 2957–2968, 2012.
[14] Y. Luo and C. Liu, “Pre- and post-fault tolerant operation of a six-phase PMSM motor using FCS-MPC without controller reconfiguration,” *IEEE Transactions on Vehicular Technology*, vol. 68, no. 1, pp. 254–263, 2019.
[15] M. R. Arahal, F. Barrero, M. J. Duran, M. G. Ortega, and C. Martín, “Trade-offs analysis in predictive current control of multi-phase induction machines,” *Control Engineering Practice*, vol. 81, pp. 105–113, 2018.
[16] J. Rodriguez and P. Cortes, *Predictive control of power converters and electrical drives*. John Wiley & Sons, 2012, vol. 40.
[17] P. Cortés, S. Kouro, B. La Rocca, R. Vargas, J. Rodríguez, J. I. León, S. Vazquez, and L. G. Franquelo, “Guidelines for weighting factors design in model predictive control of power converters and drives,” in *2009 IEEE International Conference on Industrial Technology*, 2009, pp. 1–7.
[18] T. Dragičević and M. Novak, “Weighting factor design in model predictive control of power electronic converters: An artificial neural network approach,” *IEEE Transactions on Industrial Electronics*, vol. 66, no. 11, pp. 8870–8880, 2018.
[19] P. Karamanakos and T. Geyer, “Guidelines for the design of finite control set model predictive controllers,” *IEEE Transactions on Power Electronics*, vol. 35, no. 7, pp. 7434–7450, 2019.
[20] C. S. Lim, E. Levi, M. Jones, N. A. Rahim, and W. P. Hew, “FCS-MPC-based current control of a five-phase induction motor and its comparison with PI-PWM control,” *IEEE Transactions on Industrial Electronics*, vol. 61, no. 1, pp. 149–163, 2013.
[21] J. Rodas, C. Martín, M. R. Arahal, F. Barrero, and R. Gregor, “Influence of covariance-based ALS methods in the performance of predictive controllers with rotor current estimation,” *IEEE Transactions on Industrial Electronics*, vol. 64, no. 4, pp. 2602–2607, 2017.
[22] M. I. Hlal, V. K. Ramachandaramurthya, S. Padmanaban, H. R. Kaboli, A. Pouryekta, T. Abdullah, and T. Ab Rashid, “NSGA-II and MOPSO based optimization for sizing of hybrid pv/wind/battery energy storage system,” *International Journal of Power Electronics and Drive Systems*, vol. 1, no. 1, pp. 463–478, 2019.
[23] A. Nourbakhsh, H. Safikhani, and S. Derakhshan, “The comparison of multi-objective particle swarm optimization and nsga ii algorithm: applications in centrifugal pumps,” *Engineering Optimization*, vol. 43, no. 10, pp. 1095–1113, 2011.
[24] V. Gomez, N. Gomez, J. Rodas, E. Paiva, M. Saad, and R. Gregor, “Pareto optimal PID tuning for Px4-based unmanned aerial vehicles by using a multi-objective particle swarm optimization algorithm,” *Aerospace*, vol. 7, no. 6, p. 71, 2020.
[25] J. Kennedy and R. Eberhart, “Particle swarm optimization,” in *IEEE Proceedings of ICNN’95-International Conference on Neural Networks*, vol. 4, 1995, pp. 1942–1948.
[26] J. E. Alvarez-Benitez, R. M. Everson, and J. E. Fieldsend, “A MOPSO algorithm based exclusively on pareto dominance concepts,” in *International Conference on Evolutionary Multi-Criterion Optimization*. Springer, 2005, pp. 459–473.
[27] C. C. Coello and M. S. Lechuga, “Mopso: A proposal for multiple objective particle swarm optimization,” in *IEEE Proceedings of the 2002 Congress on Evolutionary Computation*, vol. 2, 2002, pp. 1051–1056.